12-2013

Measurement of the Prompt Double J/psi Production Cross Section in pp Collisions at sqrt(s) = 7 TeV

Andrew David York
University of Tennessee - Knoxville, ayork7@utk.edu

Recommended Citation

York, Andrew David, "Measurement of the Prompt Double J/psi Production Cross Section in pp Collisions at sqrt(s) = 7 TeV. " PhD diss., University of Tennessee, 2013.
https://trace.tennessee.edu/utk_graddiss/2635

To the Graduate Council:

I am submitting herewith a dissertation written by Andrew David York entitled "Measurement of the Prompt Double J/psi Production Cross Section in pp Collisions at sqrt(s) = 7 TeV." I have examined the final electronic copy of this dissertation for form and content and recommend that it be accepted in partial fulfillment of the requirements for the degree of Doctor of Philosophy, with a major in Physics.

Stefan M. Spanier, Major Professor

We have read this dissertation and recommend its acceptance:

Marianne Breinig, George Siopsis, Grovdena Todorova

Accepted for the Council:

Carolyn R. Hodges

Vice Provost and Dean of the Graduate School

(Original signatures are on file with official student records.)

12-2013

Measurement of the Prompt Double J/psi Production Cross Section in pp Collisions at sqrt(s) = 7 TeV

Andrew David York
University of Tennessee - Knoxville, ayork7@utk.edu

To the Graduate Council:

I am submitting herewith a dissertation written by Andrew David York entitled "Measurement of the Prompt Double J/psi Production Cross Section in pp Collisions at sqrt(s) = 7 TeV." I have examined the final electronic copy of this dissertation for form and content and recommend that it be accepted in partial fulfillment of the requirements for the degree of Doctor of Philosophy, with a major in Physics.

Stefan M. Spanier, Major Professor

We have read this dissertation and recommend its acceptance:

Marianne Breinig, George Siopsis, Grovdena Todorova

Accepted for the Council:
Carolyn R. Hodges

Vice Provost and Dean of the Graduate School

(Original signatures are on file with official student records.)

Measurement of the Prompt Double J/psi Production Cross Section in pp Collisions at sqrt(s) = 7 TeV

A Dissertation Presented for the
Doctor of Philosophy
Degree
The University of Tennessee, Knoxville

Andrew David York
December 2013

Dedicated to my parents and godmother, who have supported me in everything I do.

Acknowledgements

There are many people without whom this work would not be possible. First, I would like to thank my advisor Stefan Spanier, who allowed me to do this PhD research. I am grateful to him for being a constant source of guidance, experience, and motivation, as well as for affording me the opportunity to meet in person with other members of the particle physics community and to present results at various conferences around the world.

I would like to thank the CMS Pixel and DQM groups for taking me on as a member and entrusting me with projects I thought too important for a mere graduate student. Specifically, Marcin Konecki (Warsaw) tutored me in the operation of the early Pixel RawToDigi package, enouraged me to take over its development, and was even available years later to answer the occasional questions I might have. Danek Kotlinski (PSI), Gino Bolla (Purdue), Karl Ecklund (Rice), and Will Johns (Vanderbilt) taught me about the online operation of the Pixel subdetector. Vincenzo Chiochia (Zürich), Petra Merkel (Purdue), Freya Blekman (Brussels), Gavril Giurgiu (Johns Hopkins), Urs Langenegger (PSI), and Viktor Veszpremi (RMKI) oversaw my work in Pixel Offline operations while I was at CERN. Petra Merkel (again!) and Dan Duggan (Rutgers) oversaw my work with Pixel DQM, and they and Tomas Hreus (Brussels) were always available to help me if I had questions while supervising a Tracker DQM shift. In particular, I'm grateful to Vincenzo, Petra, and Danek for first bringing me into the Pixel group, introducing me to the other members, and entrusting me with the development of the Pixel Error and Cluster DQM packages, RawToDigi package, and the ROOT-based analysis of early data used to commission Pixel. They had more confidence in my ability to contribute than I did, and worked with me whenever I had trouble. But that was true to a certain extent with everyone in Pixel, and I'm glad to have been part of that team.

I would like to thank the CMS B-physics analysis group for overseeing the progress of the double J/ψ analysis. Hermine Wöehri (CERN) introduced me to the B-physics group and shepherded the analysis through the approval process from inception to final approval, offering welcome advice and support the entire time. Roberto Covarelli (Rochester) also offered important feedback and leadership in moving the analysis through the approval process. Pietro Faccioli (LIP), Kai Yi (Iowa), and James Russ (Carnegie-Mellon) all offered valuable comments and suggestions as well. Alessandra Fanfani (INFN) not only provided feedback on the analysis, but introduced me to some of the GRID resources I would need for the analysis and helped troubleshoot early problems. The members of my ARC: Daniel Marlow (Princeton), Luca Perrozzi (CERN), Juliana Whitmore (Fermilab), and the chair Nicolo Cartiglia (INFN); all were instrumental in the final approval of the analysis.

A HUGE thank you to Giordano Cerizza, who blazed a trail for me with his PhD research, helped get the double J/ψ analysis off the ground, and has been a great friend since we started graduate school together. Also to Dr. Zongchang Yang for his work with the double J/ψ analysis; he was both an important member of the team and a friend. And thanks to Geri Ragghianti for managing the Newton Cluster, responding to problems right away (even when they appeared late Saturday night or early Sunday morning), and also being a friend.

Last, I would like to thank all of my friends and family who, even if they didn't specifically deal with my analysis, helped make and support the person behind the analysis; their contribution can't be measured. Thank you to my parents James and Judith York, godmother Mai Stuart, aunt Celeste, uncle Bob, and all my extended family in America and England. Also to my close friends: Richmond Chaisiri, Clint Coo, Michael Stakem, Andrew Donnelly, Rob Cannon, Cody Spencer, William Blake, Kwame Webb, Kirk Anderson, Jason and Shimmi Lambert, Merek Chertkow, Matt Musgrave, Matt and Olga Hollingsworth, Will Martin, Anne Brogden, Jay Billings, Chris Smith, Tom Papatheadore, and Leesa Allison. Even if I do a terrible job of keeping in touch sometimes (especially recently), I consider you all to be a part of everything I do, and I wouldn't have made it through such a difficult process without you.

I'd also like to especially mention my grandfather Col. Dantes York, who studied physics before me, and my cousin Jamie Cameron, who is just beginning higher-level physics studies. Granddad, you've been a role-model for me. Jaime, you're one of the smartest people I know and I wish you the best in your future studies.

“A person who never made a mistake never tried anything new.” Albert Einstein

Abstract

The simultaneous production of two J/psi mesons has been significantly observed in proton-proton collisions at a center-of-mass energy of 7 TeV with the CMS detector. The two J/psi mesons are fully reconstructed in their decay to muons. The signal yield is extracted with an extended maximum likelihood fit based on four event variables. A method was developed to correct for detector acceptances and efficiencies based on the measured momenta of the J/psi and their decay muons to maintain the least model dependence possible.

The measurement is performed in an acceptance region defined by the individual J/psi transverse momentum and rapidity. From the measured signal yield of 446 events corresponding to an integrated luminosity of 4.7 inverse femtobarn. The total cross section is found to be 1.49 nanobarn, with 0.07 statistical and 0.13 nb systematic error, and unpolarizaed production was assumed. Most predictions for particle production at the LHC assume dominance of single parton interaction for proton-proton collisions, which can be tested with the final state measured in this analysis. The differential cross section is measured in bins of the double J/psi invariant mass, the double J/psi transverse momentum, and the absolute difference in rapidity of the two J/psi.

The reconstruction of the four charged muon trajectories heavily relies on the Pixel subdetector located close to the beampipe. Systematic studies with cosmic muons and tracks from collision events are presented. The development of the Pixel RawToDigi package, data quality monitoring packages, commissioning studies of Pixel

data and tracks in first collisions, and realistic simulations of decay signals in the pixel subdetector were all performed as a part of this dissertation work.

Table of Contents

List of Tables

List of Figures

Chapter 1

Motivations

Elementary particle physics is the study of fundamental particles and the forces that govern their interactions in an effort to develop a complete description of natural phenomena. The Standard Model (SM) is a quantum field theory that unifies the electromagnetic, weak, and strong nuclear forces under a common theoretical framework. It is based on a limited set of particles: fermions (the fundamental building blocks) and bosons (the force carriers). Measurements performed over more than 40 years agree with the SM to a very high precision within the accessible energy regime. A candidate for the last particle predicted by the model to be responsible for generating the mass of SM particles, the Higgs boson, has recently been found Chatrchyan et al. (2012a); Aad et al. (2012). Furthermore, while the mass of the Higgs candidate is compatible with the SM, it is not predicted by the model and could have much larger values. The electromagnetic, weak, and strong force are expected to converge at energies of about 10^{-15} GeV, but the SM does not predict a common strength for the forces. Many models beyond the SM (eg, based on Supersymmetry), predict new generations of particles that overcome the shortcomings of the SM. The goal of the Large Hadron Collider (LHC) program is to find these new particles at unprecedented high energies in the collision of protons. Once produced, they are identified from decay products detected with an array of several detector technologies placed at collision points around the LHC storage ring.

The SM uses the analytic technique of perturbation theory to predict the production and decay rates of particles due to the strong interaction at high energy to a very high precision. However, it becomes impossible to analytically predict the production and decay rates of particles due to the strong interaction beyond a threshold energy because the strong force behaves asymptotically at that limit (as opposed to the electromagnetic force, which behaves as a continuous function at all energies and distances). Relatively precise calculations of cross sections are published for many modes of particle production, and the dominant production process at the LHC (including for Higgs and other new particle production) is due to interactions between gluons. Gluon fusion is expected to account for most of the simultaneous production of two J/ψ in proton-proton collisions, and the double J/ψ final state can be cleanly reconstructed due to the muon detection and identification capabilities of the CMS detector.

The goal of this analysis is to find the double J/ψ final state with the CMS detector and measure the production cross section. This measurement can be used to evaluate the predictions of different SM interaction models. The correlation between the J/ψ particles is sensitive to multiple parton interations. If found to be significant, predictions for other particle production (including the Higgs) may need to take multiple parton interaction into account. Hence, the analysis also measures differential cross sections as a function of several kinematic variables.

Models also predict that the two J/ψ can be the result of the decay of an intermediate resonance state, such as an η_b particle (composed of a b-quark and anti-b-quark, the groundstate of bottomonium) or a light psuedo-scalar Higgs particle that is not part of the SM. The decay of the η_b particle into two J/ψ in the SM is predicted to be at a rate too low to observe with current luminosity. Hence, any significant resonance would be attributed to physics beyond the SM. Such a resonance search is performed through inspection of the reconstructed double J/ψ invariant mass distribution, looking for an enhancement peak near 9 GeV/c^2.

Chapter 2

Physics Background

2.1 Introduction

This chapter explains the physics concepts relevant to study of double J/ψ production. Section 2.2 gives an overview of the Standard Model, explaining the type of mathematical model employed, the fundamental particles contained, the forces covered, and the predictions the model is capable of making. Section 2.3 goes into more detail about Quantum Chomodynamics (QCD), the theory within the Standard Model that governs the strong nuclear force interactions most relevant to J/ψ production from proton collisions. Section 2.4 discusses potential mass resonances that may be found in the double J/ψ invariant mass distribution and the implications of such a resonance for physics beyond the Standard Model.

2.2 The Standard Model of Particle Physics

2.2.1 The Elementary Particles

All elementary particles can either be classified as *fermions* or *bosons*. Fermions possess half-integer spin and follow Fermi-Dirac statistics, which means no two fermions can simultaneously possess the same quantum numbers (location, charge, spin, energy, etc) Griffiths (2005). Bosons possess integer spin and follow Bose-Einstein statistics, which means there is no limit to how many bosons may possess the same quantum numbers Griffiths (2005). Fermions are the basic building blocks of matter, while the forces occur due to exchange of bosons between fermions. Bosons are therefore considered force mediators, with different bosons responsible for the action of each force.

Fermions are further divided into two categories: *quarks* and *leptons*. Quarks have a fractional electric charge ($+\frac{2}{3}$,$-\frac{1}{3}$) and are color charged, making them subject to the strong force. Quarks cannot exist in isolation due to the magnitude of the strong force, but must rather be bound up in composite particles known as *hadrons* that are color-neutral and have integer electric charge (a phenomenon known as *color confinement*. Protons and neutrons are examples of hadrons, each composed of three quarks. Unlike quarks, leptons have an integer electric charge and no color charge, so they are subject only to the electromagnetic and weak forces and can exist as free particles. Fermions can also be organized into three generations of matter, each generation containing particles of identical electric charge but greater mass than the previous generation. Particles always decay to lower mass states when possible, which makes second and third generation particles exceedingly rare in nature. Particles acquire mass through interaction with the Higgs field, mediated by the Higgs boson Chatrchyan et al. (2012a); Aad et al. (2012). The full array of SM particles along with their classification is given in Figure 2.1 wik (2008).

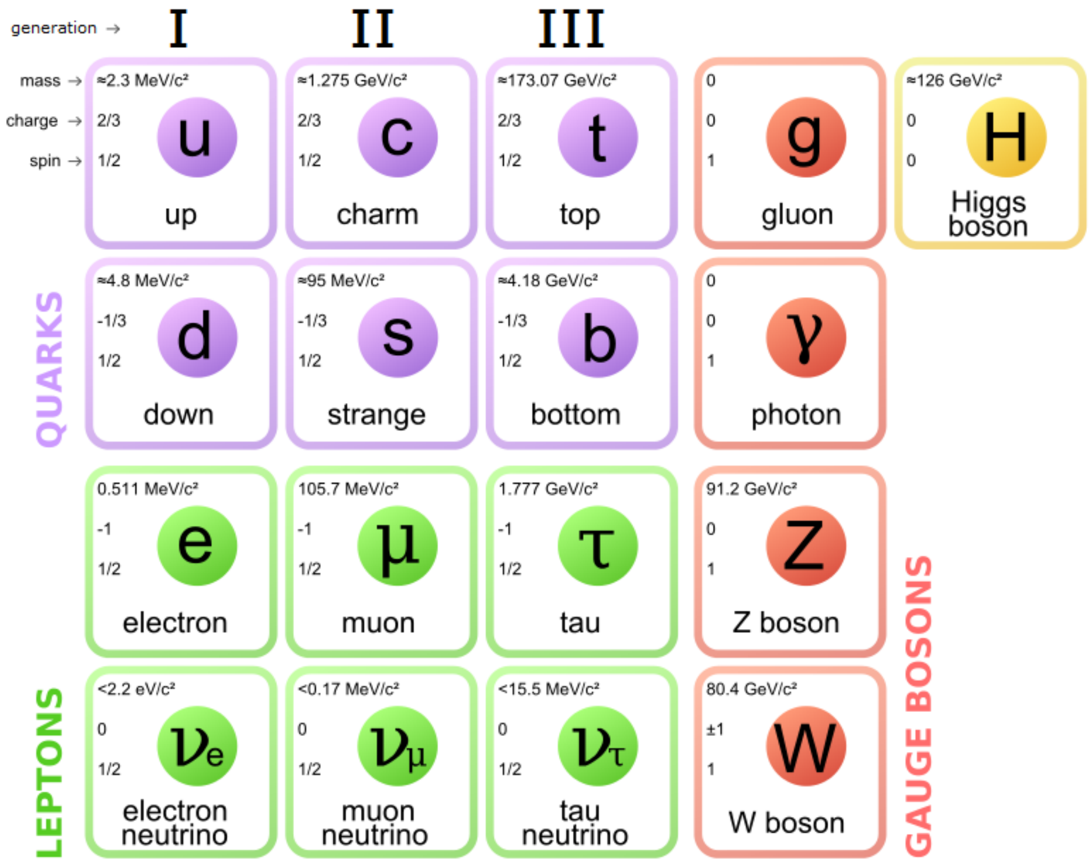

Figure 2.1: The elementary particles contained within the Standard Model. All matter is composed of two types of fermions: quarks (purple) and leptons (green). Fermions are further organized by column into three generations of matter, with higher mass particles at higher generations. The actions of the fundamental forces are due to exchange of bosons (red) between fermions. Particles acquire mass through interaction with the Higgs field, mediated by the recently discovered Higgs boson (yellow).

The six types (flavors) of quarks grouped by generation are: up (u) and down (d), charm (c) and strange (s), top (t) and bottom (b). The charm, bottom, and top quarks are referred to as heavy quarks because they have more than an order of magnitude greater mass than the lighter quarks (the top quark has approximately the mass of a gold atom). There are three lepton flavors named for the charged lepton they describe: electron, muon, and tau. For each charged lepton, there is a corresponding uncharged neutrino of the same flavor (electron neutrino, muon neutrino, and tau neutrino). For each fermion described in Fig. 2.1, there is also an oppositely charged anti-particle denoted by a bar above the symbol (for example, $\bar{c}$ indicates an anti-charm quark, which has an electric charge of $-\frac{2}{3}$). Hadrons composed of three quarks or three anti-quarks are called *baryons* or *anti-baryons* respectively, while hadrons composed of a quark/anti-quark pair are called *mesons*.

2.2.2 The Fundamental Forces

Scientists have identified four fundamental forces: gravity, electromagnetism, the strong force, and the weak force. Although gravity is relevant at the macroscopic scale because it is universally attractive, it is actually the weakest of the four forces at the microscopic scale and its effects cannot be measured in elementary interactions. The other three forces are described by the Standard Model and summarized in Table 2.1. The effective range of the strong force is limited by color confinement to about the size of a hadron. The effective range of the weak interaction is limited by the mass of its boson mediators. The electromagnetic force has no limit to its effective range since it is mediated by a massless boson (the photon) and electric charge is not subject to confinement. In practice, opposite electric charges tend to cancel each other out at the macroscopic scale, though photons (packets of light) can still travel interstellar distances.

The SM is a Quantum Field Theory (QFT), which means it describes all interactions as an exchange of particles and all particles as excited states of a quantum

Table 2.1: The fundamental interactions described by the Standard Model.

Interaction	Mediator	Effective Range	Example in Nature
Strong	gluon	10^{-15} /m	Binds hadrons and nuclei
Weak	W,Z boson	$< 10^{-17}$ /m	Enables beta decay of neutron
Electromagnetic	photon	$\infty, \frac{1}{r^2}$	Binds atoms and molecules

field (a field with values associated to points in space and time). Particles that exist only to mediate an interaction are called *virtual particles*, and may briefly exist at an energy below the mass described in Fig. 2.1. The brief existence of a particle at a forbidden energy is due to the Heisenberg uncertainty principle $\Delta E \cdot \Delta t \geq 1$ (in Natural Units), which implies large energy fluctuations at very short time scales. The Standard Model is broken down into several QFTs describing different interactions and following the requirements of *gauge invariance* and *renormalizability*. Gauge invariance requires that the theory's rules of interaction do not change under allowed transformations, which means the forces operate in the same manner at any point in space and time and are only determined by the fields and conserved quantities of the theory. Renormalizability requires that the theory be able to scale its description of interactions to different energies, allowing for finite predictions of interaction at real-world energy scales. Heisenberg uncertainty also establishes the relationship between energy, time, and distance: $\Delta E = \frac{1}{\Delta t} = \frac{1}{\Delta x}$ for forces operating at the speed of light, so the renormalization scale that determines the strength of a force can be described in terms of energy, time, or distance.

The strong force is responsible for binding quarks into hadrons and hadrons into atomic nuclei, making it the basis for nuclear power and nuclear weapons. The QFT describing the strong force is called Quantum Chromodynamics (QCD). The strong force behaves differently at very short distances (less than 1 fm, the approximate diameter of a hadron) compared to longer distances (1-3 fm, the distance between neighboring hadrons in a nucleus). The strong interaction becomes weaker at very short distances/high energies and allows quarks and gluons within a hadron to be treated as free particles, a phenomenon known as *asymptotic freedom*. The scale at which asymptotic freedom dominates is called the QCD energy scale, Λ_{QCD}, and corresponds to interaction distances ≤ 1 fm and energies ≥ 200 MeV. At this scale, a hadron may be modeled as a collection of several different kinds of *partons*: *valence quarks*, gluons, and *sea quarks*. The valence quarks are the three quarks (in the case of a baryon) or quark/anti-quark pair (in the case of a meson) needed to form the hadron and determine its quantum numbers. Gluons carry the strong interaction between the quarks and can split to form sea quarks, short-lived $q\bar{q}$ pairs that can interact in collisions but do not determine the quantum numbers of the hadron. An example of the structure of a proton at this energy scale is illustrated in Fig. 2.2. As energy scale increases, sea quarks and gluons are increasingly likely to dominate interactions. In the 7 TeV collisions of the Large Hadron Collider, the majority of interactions between colliding protons are predicted to be with gluons and the majority of quark interactions are predicted to be with sea quarks.

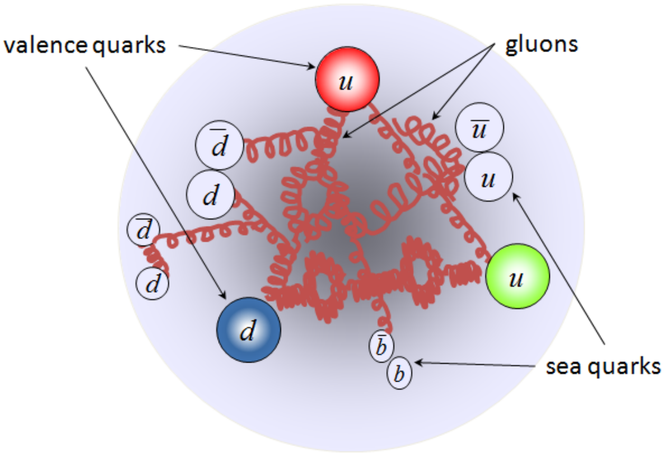

Figure 2.2: Example of a proton's internal structure at the QCD energy scale.

Protons have a *uud* valence quark structure, as Fig. 2.2 illustrates. But two *u*-quarks with the same quantum numbers in the same location would violate the Pauli Exclusion Principle. To avoid this, a new quantum number called color charge was introduced Greenberg (1964). The three types of color charge are red, green, and blue, and they each have a corresponding anti-charge (anti-red, anti-green, and anti-blue). The strong force only operates between color charged objects, which include quarks (possessing one color charge), anti-quarks (possessing an anti-color charge), and gluons (possessing a color and an anti-color charge). As with electric charge, color charge may be transferred in particle interactions but must be conserved. All three colors combine to make a color-neutral state, as do all three anti-colors or a color with its corresponding anti-color.

At distance scales higher than Λ_{QCD}, only the valence quarks need to be considered for strong interactions. At this scale the strong force is too powerful to allow any but color-neutral objects to exist, resulting in color confinement. If two quarks are separated beyond this scale, the strong interaction between them will have sufficient energy to re-enter the Λ_{QCD} regime and materialize quark/anti-quark pairs from the vacuum (following energy and charge conservation). These free quarks will then congeal into color-neutral hadrons, a process known as *hadronization*. Although hadrons are color-neutral, the quarks within a hadron can still interact with the quarks of nearby hadrons up to a distance of around 1-3 fm, similar to the manner in which electric dipoles can align and attract nearby dipoles. The strong interaction between nearby hadrons is known as the residual strong force or strong nuclear force because it is responsible for binding together the nucleus of atoms.

The electromagnetic force binds electrons to the nucleus of an atom and binds atoms together into molecules, making it responsible for most of the interactions people perceive every day such as chemical reactions, electric current flow, and light emission/absorption. The QFT that describes the electromagnetic force is called Quantum Electrodynamics (QED), mediated by exchange of massless photons between electrically-charged fermions. At distances greater than the femtometer scale, the electromagnetic force is the only SM force relevant to particle interactions.

The weak force is the shortest range force in the Standard Model, but is important for enabling several types of particle decays that would be impossible otherwise (the most common example in nature is the beta decay of a neutron into a proton).

The weak interaction is parameterized by Quantum Flavordynamics (QFD) theory and was not described by a QFT until Glashow, Weinberg, and Salam Glashow (1961); Salam (1968); Weinberg (1967) demonstrated that the electromagnetic and weak interactions can be seen as consequences of the same force, now termed the electroweak force and described by Electroweak Theory (EWT).

The range of weak interaction is so short because it is mediated by very massive charged $W^{\pm}$ bosons and neutral Z^0 bosons, unlike the other SM forces that have massless boson mediators. Weak interactions are the only means for a particle to decay in a way that changes flavor and charge. In addition, a hadron decaying via the weak interaction does not have the same likelihood of decay if its quark content are inverted in space (violating *parity*, also called P symmetry) or replaced with their respective anti-particles (violating *charge-parity*, also called CP symmetry). Only the weak interaction can violate P and CP symmetry. Because the weak interaction is so weak, particles that can only decay via the weak interaction have a much longer lifetime. For example, a neutral pion (π^0, composed of a $u\bar{u}$ or $d\bar{d}$ pair) can decay electromagnetically, resulting in a lifetime on the order of 10^{-16}s. But a charged pion ($\pi^{\pm}$, composed of a $u\bar{d}$ or $\bar{u}d$ pair) can only decay weakly, resulting in a lifetime on the order of 10^{-8}s (orders of magnitude longer than the neutral pion).

As with classical interactions, SM interactions require the sum electric charge, color charge, energy, and momentum of final-state fermions to match that of initial-state fermions. In addition, total *baryon number* and *lepton number* must be conserved. Baryon number is a quantum number given to baryons; for baryons composed of matter quarks it is $+1$ and for baryons composed of anti-matter quarks it is -1. Lepton number is a quantum number given to leptons $+1$ for leptons and -1 for anti-leptons, and different for each lepton flavor (ie, electron number must be conserved in addition to muon number and tau number). Fig. 2.3 illustrates the basic interactions of QCD and Fig. 2.4 and Fig. 2.5 illustrates the basic interactions of Electroweak theory. Each diagram can be read with any one or two adjacent particles

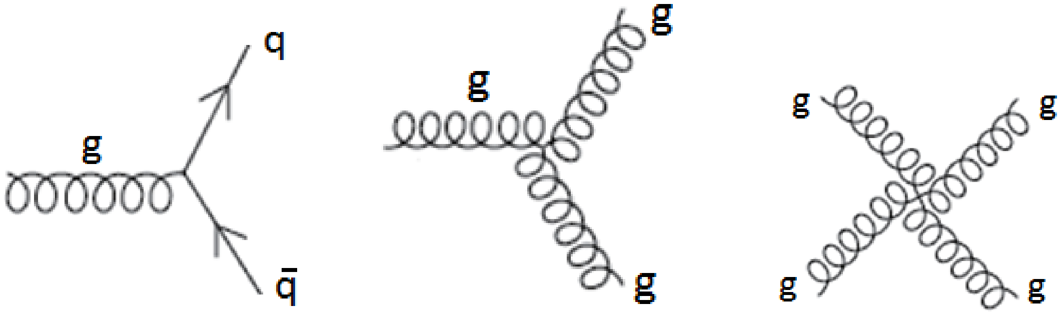

(a) A gluon can split into a quark and corresponding anti-quark, a quark and corresponding anti-quark can annihilate into a gluon, and a quark can emit or absorb a gluon (changing the color charge and energy of the quark).

(b) An excited gluon can emit another gluon. Conversely, two gluons can combine into one.

(c) A pair of gluons can exchange quantum numbers.

Figure 2.3: Basic QCD interactions.

taken as the initial state, and all physical interpretations are described in the caption below the diagram.

The diagrams in Fig. 2.3, Fig. 2.4 and Fig. 2.5 represent basic interactions that are the building blocks of the larger processes at work in all SM interactions. Any interaction is possible so long as the reactants and products couple to the appropriate force and obey the conservation rules, and those interactions are more likely at distance and energy scales where the force is very strong. A meson decay could be described by 2.3a, with a $q\bar{q}$ pair annihilating into a gluon and the gluon splitting into a new $q\bar{q}$ pair and hence new meson. A meson decay could similarly be described by Fig. 2.4a, 2.5a, and 2.5b because the $q\bar{q}$ pair couple to all three of the forces, though a $q\bar{q}$ pair of different flavor could only be decayed through Fig. 2.5b due to conservation requirements (hence the relatively long lifetime of mesons composed of different flavor quarks based on the weakness of the weak interaction). A pair of sea quarks (also called a quark loop) are modeled from the interaction in Fig. 2.3a,

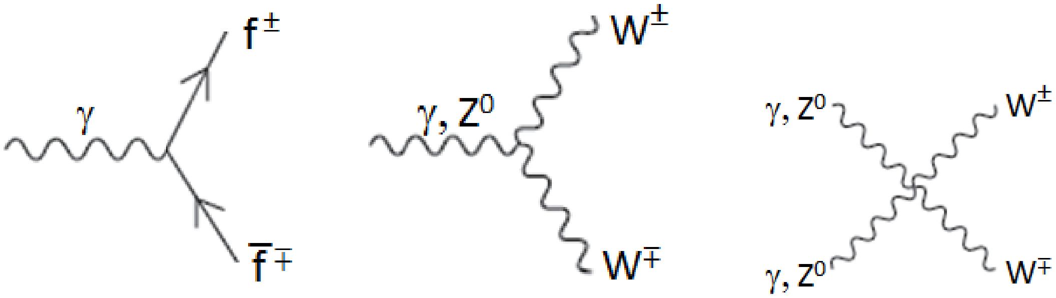

(a) A photon can split into any electrically charged fermion and corresponding anti-fermion, any electrically charged fermion and corresponding anti-fermion can annihilate into a photon, and any electrically charged fermion can emit or absorb a photon (changing the energy of the fermion).

(b) A photon or Z boson can split into a pair of oppositely charged W bosons, oppositely charged W bosons can combine into a photon or Z boson, a charged W boson can emit a or absorb a photon or Z boson (changing its energy), and a photon or Z boson can emit or absorb a W boson (gaining charge and changing its energy).

(c) A pair of neutral electroweak bosons can combine into an oppositely charged pair of W bosons (or vice-versa).

Figure 2.4: Basic EM interactions.

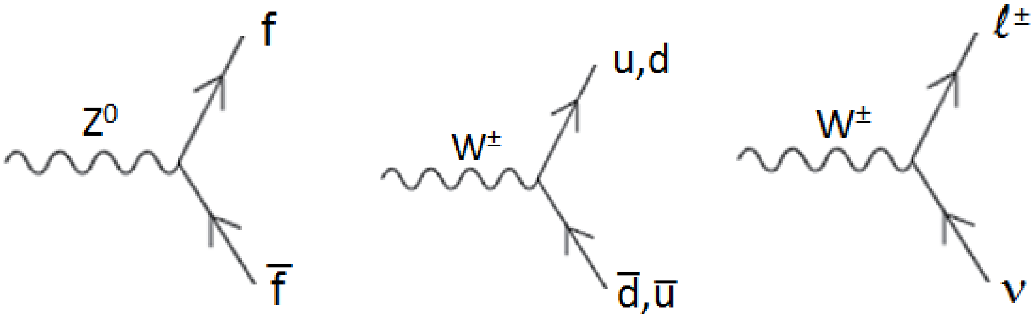

(a) A Z boson can split into any fermion and corresponding anti-fermion (including uncharged fermions), any fermion and corresponding anti-fermion can annihilate into a Z boson, and any fermion can emit or absorb a Z boson (changing the energy of the fermion).

(b) A positively charged W boson can split into any up-type quark and down-type anti-quark, a negatively charged W boson can split into any down-type quark and up-type anti-quark, these quarks can combine into a W boson, and a quark can emit or absorb a charged W boson (changing the electric charge, flavor, T_3, and energy of the quark).

(c) A positively charged W boson can split into a neutrino and charged anti-lepton, a negatively charged W boson can split into a charged lepton and anti-neutrino, these leptons can combine into a W boson, and a lepton can emit or absorb a charged W boson (gaining or losing electric charge and changing the lepton's T_3 and energy).

Figure 2.5: Basic Weak interactions.

with a gluon splitting into a $q\bar{q}$ pair, then reconverging to a gluon final state. Other fermion and boson loops can similarly be built up from the other interactions shown, and these loops play a larger role in interactions as energy scale increases.

At the LHC, protons collide with a center-of-mass energy of 7 TeV. This energy is distributed among their partons, and each parton has a chance to interact with the partons of a colliding proton to produce new particles. A pair of J/ψ particles can be produced from a single interaction in a Single Parton Scattering (SPS) event, as depicted in Fig. 2.6. Alternately, two separate interactions between the protons could each produce a J/ψ in a Double Parton Scattering (DPS) event, depicted in Fig. 2.7. One of the goals of this analysis is to measure the simultaneous production of two prompt J/ψ in a manner that discriminates between SPS and DPS production.

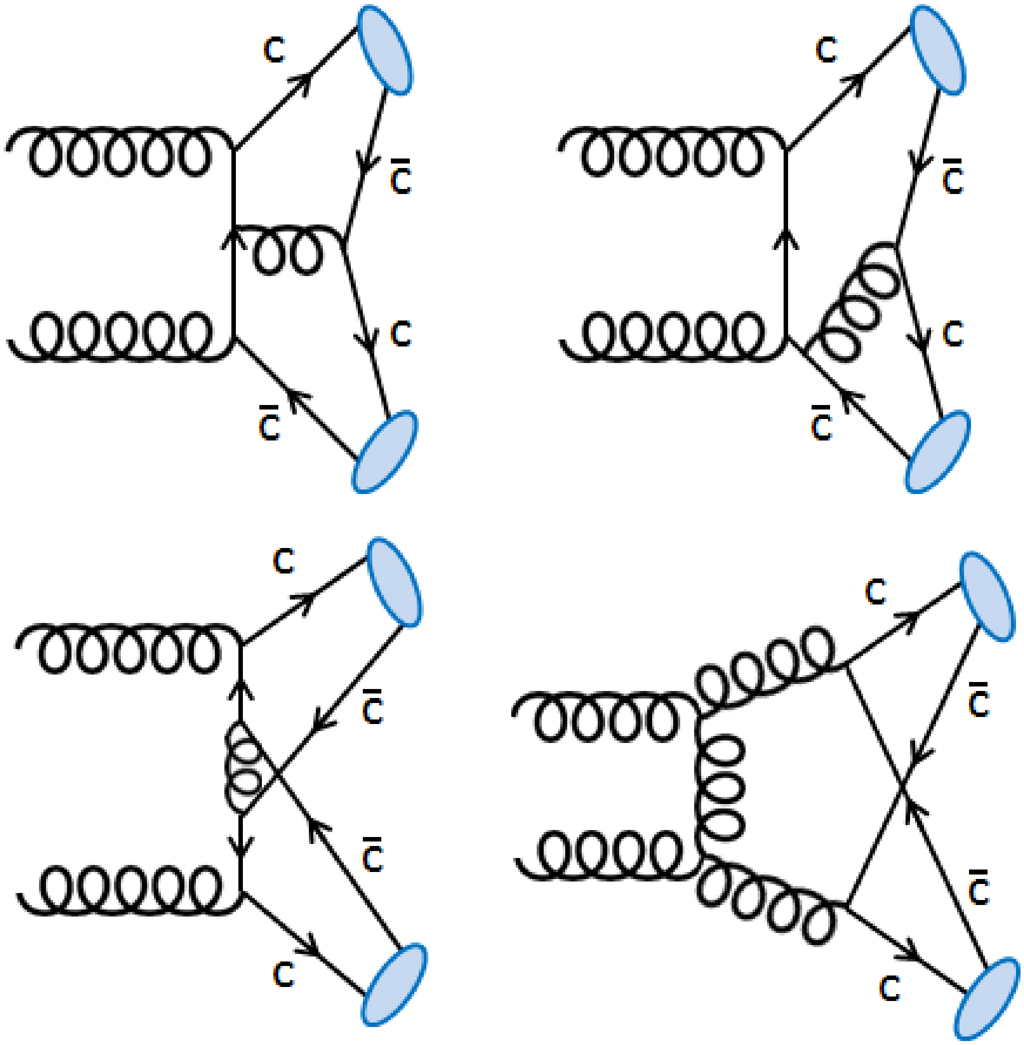

Figure 2.6: Examples of prompt double J/ψ production through Single Parton Scattering (SPS). In the cases illustrated, two gluons fuse to directly produce the double J/ψ state.

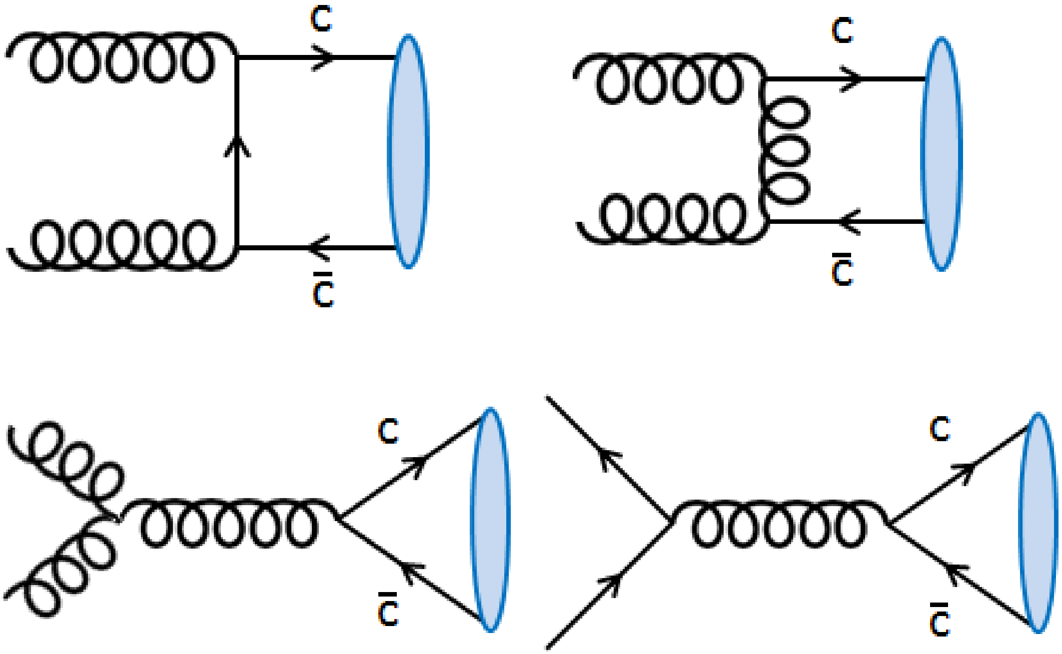

Figure 2.7: Examples of processes that lead to prompt single J/ψ production through gluon fusion or quark annihilation. Any two of these interactions could occur more than once between the partons of colliding protons.

2.3 Quantum Chromodynamics and Particle Production at the LHC

This section discusses important concepts behind the Quantum Chromodynamics (QCD) approach used to describe particle interactions and predict prompt double J/ψ production at the LHC.

2.3.1 QCD Interactions at High Energy

The strong coupling constant α_s determines the strength of strong force interactions and is called a running coupling constant because it is dependent on the energy scale of the interaction. At energies high enough for asymptotic freedom, the strong coupling can be approximated $\alpha_s \approx \frac{1}{\beta_0 \ln(E^2/\Lambda_{QCD}^2)}$, where β_0 is a constant and Λ_{QCD} is the QCD scale, measured to be $\Lambda_{QCD} = 217^{+25}_{-23}$ MeV Beringer et al. (2012). As interaction energy drops to Λ_{QCD}, the strong coupling blows up and color confinement takes over. But at higher energies, the strong coupling can be approximated using a perturbative expansion. Perturbative QCD is currently the most predictive analytic solution to QCD equations at high energies.

When hadrons collide at high energy, their partons may interact via the strong force to produce hard, semi-hard, and soft scattering processes. Hard scattering processes are those with an interaction energy on the order of tens of GeVor higher, semi-hard scattering processes are those with an interaction energy on the order of a few GeV, and soft scattering processes are those with an interaction energy on the order of tens of MeV. Semi-hard and soft scattering processes may produce light hadrons with low momentum, the so-called *underlying event* (UE). But hard scattering processes are the only interactions with enough energy to result in double J/ψ production detectable by CMS and are the interactions best described by Perturbative QCD.

The process of hard scattering between hadrons is conceptually factorized into three parts: each hadron is treated as a distribution of partons, each parton within a hadron is considered an unbound particle with a chance to interact with any parton in the other hadron, and every such parton-level interaction has a chance to result in various end-state hadrons after hadronization. Mathematically, this conceptual treatment translates to the cross section described in Eq. 2.1:

$$\frac{d\sigma}{dX} = \sum_{j,k} \int_{\hat{X}} f_j(x_1) f_k(x_2) \, \frac{d\hat{\sigma}_{jk}}{d\hat{X}} \, F(\hat{X} \to X) \tag{2.1}$$

where:

- X is a hadronic final state kinematic variable of interest (examples below);
- the sum over i and j is over parton types inside the respective hadrons;
- the function $f_j(x)$ is a parton distribution function (PDF), representing the number density of parton type j with momentum fraction x;
- $\hat{X}$ is a parton-level kinematic variable corresponding to X (before hadronization);
- $\hat{\sigma}_{jk}$ is the parton-level cross section, differential in $\hat{X}$;
- $F(\hat{X} \to X)$ is a transition function that weighs the probability that the partonic state $\hat{X}$ transitions to the final hadronic state X.

Factorizing the process in this manner allows different models to be developed and interchanged to describe each step. For example, different PDFs can be developed and paired with the same partonic interaction likelihoods and hadronization models to provide different predictions of production.

QCD interactions are typically measured with respect to the following kinematic variables (X) that describe the momentum and angular ranges of interaction products:

- **transverse momentum** (p_{T}): the component of the momentum in the plane perpendicular to the direction of the collisions,

- **pseudorapidity** (η): spatial coordinate that describes the angle of a particle relative to the beam direction and defined by the equation

  $$\eta = -\ln\left[\tan\left(\frac{\theta}{2}\right)\right], \tag{2.2}$$

  where θ is the angle between the particle momentum $\vec{p}$ and the beam direction.

- **rapidity** (y): defined as

  $$y = \frac{1}{2}\ln\left(\frac{E + p_{\mathrm{L}}}{E - p_{\mathrm{L}}}\right) \tag{2.3}$$

  where E is the energy of the particle and $p_{\mathrm{L}}$is the momentum along the colliding hadron beam direction. If the particle is traveling close to the speed of light, or the mass of the particle is negligible compared to the energies involved in the process, the pseudorapidity will be numerically close to the rapidity of the particle.

2.3.2 Color Singlet and Color Octet States

Real particles must exist in a color neutral state due to color confinement. Therefore, mesons must possess $r\bar{r}$, $b\bar{b}$, or $g\bar{g}$ color charges. Since the exact color charge content cannot be measured, it is described as a superposition of these possibilities, $(r\bar{r} + b\bar{b} + g\bar{g})/\sqrt{3}$, known as a *color singlet* (CS). Gluons exist only as virtual particles and are experimentally observed not to operate at long range, so gluons do not exist in a CS state. Rather, gluons exist as a *color octet* (CO) described by the eight color superpositions in Table 2.2.

Color singlets and octets are also useful in describing the transition function $F(\hat{X} \to X)$ of Eq. 2.1. CS models assume the final hadronic state must be produced as a color singlet. CO models require the hadronic state to be produced as a color

Table 2.2: Eight color superpositions of the gluon.

$(r\bar{b} + b\bar{r})/\sqrt{2}$	$-\imath(r\bar{b} - b\bar{r})/\sqrt{2}$
$(r\bar{g} + g\bar{r})/\sqrt{2}$	$-\imath(r\bar{g} - g\bar{r})/\sqrt{2}$
$(b\bar{g} + g\bar{b})/\sqrt{2}$	$-\imath(b\bar{g} - g\bar{b})/\sqrt{2}$
$(r\bar{r} - b\bar{b})/\sqrt{2}$	$(r\bar{r} + b\bar{b} - 2g\bar{g})/\sqrt{6}$

octet and then decay to a color singlet via soft gluon emission. CO models predict greater production cross sections at high p_{T} than CS models.

2.4 Resonant Production

A resonance content is predicted for the double J/ψ final state. The bottomonium ground-state meson η_b is expected to decay into two J/ψ mesons in analogy to the η_c charmonium ground-state that decays into two ϕ-mesons Collaboration (2006). However, explicit calculations based on Nonrelativistic QCD (NRQCD) Braaten et al. (2001); Maltoni and Polosa (2004); Jia (2008) predict this decay mode to be highly suppressed, so any observation could indicate the limitations of present NRQCD approaches. Other predicted resonant states that could decay into two J/ψ mesons are exotic tetra charm-quark states Berezhnoy et al. (2011). Furthermore, a CP-odd Higgs e.g. in Next-to-Minimal Supersymmetric Standard Models (NMSSM) Dermisek and Gunion (2005) is predicted with mass close to the η_b meson. The mixing between those two states can alter the behavior of η_b with respect to QCD predictions Domingo et al. (2009); Domingo (2011). No evidence for the CP-odd Higgs was found by CMS in the $\mu^+\mu^-$ invariant mass spectrum between 5.5 GeV/c^2 and 14 GeV/c^2 Chatrchyan et al. (2012b). The η_b state has been observed in radiative transitions with the BaBar experiment and observed to have a mass of about 9.4 GeV/c^2 and an assumed decay width, Γ_{η_b}, of about 10 MeV/c^2 Aubert et al. (2009). The η_b decay to two J/ψ was probed with the CDF detector, which established an upper limit of 3 events in 1.1 fb^{-1} of proton/anti-proton collisions at 1.96 GeV Collaboration (2006).

Chapter 3

Experimental Setup

3.1 The Large Hadron Collider

The search outlined in the previous chapter requires parton interactions significantly in excess of 6.2 GeV (the rest energy of two J/ψ mesons). The highest energy parton within a proton has about one-third of the total kinetic energy of the proton. In order to achieve TeV scale interactions between protons, the protons must be accelerated to multiples of a TeV. In addition, high beam intensities and collision rates are neeeded to compensate for the low double J/ψ cross section. The Large Hadron Collider (LHC) Brning et al. (2004) Evans and Bryant (2008) is a proton-proton collider located at the European Organization for Nuclear Research (CERN [*]) near Geneva, Switzerland. The LHC was designed to:

- accelerate two parallel proton beams in opposite directions, each to a final design energy of 7 TeV;
- maximize the chance of proton collisions every time the beams cross (measured by *cross section*);

---

[*] Originally Conseil Européen pour la Recherche Nucléaire, now, Organisation Européen pour la Recherche Nucléaire

- collide a large number of protons frequently, continuously, and over a long period of time (measured by *luminosity*);

The LHC itself is a proton storage ring that recycles the protons in each beam to allow it to operate persistently, with minimal downtime, and with minimal loss of protons (only possible because most interactions are between the sea quarks and gluons within a proton rather than the valence quarks, so the proton is usually not destroyed by collisions). The beams are steered around their circular path by $1,232$ dipole magnets, while 392 quadropole magnets around the path serve to regularly focus the beams (preventing proton loss and increasing chance of interaction). To further increase the likelihood of collision, the protons are clustered in evenly spaced bunches and timed so that a bunch from each beam passes through the beam crossing points at the same time.

The LHC is housed deep underground in tunnels originally excavated for the Large Electron-Positron Collider (LEP) and is able to repurpose much of the earlier project's infrastructure. Figure 3.1 depicts the accelerator complex at CERN, as well as the locations of the four detectors located at the four points of beam crossing along the LHC ring. The proton beams are built in steps, each step designed to successively boost the energy of the protons. First, a linear proton accelerator (LINAC 2) generates 50 MeV protons. The protons are fed into a Proton Synchrotron Booster (PSB), where they are accelerated to 1.4 GeV. A Proton Synchrotron (PS) then boosts them to 26 GeV, followed by a Super Proton Synchrotron (SPS) that boosts them to 450 GeV. In the final step, the protons are injected over a period of about 4.5 minutes into the LHC ring, where they are accelerated for about 20 minutes to reach their final energy. The protons from a single injection cycle can sustain collisions at the four intersection points for up to 24 hours. Each experiment is located at an intersection point, with the Compact Muon Solenoid CMS Collaboration (2006a); Chatrchyan et al. (2008) (CMS) detector located at Point 5 (P5). CMS is a general

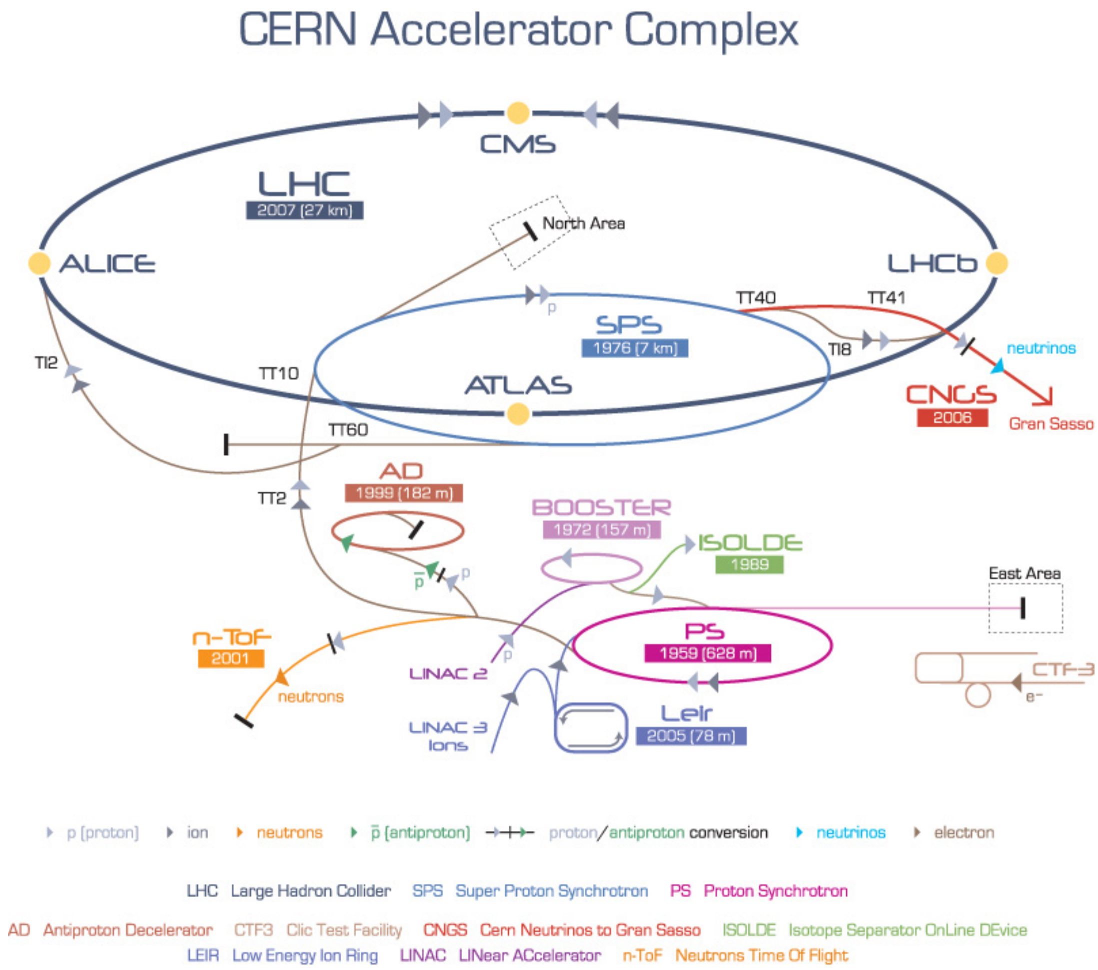

Figure 3.1: The accelerator chain at CERN. The arrows show the direction of proton beams in the accelerators and the energy of the beam at these points. Filled circles show the locations of the four major detectors on the LHC (utility insertions are not shown).

purpose experiment whose main goals are to explore a wide range of physics at the TeV scale.

Table 3.1 shows the LHC operating conditions for most of the 2011 period of operation as well as the original design values. The design energy is expected to be reached in 2015.

Table 3.1: Summary of LHC operating conditions during the 2011 run period along with the original design values.

Parameter	2011 Operation	Design Value
Beam energy E_{beam} (TeV):	3.5	7
Number of bunches per beam n_b:	1380	2808
Number of protons per bunch N_p:	$\sim 10^{11}$	1.15×10^{11}
Time between collisions (ns):	50	25
Cross section σ (cm^2):	$\sim 10^{-25}$	10^{-26}
Peak luminosity $\mathcal{L}$ ($\mathrm{cm}^{-2}\mathrm{s}^{-1}$):	$10^{33} - 10^{34}$	1×10^{34}

The LHC is described in more detail here in three sections: Section 3.1.1 describes proton acceleration, Section 3.1.2 describes the magnet systems that steer and focus the beams, Section 3.1.3 describes the machine luminosity. The CMS experiment is introduced in Section 3.2.

3.1.1 Acceleration

The LHC program makes use of accelerators already in place at CERN. The proton beam is created from a bottle of compressed hydrogen gas, shown in Figure 3.2. Hydrogen atoms from this gas cylinder are injected into the plasma source chamber of the LINAC 2, shown earlier in Figure 3.1. A hydrogen atom consists of a single electron orbiting a proton, so the electrons in the hydrogen source are stripped away to leave proton ions suitable for acceleration.

A Radio-Frequency (RF) cavity is a metallic chamber supplied with a time-dependent voltage to create an EM field that oscillates (changes direction) at a resonant frequency. Charged particles (eg, the protons) moving through the RF cavity are accelerated by the EM field. The RF cavities are separated from each

Figure 3.2: The source of protons for the LHC.

other by a field-free zone to allow particles to freely drift while the EM field reverses direction. The setup of RF cavities in the LHC is depicted in Fig. 3.3. The length of the field-free zones and the timing of the voltage are chosen to accelerate particles to a specific velocity. A particle moving below this velocity receives an overall boost from the EM field, a particle moving above this velocity is slowed by the EM field, and a particle traveling at exactly this velocity is not affected by the field. The spacing of the RF cavities also serves to group the protons into bunches. Each stage of proton acceleration utilizes RF cavities to bring the protons to a specified energy.

As the protons are initially non-relativistic, the lengths of the field-free regions in LINAC 2 vary to account for the rapidly changing velocity. The length remains constant for the relativistic protons in the later stages, a necessary condition in order to circulate the protons multiple times around an accelerator ring. In the ring accelerators, the frequency in the cavity is an integer multiple of the revolution frequency (harmonic number). The virtual positions occupied along the LHC circumference by the bunches of protons are called buckets. Each bunch can contain

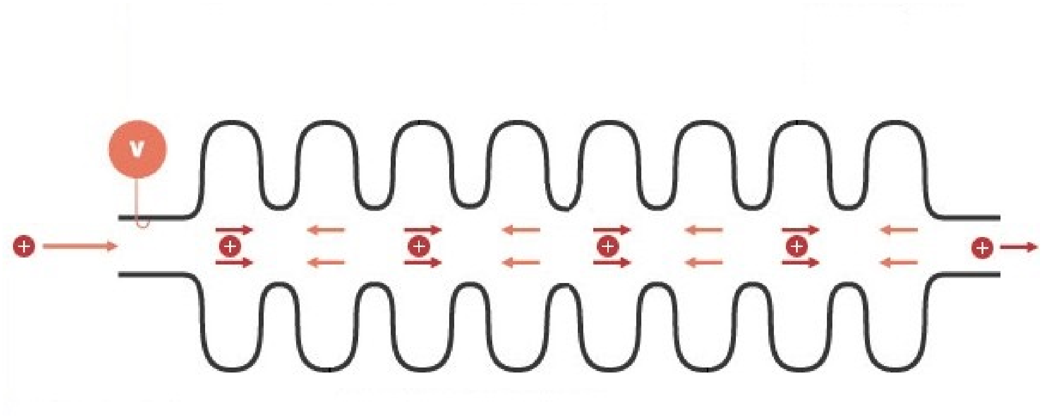

Figure 3.3: Illustrates the function of the eight RF cavities used per proton beam of the LHC, which serve to accelerate protons to a specific energy and sort the protons into bunches.

up to $\sim 10^{10}$ protons. For the LHC, 2808 bunches are positioned in the buckets to provide a spacing of 25 ns.

The LINAC 2 generates 50 MeV protons and feeds them into the Super Proton Synchrotron (PSB), the first of the ring accelerators. The PSB boosts the beam to 1.4 GeVand separates it into well-defined bunches of $\sim 10^{10}$ protons each spaced a minimum of 300 ns apart. These bunches are then transferred to the Proton Synchrotron (PS). Two batches, containing a total of seven bunches, are accelerated for several revolutions to reduce the spacing between bunches by increasing the number of harmonics in the ring. The protons are accelerated further to an energy of 25 GeV, while the beam is split up in steps using the RF on higher harmonics until 72 bunches of $\sim 10^{11}$ protons each are spaced by 25 ns. Those are transferred into the Super Proton Synchrotron (SPS) that accelerates them to an energy of 450 GeV and, finally, injects them into the LHC, both in a clockwise and anti-clockwise direction. The total filling time is about five minutes per LHC ring. The bunches of protons are accumulated for up to 20 minutes in the LHC at the 450 GeV injection energy. The RF cavities in the LHC ring are able to provide 55 GeV/s of power, and the LHC ramps the beams to their final energy within 25 minutes of injection.

3.1.2 Beam Steering and Focus

A charged particle moving through a magnetic field experiences a Lorentz force perpendicular to its direction of motion and the direction of the field. If the magnetic field is homogenous, the particle will follow a circular path. The path's radius of curvature (r) can be determined by setting the centripetal and Lorentz forces equal to one another, resulting in Equation 3.1).

$$r = 0.3 \cdot \frac{p}{q \cdot B} \tag{3.1}$$

Here p is the particle's momentum (in GeV/c), q is the particle's charge (in electrons), and B the magnetic field (in Tesla). This principle is applied in the design of the ring accelerators at CERN. Dipole magnets steer the beams into circular orbits while quadropole magnets focus them, preventing dispersion and allowing the protons to be re-used after collisions. The dipole magnets of the LHC have a very high field strength of 8.3 T, necessary to fit the LHC into tunnels originally built for the lower energy LEP. The magnetic field is generated by several blocks of superconducting niobium-titanium coils running $11,850$ A of current and cooled to 1.9 K by superfluid helium.

The LHC has two proton beams, each running in parallel but opposite directions and separated by only 20 cm. In order to steer both beams along the same path, the magnetic field of the dipole magnets must be inverted over one beam with respect to the other. This 2-in-1 field configuration is achieved by reversing the direction that the superconducting coils are wound around each beam, allowing the same current to flow in opposite directions and create an inverted magnetic field. This configuration is shown in Figure 3.4.

A quadrupole magnet can focus the beam along one axis, so groups of two quadrupole magnets rotated 90 degrees relative to one another are used to focus the beams in the plane normal to their direction. Higher order multipole magnets are also used to provide higher order corrections to the beam. Table 3.2 gives the

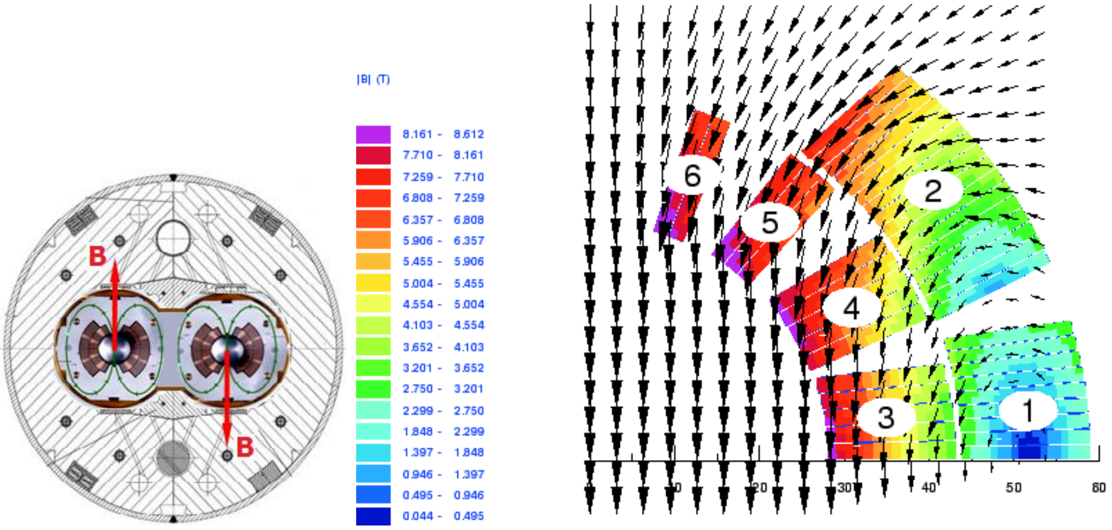

Figure 3.4: The image on the left shows a cross section of a dipole magnet around the LHC beampipe, with a 2-in-1 magnetic field configuration. The image on the right shows a quarter of a dipole aperture, with the 6 superconducting blocks and magnetic field strength indicated.

number of dipoles, quadrupoles, and higher order multipole magnets installed along the LHC ring.

Table 3.2: Magnets installed at the LHC.

Number of poles	Number of magnets
Dipoles	1232
Quadrupoles	858
Higher order multipoles	~ 7200

3.1.3 Luminosity

Luminosity ($\mathcal{L}$) is a measure of how many particles an accelerator can throw into collisions, given as a rate per unit area and per unit time. Cross section (σ) is a measure of how likely it is for two particles to interact, given as an effective area. The rate (R) at which colliding particles will interact is therefore a product of these two values:

$$R = \mathcal{L}\,\sigma \tag{3.2}$$

The luminosity is determined by accelerator parameters following the relation:

$$\mathcal{L} = \frac{f N_p^2 n_b}{4\pi\sigma_x\sigma_y} \cdot \left(\sqrt{1+\left(\frac{\theta_c\sigma_z}{2\sigma^*}\right)^2}\right)^{-1} \tag{3.3}$$

where N_1 and N_2 are the number of protons in each bunch for beam 1 and beam 2, n_b is the number of colliding bunches in the beams, f is the bunch crossing frequency, $\sigma_{x,y,z}$ is the width of the beam in x, y, and z assuming a Gaussian density in those directions, θ_c is the crossing angle of the beams, and σ^* is the transverse beam size at the point of crossing. For most of the 2011 running, the instantaneous luminosity was $\mathcal{L} \sim\ 10^{33} - 10^{34}\ \text{cm}^{-2}\text{s}^{-1}$.

The time integral of the instantaneous luminosity ($\int \mathcal{L}$) is used to describe the total amount of data collected in an experiment. The total integrated luminosity available for this analysis was $4.73 \pm 0.12\ \text{fb}^{-1}$. The total number of events observed in a particular reaction is given by

$$N = \sigma \int \mathcal{L} dt \tag{3.4}$$

The rate of particle production is too high for CMS to record all of the collision events it detects. Thus, a trigger is employed to record only events with indications of interesting physics. This analysis utilizes an unprescaled muon trigger path designed to achieve the highest efficiency for J/ψ + muon searches during the 2011 campaign. This trigger requires the presence of at least three muons, two of which must be oppositely charged and within the dimuon invariant mass range.

3.2 The Compact Muon Solenoid

The Compact Muon Solenoid (CMS) CMS Collaboration (2006a); Chatrchyan et al. (2008) is one of two general-purpose particle detectors located at one of the four interaction points of the LHC. It is designed to explore a wide range of physics in proton-proton collisions at center-of-mass energies up to 14 TeV and interaction rates of 40 MHz as bunches collide every 25 ns, with up to 20 proton-proton collisions occurring simultaneously. The CMS detector is built to search for the Higgs boson in a wide range of long-lived final state particles, which makes it suitable for the search and study of a variety of heavy particles (expected or not). The CMS detector is built from sub-detectors arranged in cylindrical layers around the beam-pipe, as illustrated in Figure 3.5. From inside out these are: the pixel tracker (Pixel), the silicon strip tracker, the electromagnetic calorimeter (ECAL), the hadronic calorimeter (HCAL), and the muon stations. The solenoidal magnet that serves as the namesake of CMS produces a magnetic field of 3.8 T within the cylinder of the solenoid to assist in reconstructing charged particle tracks, whereas the iron yoke enhances the return magnetic field to achieve a magnetic field of 2 T outside the confines of the solenoid.

A charged particle deposits charge in layers of the inner tracker as it passes through them, and these charge deposits can be connected to form tracks representing the path of the particle (uncharged particles leave behind no charge deposits). The calorimeters serve to absorb and measure the energy of certain kinds of particles, and the muon stations provide additional track measurements at high radii to assist in the reconstruction of muon tracks. Thus, each subdetector layer serves to detect different kinds of final state particle: electrons are found as tracks matched to an energy deposit in the ECAL, photons are found as energy deposits in ECAL without corresponding tracks, charged hadrons ($\pi^{\pm}$, protons) are found as tracks matched up to deposits in the HCAL, uncharged hadrons (π^0, neutrons) are found as energy deposits in HCAL not associated to a track, and muons are found as tracks in the tracker matched to deposits in the muon stations (only muons are penetrating enough to

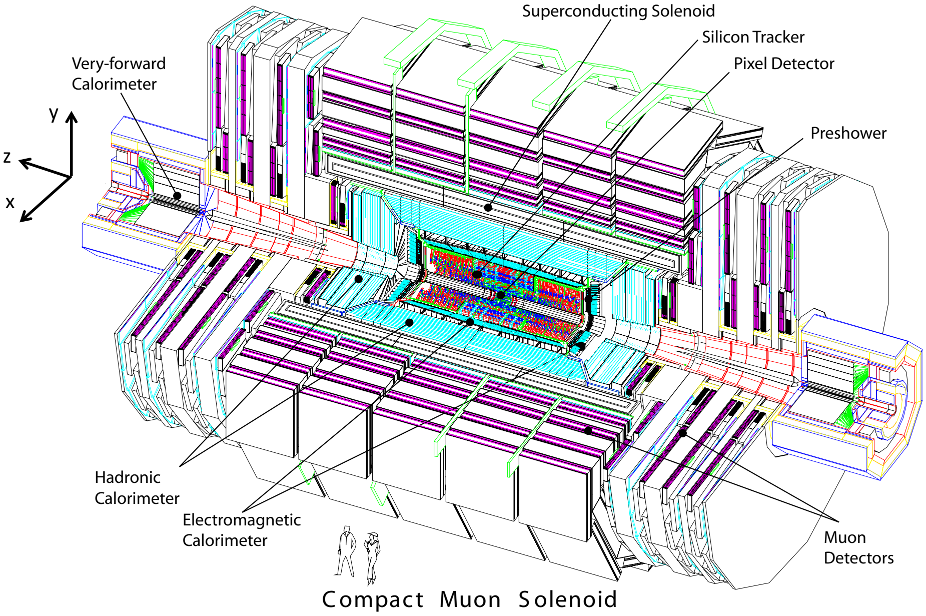

Figure 3.5: A cut-away view of the CMS detector showing the sub-detector systems. The coordinate system is defined to have its origin at the center of the detector, the x-axis pointing to the center of the LHC, the y-axis pointing up from the ground (perpendicular to the LHC plane), and the z-axis aligned with the counterclockwise beam direction.

reach the outer layers of CMS). This process is illustrated in Figure 3.6. Because CMS cannot distinguish different kinds of hadrons from one another, all tracks through HCAL not identified as muons are considered to be pions. The following sections describe the different detector parts and sub-detector systems of CMS: Section 3.2.2 describes the silicon tracker, Section 3.2.3 describes the electromagnetic calorimeter, Section 3.2.4 describes the hadronic calorimeter, and Section 3.2.5 describes the muon stations. Finally, Section 3.3 describes the CMS trigger system and Section 3.4 describes the computing framework for charged particle track reconstruction and muon identification.

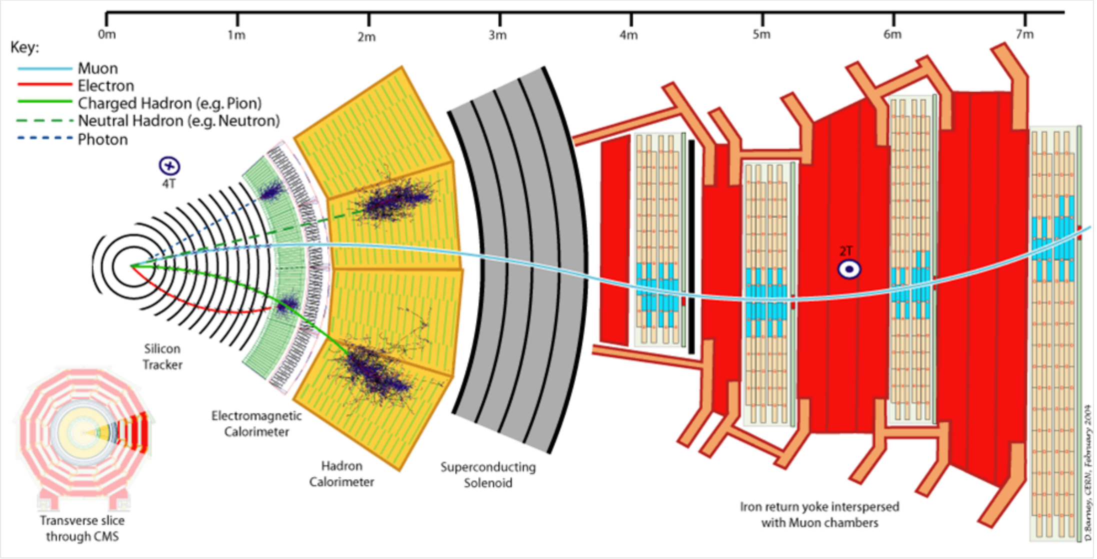

Figure 3.6: A transverse slice of the CMS detector illustrating the manner in which different subdetector layers of CMS serve to identify particles.

3.2.1 Momentum Measurement of Charged Particles

A particle of charge q and velocity $\vec{v}$ subjected to a uniform magnetic field $\vec{B}$ experiences a Lorentz force $\vec{F}$. The Lorentz force is always perpendicular to both the velocity of the particle and the magnetic field that created it. In general, when a charged particle moves in a static magnetic field, it will follow a helical path in which the axis of the helix is parallel to the magnetic field and the speed of the particle will remain constant. Describing CMS in a Cartesian coordinate system, the origin is defined at the center of the detector, the x-axis pointing to the center of the LHC, the y-axis pointing up from the ground (perpendicular to the LHC plane), and the z-axis aligned with the counterclockwise beam direction. Describing CMS in a cylindrical coordinate system, the azimuthal angle φ is defined such that φ is measured up from the cartesian x-axis, ρ is the radial distance from the beam, and θ is measured from the Cartesian z-axis. The helical trajectory can be reconstructed from measured positions along the particle path of length s as:

$$\begin{aligned}
x(s) &= x_0 + \frac{1}{r_0}\left[\cos\left(\phi_0 + \frac{Hs}{r_0}\cos\lambda\right) - \cos\phi_0\right] \\
y(s) &= y_0 + \frac{1}{r_0}\left[\sin\left(\phi_0 + \frac{Hs}{r_0}\cos\lambda\right) - \sin\phi_0\right] \\
z(s) &= z_0 + s\sin\lambda
\end{aligned} \tag{3.5}$$

where (x_0, y_0, z_0) is the starting point at length $s = 0$, r_0 is the radius, λ is the polar (dip) angle, $H = \pm 1$ is the rotation of the projected helix in the transverse plane (the product of the sign of the particle's charge with the direction of the magnetic field along z), and ϕ_0 is the azimuthal angle of the starting point with respect to the helix axis.

In the transverse plane (x,y), the particle follows a circular path with radius r_0 given by Equation 3.1. For high momentum particles, only a slight curvature is observed. A particle of transverse momentum p_{T} passing through a region of length L within a magnetic field B deviates from a straight line by s, the sagitta of the track (see Figure 3.7 for the definition).

The sagitta s determines the momentum of the track, p_{T},

$$s = r - h = \frac{L^2}{8r} \tag{3.6}$$

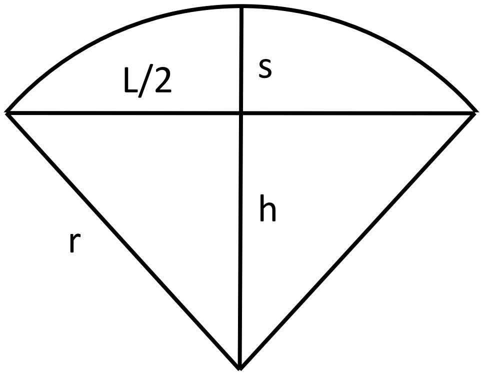

Figure 3.7: Definition of the sagitta s for a particle of transverse momentum p_{T} passing through a region of length L with magnetic field B.

Replacing r with Equation 3.1 yields:

$$p_{\mathrm{T}} = \frac{qL^2B}{8s}. \tag{3.7}$$

The magnitude of the total momentum is given as

$$p_{\mathrm{tot}} = p_{\mathrm{T}}\sqrt{1+\tan^2\lambda}. \tag{3.8}$$

The direction of the momentum is evaluated along the track (see Equation 3.6). The uncertainty of the momentum measurement is related to the error of the measured sagitta $\sigma(s)$ as follows

$$\frac{\sigma(p_{\mathrm{T}})}{p_{\mathrm{T}}} = \frac{8}{qBL^2}p_{\mathrm{T}} \cdot \sigma(s). \tag{3.9}$$

This is directly proportional to the sagitta error and to the transverse momentum p_{T} itself, but inversely proportional to the magnetic field strength and the square of the distance L^2. Hence, the measurement closest to the interaction point is most important to the track, and this is the measurement provided by the silicon pixel detector. The uncertainty also depends on the number of hits in the silicon layers

(N) and their position resolution $(\sigma_{r\varphi})$:

$$\sigma(s) = \sqrt{\frac{720}{N+4}}\frac{\sigma_{r\varphi}}{8}, \tag{3.10}$$

The $\sigma_{r\varphi}$ component always has a contribution from the intrinsic position resolution of the detector and from multiple scattering. The intrinsic resolution depends on the production and collection of secondary charges and the readout electronics used to measure them. Multiple scattering is caused by Coulomb scattering of the particle as it passes through the detector material, essentially bouncing the particle around and lowering its momenta. Multiple scattering depends on the distance the particle travels through the material (l) and the radiation length of the material ($X_0 = 9.4$ cm for silicon). The uncertainty of the momentum measurement due to these two effects can be parameterized as

$$\frac{\sigma(p_\mathrm{T})}{p_\mathrm{T}} \propto a \cdot p_\mathrm{T} \oplus b \cdot \sqrt{\frac{l}{X_0}} \tag{3.11}$$

where a and b are constant terms. Figure 3.8 shows the resolution of muons with p_T of 1, 10, and 100 GeV/c as a function of the pseudorapidity (η).

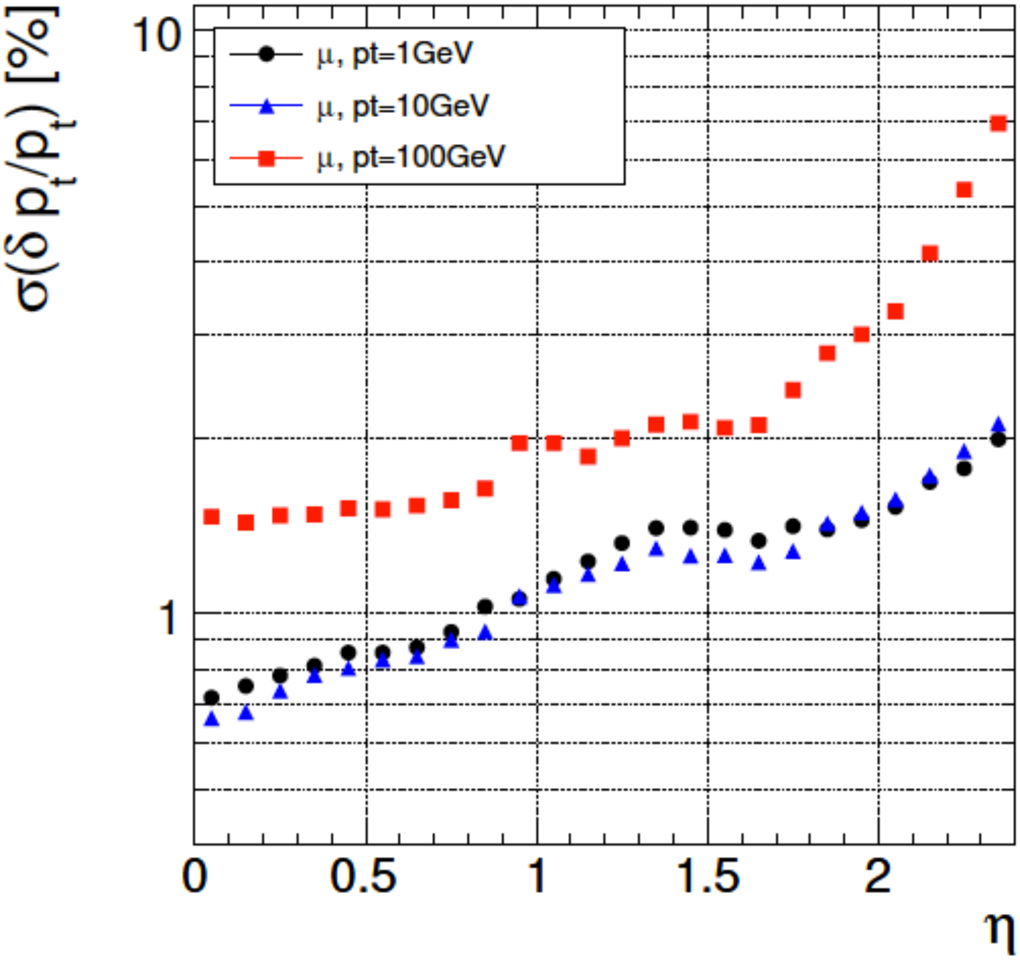

Figure 3.8: Relative transverse momentum resolution for muons with transverse momenta of 1, 10, and 100 GeV/c as a function of the pseudorapidity.

3.2.2 The Silicon Tracker

An average of $1,000$ particles would hit the innermost layers of the tracker at the design luminosity of 10^{34} cm^{-2}s^{-1} during each LHC bunch crossing. In addition, low-p_{T} tracks curl around the beampipe due to the strong magnetic field, leading to repeated charged particle interactions at low radii. The particle flux in the innermost pixel layer is dominated by pions created either by the main proton collisions or by stray protons interacting with beampipe or detector material. The detector is exposed to fluences of up to 10^{14} n_{eq}/cm^2 per year (where 1 n_{eq} is a MeV neutron equivalent particle), resulting in a sufficiently hostile radiation environment at low radii to damage sensitive detector material in a short period of time. To provide high precision charged particle tracking under these conditions, the detector must:

- maintain function in a hostile radiation environment,
- reconstruct charged particle tracks close to the collision region to precisely determine the momentum of charged particles and the position of secondary vertices from long-lived decays,
- provide many hits per track, with a single-hit position resulotion ~ 20 μm for tracks normal to a detector panel.

The material for such a detector was chosen to be silicon doped with donor impurity atoms. Such silicon is a semi-conducting material with good intrinsic energy resolution. An energy deposit of 3.6 eV is needed to create an electron-hole pair in the detector material. Reverse biasing a $p-n$ junction of the silicon sensor creates an electric field strong enough to push liberated charge towards charge readouts. The low ionization threshold leads to a large amount of liberated charge per deposit. Unlike with gas detectors, the collected signal is only a function of the detector thickness (there is no multiplication of primary charge). To minimize the multiple scattering, the detector thickness is as small as possible, with a practical limit set by the signal-to-noise ratio. An average of 3×10^4 electron-hole pairs are created with a silicon thickness of 300 μm (0.3% of a radiation length), a very detectable signal with low noise electronics. Silicon-based sensors have a position resolution on the order of tens of microns, a short signal collection time, and can be operated in strong magnetic fields. The smallest radius at which a traditional silicon micro-strip detector can function in the CMS radiation environment is limited by its occupancy and radiation damage. Reducing the size of the sensor elements reduces the hit rate per element and leads to a higher position resolution. This is why silicon pixels were chosen for the innermost part of the CMS tracking detector. The number of pixel channels needed (and hence the cost of the detector) is proportional to the area (r^2), while the particle flux is inversely proportional to this value (relaxing the necessary single-hit resolution). Hence, for radii greater than 15 cm, silicon strip detectors were chosen.

The pixel detector consists of three cylindrical layers (the barrel pixel detector, or BPix) and two layers of endcap discs on either end of the cylinders (the forward pixel detector, or FPix). The pixel detector is essential for forming seed tracks for track reconstruction and for the reconstruction of secondary vertices from long-lived decays. The 53 cm long BPix layers are located at mean radii of 4.4, 7.3, and 10.2 cm. The FPix disks have a radius of 6 and 15 cmand are placed on at $z = \pm 34.5$ and $z = \pm 46.5$ cm. BPix (FPix) contains 48 million (18 million) pixels, resulting in an occupancy of 10^{-4} hits per pixel per bunch crossing at full luminosity. Figure 3.9 shows this geometric arrangement and coverage as a function of pseudorapidity. The pixel detector covers the pseudorapidity range $-2.5 < \eta < 2.5$, matching the range covered by the other layers of the tracker. In the high-η region, hits in the innermost barrel layer are matched to hits in the two disks.

The dimensions of a pixel are 150 μm $\times$ 100 μm. The side 150 μm long is in the direction of Lorentz drift in the barrel, taking advantage of the Lorentz force to smear charge over multiple pixels. The side 100 μm long is parallel to the magnetic field. The pixel system has an analog pulse readout. The position resolution for each pixel due to charge sharing between neighboring pixels helps to separate signal

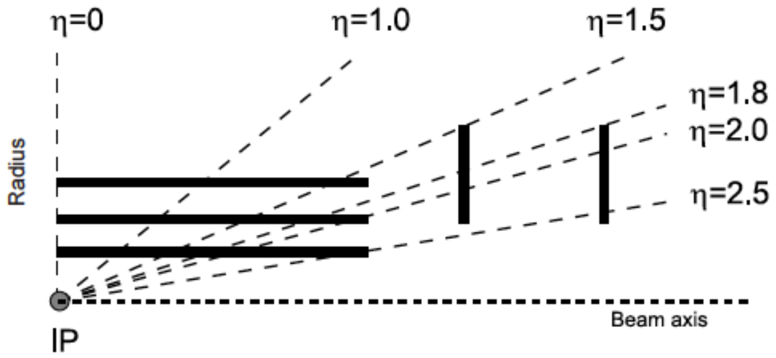

Figure 3.9: Geometrical layout of the pixel detector and hit coverage as function of pseudorapidity. IP refers to the interaction point.

hits from noise and identifies large charge deposits from overlapping tracks. Charge interpolation of the analog pulse results in a spatial resolution of $10-12$ μm for tracks normal to the sensor. The endcap detectors are tilted 20° in a turbine geometry to cause charge sharing given the lack of Lorentz drift in sensors where the electric field is parallel to the magnetic field.

Radiation damage causes charge to become trapped in the silicon material, reducing the effective depth of silicon sensitive to the passage of a charged particle and decreasing the amount of charge sharing (and hence, position resolution). Increasing bias voltage can compensate for the initial effects of radiation damage, but careful monitoring of detector performance and the radiation environment is important and the innermost pixel layers will need to be replaced after a few years. A more detailed description of the pixel detector can be found in Chapter 4.

The CMS silicon strip detector is the next part of the inner tracker. This system is 5.8 m long and 2.5 m in diameter. The total active silicon region of 75 million readout channels covers a surface area of 200 m^2, making the CMS tracker the largest silicon detector ever built. The silicon strip tracker is divided into the tracker inner barrel (TIB) and tracker inner disks (TID) that cover $20 < r < 55$ cm, and the tracker outer barrel (TOB) and tracker outer endcaps (TEC) that cover $55 < r < 120$ cm. Figure 3.10 demonstrates the coverage afforded by the silicon strip tracker.

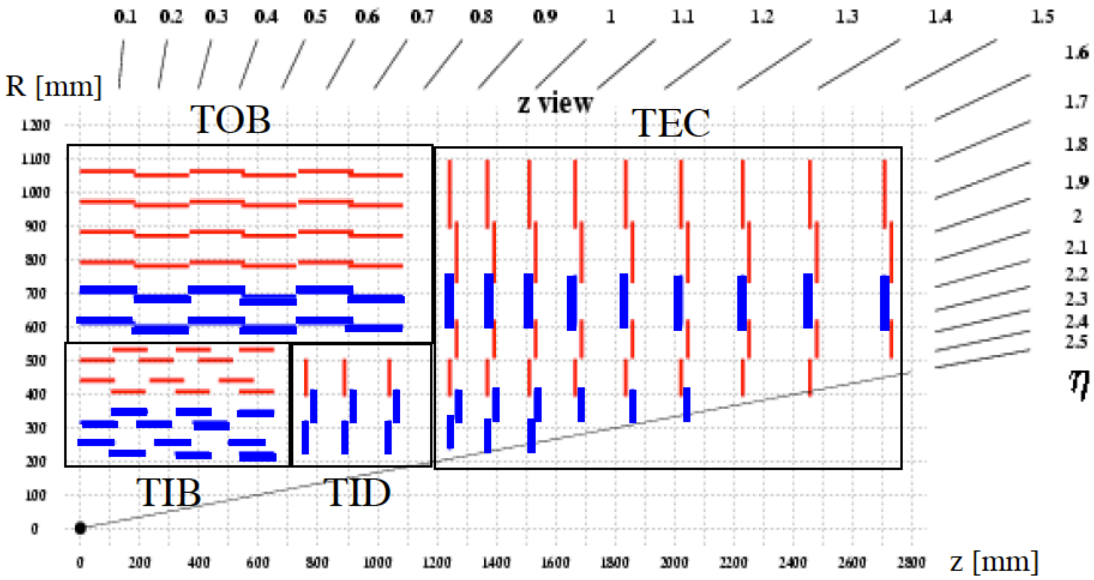

Figure 3.10: Coverage provided by a quarter of the CMS silicon strip tracker.

The tracker coverage ends at $|\eta| < 2.5$, and as Figure 3.10 demonstrates, a track of $|\eta| < 2.4$ crosses at least nine strip detector layers, from a radius of 20 cm to 1.2 m. The width, length, and pitch (distance between strips) are chosen to maintain consistent resolution and occupancy, with an increasing pitch at higher radii. The TIB consists of four barrel layers of strips, each strip 10 cm in length with a minimum pitch of 80 μm. The TID consists of three endcap layers, each strip 10 cm in length and with a pitch of 100 μm. This ensures an occupancy of up to $2-3\%$ per bunch crossing for single strip, with a single point resolution in $r - \varphi$ of 23 to 35 μm (depending on the $r - \varphi$ pitch). The TOB consists of six barrel strip layers, each strip 25 cm in length and with a pitch of 180 μm. The TEC consists of nine endcap strip layers, each strip 25 cm in length and with a pitch of 184 μm. This ensures an occupancy of up to 1% per bunch crossing for a single strip in the outer region, with a single point resolution in $r - \varphi$ of 35 to 53 μm (depending on the $r - \varphi$ pitch). The magnetic field deflects very low momentum particles back towards low radii, so the outer region ($r > 55$ cm) experiences a rapid decrease in charged particle rates (hence, the increased strip length and pitch). However, electronic noise grows linearly with strip length and decreases with thickness, so the strip thickness must be increased to 500 μm in the outer regions to keep the signal to noise ratio above ten. The resulting higher depletion voltage is offset by a higher initial resistivity, so the initial depletion voltage of the thick and thin sensors are within the same range. Some layers are equipped with stereo-modules, shown in blue in Figure 3.10. In that case, two modules are mounted back-to-back at a stereo angle of 100 mrad to provide a measurement in (r, z) as well as in (r, φ). They provide single point resolutions of 230 μm and 530 μm in z in the inner and outer barrel, respectively. The silicon strip detector material budget, in units of radiation length, increases as function of pseudorapidity from 0.4 X_0 at $\eta \approx 0$ to about 1.8 at $\eta \approx 1.4$. Beyond this value, it decreases to about 1 X_0 as it approaches $\eta \approx 2.5$. The relative transverse momentum resolution for the full silicon tracker (pixel and strip technologies) was shown earlier in Figure 3.8.

3.2.3 The Electromagnetic Calorimeter

A brief discussion of the electromagnetic calorimeter (ECAL) is given here for completeness even though this analysis does not make direct use of ECAL information. For neutral Higgs bosons with masses below ~ 140 GeV, the decay into two photons offers a clean channel for discovery. Identification of the Higgs via a diphoton resonance requires measurement of the total energy and direction of decay photons with energies above 100 GeV. The CMS ECAL uses an array of lead tungstate crystals ($PbWO_4$) to measure the energy deposition of electrons and photons in that regime. Lead tungstate is an ideal material for this purpose because of its stability in high-radiation environments, its relatively fast scintillation response time (80% of the light released within 25 ns), and its small radiation length (0.89 cm). The total amount of secondary light collected from the crystals is proportional to the amount of energy lost by the incident particle. If the particle is completely stopped, the total energy of the particle is deposited and converted into light. The $61,200$ crystals in the ECAL barrel region (EB) and the $7,324$ crystals in each of the two ECAL endcaps (EE) provide a hermetic, homogeneous coverage up to $|\eta| < 3$. Groups of 25 crystals are arranged in geometric structures called towers. In front of each ECAL Endcap is a preshower detector (ES) covering $1.65 < |\eta| < 2.6$ and made from silicon strip detectors in order to reject the $\pi^0 \rightarrow \gamma\gamma$ decays. The measurement of charged particle tracks for muons and hadrons is not degraded by the calorimeter material budget. The energy loss for muons traversing the crystal is negligible because of its small radiation length. The problem does not exist for hadrons because the energy is determined from the track reconstructed in the silicon tracker (positioned before the calorimeters).

3.2.4 The Hadronic Calorimeter

A brief discussion of the hadronic calorimeter (HCAL) is also given for completeness even though this analysis does not make direct use of HCAL information. The

HCAL is a second calorimeter system located just after the ECAL CMS Collaboration (1997a). It is used to

- measure the energy of hadronic collision products in CMS, whether as groups of hadrons traveling in the same direction (jets) or individual hadrons and muons,
- generate energy segments for High Level Trigger (HLT) decisions, and
- measure the instantaneous luminosity of the LHC.

The HCAL is required to have as many interaction lengths of material as possible because hadronic showers generally have a much longer interaction length than electromagnetic showers. Each HCAL tower is placed behind a corresponding ECAL tower (except in the endcap region) to produce a long structure capable of measuring the total energy of hadrons in a well defined (η,φ) region with minimal leakage. Figure 3.11 illustrates a section of CMS with the HCAL components labelled.

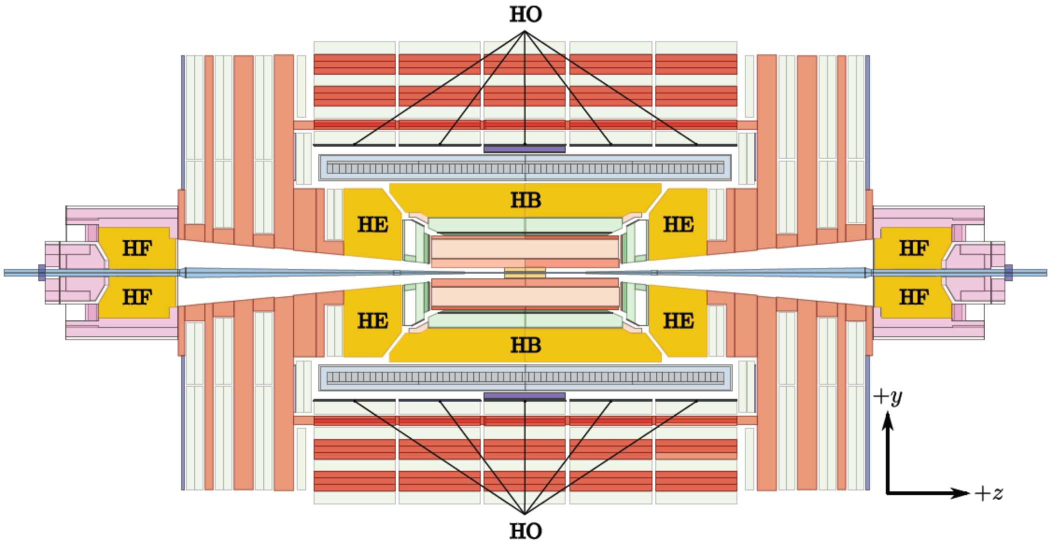

Figure 3.11: A view of the CMS detector in y-z projection with the components of the HCAL labeled.

HCAL is composed of four sub detectors: the HCAL Barrel (HB) covering $|\eta| < 1.4$, the HCAL Endcaps (HE) covering $1.3 < |\eta| < 3$, the HCAL Outer (HO) covering $|\eta| < 1.3$, and the HCAL Forward (HF) covering $2.8 < |\eta| < 5.2$. The HB and HE are located in between the ECAL and the magnet. The HO sits between the magnet and the muon stations and serves to catch the tails hadronic showers. The HF is essentially an iron cylinder that acts to absorber hadrons, with a total depth of 165 cm (≈ 10 interaction lengths).

The barrel, the endcap, the outer hadronic calorimeters are all sampling calorimeters consisting of plastic scintillators sandwiched between brass absorbers. The scintillators sample the showers of charged particles produced by the nuclear interactions of hadrons with the nuclei of the absorber. Transverse to the beamline, the absorber of the barrel calorimeter is 5.82 interaction lengths deep. The effective depth increases with psuedorapidity, resulting in 10.6 interaction lengths at the edge of the barrel. The endcaps are 10 interaction lengths deep (taking into account ECAL as well as HCAL shielding). The HO is positioned outside of the magnet and adds another 19.5 cm of iron shielding. Thus the total depth of the calorimeter system is at least of 11.8 interaction lengths. Being very close to the beam-pipe, each HF detector is exposed to roughly 380 GeV of energy per pp collision due to soft scattering, compared to only 100 GeV of energy deposited in the rest of the detector. This high particle flux environment must use a different type of detection system. The forward calorimeter is also a sampling calorimeter, but uses scintillating quartz fibers oriented in the direction of developing electromagnetic and hadronic showers (as opposed to the scintillating plates perpendicular to showers in the central hadronic calorimeters). Quartz fibers act as the active medium and signal is generated when charged particles generate Cherenkov light, making the HF mostly sensitive to the EM component of showers.

3.2.5 The Muon System

The muon system has to: distinguish muons from hadrons, perform a fast muon multiplicity count, and add to the muon track measurement. Identifying muons and precisely measuring their momenta is of prime importance to CMS. The CMS muon system provides important information to:

- measure the decays of J/ψ mesons into muons (the subject of this analysis),
- search for the Higgs Boson decay into ZZ or ZZ^* (which in turn decay into a four muon end state),
- search for new gauge bosons (such as $Z' \to \mu^+\mu^-$ with $p_{\mathrm{T}}^{\mu} > 1$ TeV),
- determine lepton and photon isolation criteria, and
- identify jets from *b*-quark decays (exploiting the b $\to$ μ decay essential to Higgs studies, top studies, and SUSY searches).

Muons are unique among the products of high-energy collisions because they have a long lifetime (2.2 μs in their rest frame), a large rest mass (105.7 MeV/c^2) and do not interact via the strong force. The long lifetime enables the muons to reach the outer layers of the detector and beyond. Due to their greater mass, muons are not deflected by electromagnetic fields so much as electrons and do not emit as much bremsstrahlung radiation (the primary mechanism of energy loss for decelerating charged particles). This allows a muon to penetrate much deeper into detector material than an electron with the same energy. Relativistic muons are called Minimum Ionizing Particles (MIPs) because the amount of energy lost by the muon per unit of distance traveled in a medium is close to the minimum. The energy loss rate of a muon only increases logarithmically between momenta of $p = 1$ and $p = 100$ GeV/c, so that all muons in this momentum range are effectively minimum-ionizing. Finally, because the muons do not experience the strong nuclear force, they do not lose energy due to inelastic nuclear collisions in the dense calorimeter material as hadrons do. Thus muons reach the outside of the solenoid magnet with relatively little energy loss. The physics goals are

- muon identification: at least 16 radiation lengths of material are needed to ensure absorption of other charged particles before (in the HCAL and ECAL) and inside the muon system (in the iron yoke);
- muon trigger: the combination of muon chambers and fast muon counters provide unambiguous collision event identification and trigger on single and multi-muon events with well defined p_{T} thresholds from a few GeV/c to 100 GeV/c for $\eta \leq 2.1$;
- transverse momentum resolution: from $8-15\%$ $\delta p_{\mathrm{T}}/p_{\mathrm{T}}$ (at 10 GeV/c) to $20-40\%$ (at 1 TeV) for muons reconstructed with the muon system, and from $1-2\%$ (at 10 GeV/c) to $6-17\%$ (at 1 TeV) after combining the reconstructed muon in the muons system with a track from the CMS tracker;
- charge assignment: evaluated from the direction of charged track curvature in the magnetic field (correct to 99% confidence up to the kinematic limit of 7 TeV);
- capability of withstanding the high radiation and interaction background expected at the LHC.

Due to the shape of the solenoid magnet, the muon system has a cylindrical barrel section and two planar endcap regions. The muon system uses three types of gaseous particle detectors:

- **Drift Tubes** (DT) in the barrel region ($|\eta| < 1.2$) where the magnetic field is confined to the iron yoke, the muon rate is low, and the background rates are small;

- **Cathode Strip Chambers** (CSC) in the the endcap discs ($0.9 < |\eta| < 2.4$) in order to deal with the strong, non-uniform magnetic field and the high charged particle rates in the forward region;
- **Resistive Plate Chambers** (RPC) over the barrel as well as endcaps (used to supplement the other two technologies).

Figure 3.12 shows the muon system, which provides geometric coverage up to $|\eta| < 2.4$ CMS Collaboration (1997b); Chatrchyan et al. (2008). DTs and CSCs provide excellent position resolution and RPCs provide excellent time resolution, so the technologies are used together to utilize each other's strengths while offsetting weaknesses.

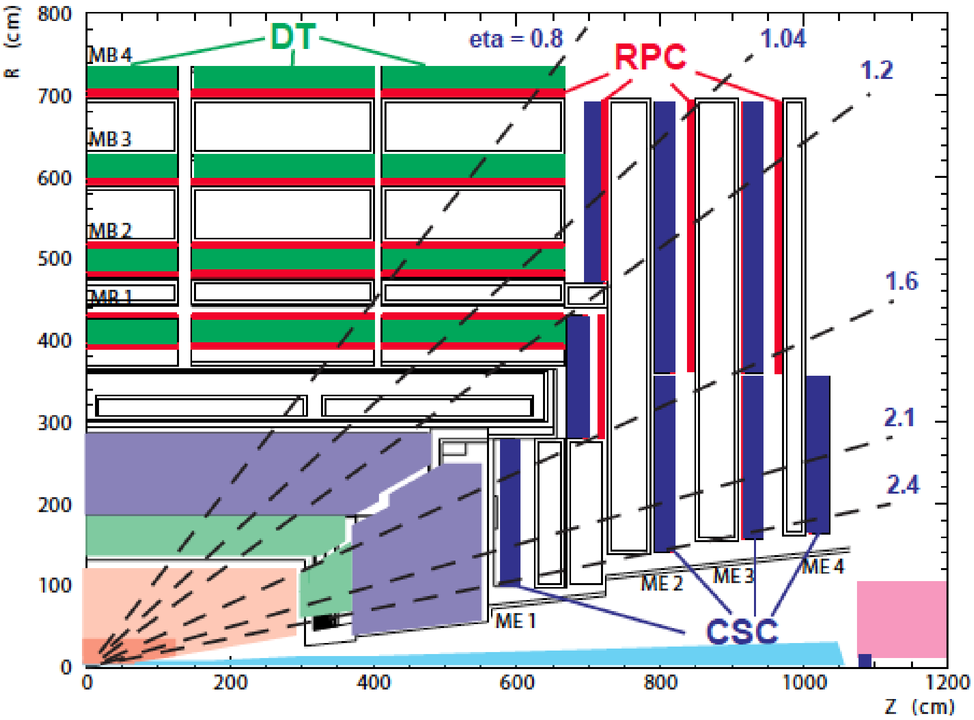

Figure 3.12: A quarter section of the muon system.

A Drift Tube (DT) is a gas-filled cylindrical cathode tube with an anode wire running through the center held at slightly above atmospheric pressure. A charged particle passing through the tube will ionize atoms in the gas, causing liberated electrons to move toward the anode wire and cause secondary ionizations that produce an electric current. Time measurements of the current pulses with respect to the the known electron drift time allows reconstruction of the position of the charged particle as it passed through the DT. This reconstruction requires precise control over the pressure, temperature, current flow, and gas purity in the DT. The DT system is made of three Super-Layers (SL), each consisting of four layers of drift tubes. The two outer SLs ($r-\varphi$ type) measure the track coordinates in the transverse plane while the inner SL (z type) measures the track coordinate in the beam direction. Multiple chambers are clustered in stations, for a total of four embedded in the gaps within the flux return yoke. Each of the first three stations (MB1, MB2, MB3) contain eight chambers (in two groups of four) that serve to measure the $r-\varphi$ coordinate of the muon track, as well as four chambers that serve to measure the z-position of the hit. The fourth station (MB4) does not contain any measurements of z-position. The two measurements are combined to build a three-dimensional segment in the chamber. Figure 3.12 shows the configuration of the four stations in the barrel. DT chambers in the four different MB stations are staggered so that a high-p_{T} muon produced near a sector boundary crosses at least 3 of the 4 stations. DT chambers are also installed in an alternating fashion with RPCs (one or two at a time, depending on station). In this way, a high-p_{T} muon crosses up to six RPC and four DT sections, producing up to 44 measured points in the DT system from which a muon track candidate can be built. The resolution on the z position varies between 100 μm (for a track reconstructed from eight points) to 250 μm (for a track reconstructed from a single point). The resolution in the $r-\varphi$ direction is about 0.5 mrad.

A Cathode Strip Chamber (CSC) is a trapezoidal multi-wire chamber that consists of six gas gaps. Each gap has a plane of radial cathode strips and a plane of anode wires that run almost perpendicular to the cathode strips. The gas ionization and subsequent electron avalanche caused by a charged particle traversing each plane of a CSC liberates charge that gets collected on the anode wire and image charge on a group of cathode strips. In this way, the CSC measures a 3D hit position in each of the six layers. Closely spaced wires make the CSC a fast detector (response time of ~ 4.5 ns), but with a relatively coarse position resolution. The position resolution is improved by using the charge-weighted center of the charge distribution induced on the cathode strips, resulting in a spatial resolution of $\sim 200\ \mu$m and an angular resolution of ~ 10 mrad. CSCs are used at very large radii because they can operate in large and non-uniform magnetic fields without significant deterioration in their performance (gas mixture composition, temperature, and pressure do not directly affect CSC precision).

A Resistive Plate Cathodes (RPC) is a gaseous parallel-plate detector that provides excellent time resolution (typically around 3 ns) but poor position resolution (around 1 cm), and so are used in conjunction with DTs and CSCs. RPCs consist of two resistive plates made of bakelite that are kept parallel to one another by insulating spacers that define the size of the gas gap. A uniform electric field of a few kV/mm causes an avalanche multiplication of the ionization electrons across the gap. The readout is performed by one set of copper strips placed in the middle of the gaps and requires a high signal amplification in the front-end electronics to compensate for the low gas amplification (Avalanche-mode operation). The rate at which an RPC can register hits primarily depends on its electrode resistivity, while the speed at which it can register a hit primarily depends on the gap width. Due to their excellent time resolution, RPCs guarantee a precise bunch crossing.

These three detectors operate within the Level-1 (hardware based) trigger system described in detail in Section 3.3. The muon detection system is capable of identifying single and multi-muon events to high resolution in a p_{T} range of a few GeV/c to TeV/c. The relative muon momentum resolution as a function of p_{T} is illustrated in Figure 3.13. The silicon tracker provides the best momentum resolution for muons with a p_{T} below 200 GeV/c, where the resolution in the muon chambers is dominated by multiple scattering. Multiple scattering and energy losses become negligible at higher momenta, so the momentum resolution benefits from high radii measurements made in the muon stations.

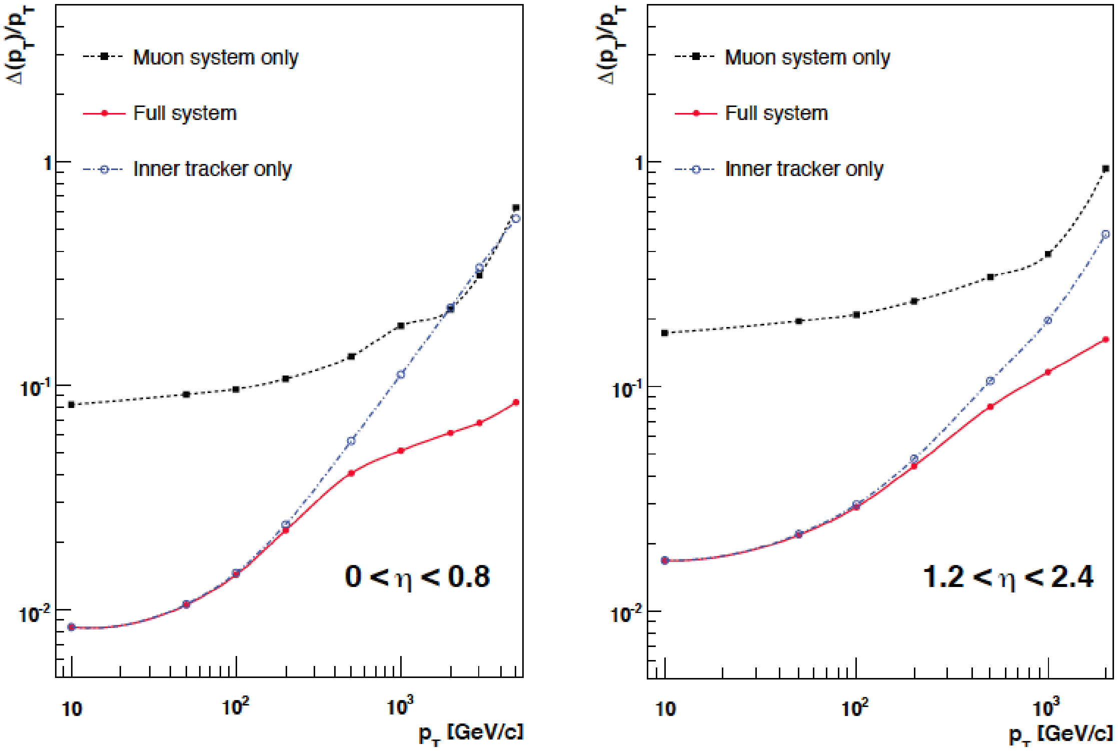

Figure 3.13: Relative muon p_{T} resolution as a function of p_{T} for measurements with the muon system only, with the inner tracking only, and with both systems in the barrel (left) and forward (right) regions.

3.3 CMS Event Selection and Reconstruction

At full intensity, the LHC will generate collision events at a rate of 40 MHz, too great a rate to be recorded with present computing technologies. The data must therefore immediately be pared down to contain only events most likely to contain interesting physics processes. To do this, CMS employs a two-tiered trigger system: a hardware-based *Level-1* trigger (L1) CMS Collaboration (2006b) and a software-based *High-Level Trigger* (HLT) CMS Collaboration (2002). The L1 trigger is designed to make decisions within 3.2 μs after a collision occurs, and reduces the event rate by a factor of 10^{-3}. The HLT reduces the rate by another factor of 10^{-2} to 100 Hz before the events are shipped off to long term storage.

3.3.1 Level-1 Trigger

The CMS L1 trigger CMS Collaboration (2006b) is entirely hardware-based and uses only the calorimeters and muon systems because information from the tracker is too complex to be analyzed on the short timescale required for the L1. The architecture of the L1 system is shown in Figure 3.14. The L1 trigger is divided into local, regional, and global components. At the local level, the individual sub-detectors use pattern-matching algorithms to find high-energy deposits in the calorimeters or high-momentum charged tracks in the muon system. The highest-quality primitives (defined as muon track segments or electron/photon energy towers) are assigned on the basis of parameters such as energy deposited and reconstructed momentum from the local levels and sent from each sub-system to one of two regional-level triggers: the Regional Calorimeter Trigger (RCT) and the DT and CSC Muon system Track Finders. The RCT is an algorithm that combines information from HCAL and ECAL to find electron/photon candidates. The algorithm processes the input of each region where energy deposits are found and creates two sets of information: the sum total energy, and the highest-energy pair electron candidates. Here, an electron candidate is defined as an energy deposit in a single crystal. The eight highest energy pairs and

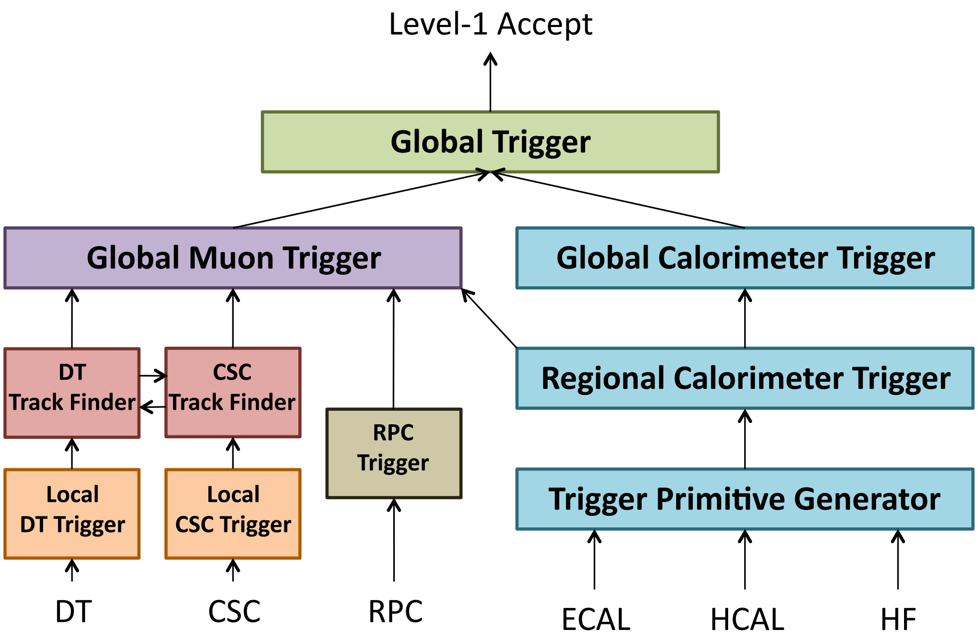

Figure 3.14: The L1 trigger system architecture.

regional sums are collected in an intermediate buffer area and then forwarded to the Global Calorimeter Trigger (GCT). The second regional trigger uses two of the muon sub-systems (the DTs and the CSCs) to convert detection information (chamber ID, strip patterns, etc.) into r- and φ-coordinates. The reconstruction of a muon track starts with each muon station generating a momentum hypothesis for the muon that traversed it based on the pattern of deposits. If the hypothesis matches a template for high momentum muons originating from the collision region, the dedicated muon trigger hardware forwards the information to Track Finder (TF) algorithms that combine the information from several stations to make an approximate measurement of the muon p_{T}. The four highest p_{T} muons from the CSC and DT Track Finders are forwarded to the Global Muon Trigger (GMT). The RPCs instead forward all of their data to a regional trigger system that detects muons based on hits in adjacent RPC chambers. The RPC Pattern Comparator Trigger (PaCT) then uses data from the HCAL Outer (HO) detector to identify muons and measure their transverse momenta in the barrel portion of CMS. The PaCT forwards the four highest p_{T} muon candidates (in the barrel and endcaps) to the GMT. The CMS Global Trigger (GT) compiles all the information from the GCT and GMT to make a trigger decision. A table of selection criteria is encoded in Field-Programmable Gate Arrays (FPGA) that allow fast decision-making and fast changes in the algorithms to adapt to changing run conditions. If the collision event is considered interesting by the GT, it sends a Level-1 Accept (L1A) message to each subdetector to begin Data Acquisition (DAQ). The total time between a collision and a L1A decision is less than 3.2 μs.

3.3.2 High Level Trigger

The CMS High Level Trigger uses data from all subdetectors to reconstruct the collision event and to make a decision CMS Collaboration (2002). The event reconstruction software is similar to that used in offline reconstruction (but simplified to speed up the process). CMS employs 720 computers with eight processing cores apiece to do the HLT reconstruction, resulting in a mean decision time of 50 ms per event. The HLT only reconstructs areas of the detector where the L1 algorithms identified interesting physics objects. Tracks are reconstructed using the silicon pixel and strip tracker to achieve better track resolution (the only stage in the trigger to use tracker information). The HLT is configured to select events according to a list of algorithms (trigger menu) corresponding to one or more physics objects, each reconstructed from one or more subsystems. Triggers are split into single object type (one or two leptons, one or two photons, one or multiple jets, etc) and cross-type triggers (muon plus electron or photon or jet, etc). For studies of charmonium ($c\bar{c}$) and bottomomium ($b\bar{b}$) states, such as J/ψ(nS) and Υ(nS), and B hadrons decaying into a J/ψ (with subsequently J/$\psi \to \mu^+\mu^-$), a dedicated set of unbiased triggers with loose muon selection criteria are used. For these triggers (named as `DoubleMu_X`), a total bandwidth of $\sim$ 40 Hz was assigned from the total $\sim$ 100 Hz available. The dominant fraction was allocated for fundamental perturbative QCD measurements involving the b and the c quarks (prompt and non-prompt J/ψ, Υ, and B mesons production cross sections). Once an event is selected by one of the HLT algorithms, it is shipped out of Point 5 for storage and further reconstruction.

3.3.3 Dataset Creation and Offline Reconstruction

Events selected by the HLT are transferred to several tiers of computing centers and the events reconstructed again in more detail using newer alignment and calibration information. Because this reconstruction does not need to occur at the event rate of data acquisition, it is known as offline reconstruction. The first tier of computing center to accept raw data from the HLT is known as Tier 0 (T0), located at CERN. T0 repacks the raw data into primary datasets based on trigger information (for example, events passing a muon-based trigger are packed into a muon primary dataset), archives the raw datasets, and sends a copy of each raw dataset to seven major computing sites around the world (Tier 1, or T1 locations). Each dataset is then reconstructed at T0 and the reconstucted datasets copied to the T1 locations. This process of offline calibration, alignment, and reconstruction is summarized in Figure 3.15.

The first iteration of offline calibration, alignment, and reconstruction typically occurs within 48 hours of data acquisition, and so is known as the Prompt Reconstruction. Subsequent iterations of reconstruction on the original raw data are performed every few months of data-taking at the T1 locations, as alignment and calibration parameters are refined with increased statistics and improvements are made to the reconstruction software.

3.4 CMS Analysis Software

To aid in processing the enormous amount of data that the CMS detector produces, a framework of dedicated analysis software called CMSSoftware (CMSSW) was developed by the CMS community CMS Collaboration (2005). It is designed around the concept of an event (representing a collision), which can contain everything from

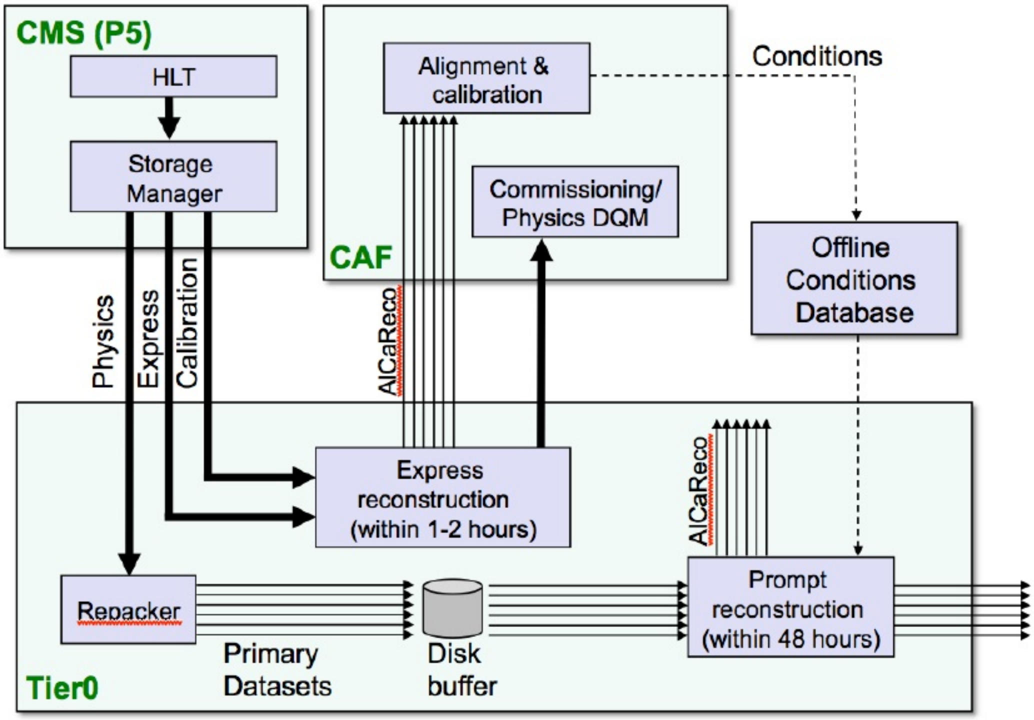

Figure 3.15: The prompt calibration, alignment, and reconstruction loop.

raw detector information (RAW) to reconstructed physics objects representing the particles produced in that collision. This information is stored as C++ objects using the ROOT analysis framework Verkerke and Kirkby (2003). CMSSW employs different categories of algorithms to perform reconstruction: producer modules build upon event information to insert new objects into the event representing the next layer of reconstruction (up to the final physics objects), filter modules remove objects to ensure quality or remove duplications, and analysis modules use the products of reconstruction to create summary information about the event. The analysis software also allows access to information about the condition and configuration of the detector held in database objects.

3.4.1 Event Reconstruction

The goal of reconstruction is to create representations of physics objects such as electrons, muons, photons, and jets from raw digitized detector data. Once all physics objects in an event have been reconstructed (RECO objects), they can be stored away from the raw detector data to use less physical storage space and network transfer time. Many different producer modules are used to generate the different RECO candidate objects, and sometimes multiple producers are used to reconstruct the same candidate objects in different ways. This section will focus on those reconstruction algorithms that pertain to this analysis: charged tracks and muons.

Track Reconstruction

The track reconstruction can be divided into five logical steps:

- Hit reconstruction
- Seed generation
- Pattern recognition (track building)
- Ambiguity resolution (track cleaning)
- Final track fit (track smoothing)

The digitized raw data from the sub-detectors are combined with detector geometry and alignment information from a conditions database to build three-dimensional Reconstructed Hits (RecHits). At least three RecHits reconstructed from charge deposits in the Pixel subdetector or two Pixel RecHits compatible with the beamspot are required to initiate a track search (seed generation). Seeding provides the initial description of the five parameters of the helical track and is based on the combinatorial Kalman filter method Fruhwirth (1987a). A Kalman filter fits a parameterized function to data by iterating over the measurements and taking advantage of known correlations between measurements and measurement resolutions. A track is built from each seed and propagated to the next detector layer (taking into account possible multiple scattering and energy losses). A separate track candidate is formed for each hit that falls within a certain χ-square range. The procedure is repeated layer by layer until the outermost layer is reached and all possible unique tracks are formed (or until a stopping condition is applied) [†]. This creates a large number of tracks, many of which share the same hits. If the fraction of shared hits between two trajectories is too large, the ambiguity is resolved by keeping only the highest-quality track. To avoid biases during track building, all valid tracks are refit with a Kalman filter and a smoother algorithm is applied, which moves in from the outermost layer toward the beamline searching for hit positions to improve the quality of the track.

Muon Reconstruction

In collision data, muons are tracks reconstructed using hits reconstructed in both the inner tracker and the muon stations. Tracks are first independently built using only hits in the tracker or muon stations. Then, the tracker-only tracks are propagated outward to the muon stations and a test is performed to see if they match within a search window of any muon-only tracks. If so, a new track is created by combining the tracker-only and muon-only tracks and refitting to the full set of hits. Only tracks passing an additional χ-square test are considered, and ECAL information is also used to verify the compatibility of a track with the muon hypothesis (minimum ionizing particle).

[†] e.g. to limit the CPU time in the HLT, where only a partial track reconstruction with less than $5-6$ hits is necessary to achieve the required accuracy.

Chapter 4

The CMS Pixel Detector

4.1 Introduction

Tracking must reach as close as possible to the primary collision point in order to identify tracks from a displaced origin (resulting from long-lived decays). The high particle flux near the collision region makes it important to have not only good position resolution, but also high granularity (ability to distinguish closely-spaced particle tracks). The CMS silicon pixel tracker fulfills these requirements. Over the full acceptance of the CMS detector, the silicon pixel tracker provides two or more hits per charged particle track. These hits serve as the seeds for track-building and will be the most important measurements when fitting tracks to a common vertex. The position resolution of such a vertex depends on three attributes of the pixel subdetector:

- single hit resolution,
- distance of the layers from the interaction region,
- the material budget.

The distance of the pixel layers is constrained by the size of the beampipe and the particle flux (which decreases by the square of the radius). The resolution is inherently limited by multiple scattering in the beampipe and detector. The multiple scattering angle depends directly on the distance traversed in the medium (in radiation lengths), and is inversely proportional to the momentum and velocity of the incident particle Beringer et al. (2012). This translates into a position uncertainty on vertexing that depends on the thickness of the pixel sensors. To achieve the desired vertex position resolution, the width of the sensor is chosen to correspond to 0.3% radiation lengths in silicon. In this chapter, the principles of the pixel detector are described in Section 4.2. The pixel readout scheme is introduced in Section 4.3 and the software architecture for reconstruction is introduced in Section 3.3.3, with emphasis on the reconstruction software used by the pixel detector.

4.2 Pixel Sensors

When a charged particle passes through silicon, it interacts with the material via the Coulomb force. The two most important processes taking place are elastic scattering on nuclei (in which the particle essentially bounces off of atomic nuclei in the material), and EM interactions (in which the particle loses energy due to inelastic collisions with atomic electrons in the material). Excited electrons transit to the conduction band of an atom and they behave as free carriers, leaving behind holes (missing electrons) in the valence band. A Minimum Ionizing Particle (MIP) normal to the sensor plane releases an ionization charge of approximately 23 ke^- in a silicon sensor with a thickness of 285 μm. The charge primarily moves through diffusion and drift in semiconductors, and will move randomly in all directions in the absence of an electric field (eventually losing all momentum to lattice collision). Pixel sensors apply a voltage of 100 V to achieve a field strength of $E \lesssim 300$ kV/m. An electrode on one side of the silicon substrate collects the electrons to read out the signal. The typical mobility of electrons in silicon is $\mu_e = 0.14$ m^2/(Vs), quickly resulting in a drift-velocity of $v_D = \mu_e E = 2.1 \times 10^6$ m/s that remains constant over the time of the drift. Hence, the collection time across the sensor thickness (d) is $t_D = d/v_D \approx 0.1$ ns. The total drift force (F) acting on a charged particle in the presence of constant electric (E) and magnetic (B) fields is given by the Lorentz force (see Figure 4.1)

$$\vec{F} = q \cdot \left(\vec{E} + \vec{v} \times \vec{B}\right)$$

where $\vec{v}$ is the velocity of the charge carriers. If the magnetic field is perpendicular to the electric field, the carriers drift at a Lorentz angle θ_L given by:

$$\tan \theta_L = \mu_e \cdot |\vec{B}|.$$

For a 4 Tesla magnetic field the Lorentz angle is $\theta_L \approx 30°$, causing the electrons to

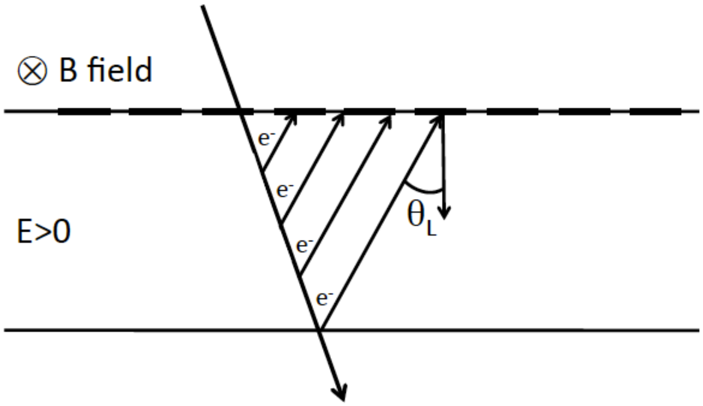

Figure 4.1: Graphic representation of the Lorentz angle (θ_L) for a charged particle traversing the silicon substrate.

smear over more collection electrodes. The electron mobility is a factor higher than for holes, leading to a larger Lorentz angle.

The sensor of the CMS silicon pixel detector is a p- and n-type semiconductor joined together ($p-n$ junction). p-type semiconductors are obtained by adding atoms (through doping) with a deficit in valence electrons (acceptors) to the silicon. n-type semiconductors are obtained by adding atoms that provide extra valence electrons (donors) to the host material. Once the contact is established between p- and n-type semiconductors, the excess electrons on the n-side diffuse into the p-side while the excess holes in the p-side diffuse into the n-side. This process creates an excess of positive charge on the n-side and negative charge on the p-side. While the holes (electrons) are diffusing, some of the acceptor (donor) ions ($N_{A(D)}$) near the p-side (n-side) are left uncompensated since the number of acceptors (donors) is fixed in the semiconductors. The result is an electric field, which causes a zone around the junction to becomes free of mobile charges (depletion zone). The electric field counteracts the diffusion and prevents further movement from the charge carriers. Diffusion and drift currents are in opposite directions, which means the net electron and hole currents will be zero on the borders of the depleted region (equilibrium condition). The width of an intrinsic depletion region is on the order of 10 μm, which corresponds to $V_{bi} \approx 0.5$ V. A larger depletion zone is created by applying a reverse bias voltage V_{bias}, with $-V_{bias}$ across the p-side junction and $+V_{bias}$ across the n-side, shown in Figure 4.2. With a field strength of less than 100 V, the depletion zone is effectively extended over the full sensor and liberated charge is quickly collected by this strong external field. The width of the depletion zone is inversely proportional to the density of acceptor N_A and donor N_D. Hence, the depletion zone can be extended into one side of the semiconductor if the concentration of doping atoms of the other side of the junction is much larger.

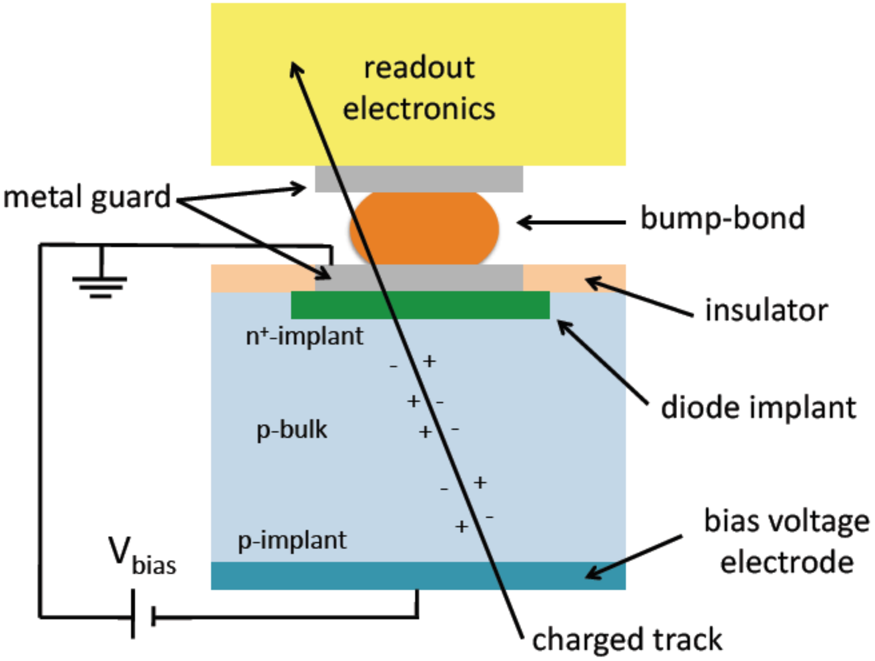

Figure 4.2: Diagram of a single silicon pixel. It is defined electrically by the readout electrode on top that is bump bonded to a readout channel on the readout chip (ROC). The backside is a continuous electrode.

The BPix layers and FPix disks are composed of modules, each of which consist of segmented rectangular regions (pixels) of size 100 μm × 150 μm connected to highly integrated readout chips (ROC) using a bump-bonding technique (see Figure 4.2). The pixel is designed as a high concentration n-implant (n^+) emmersed in a highly resistive n-substrate that serves as the active volume. The $p-n$ junction is created by a high concentration p-implant at the back in contact with the n-substrate, shown in Figure 4.3. The bulk material will invert its type from n to p when irradiated,

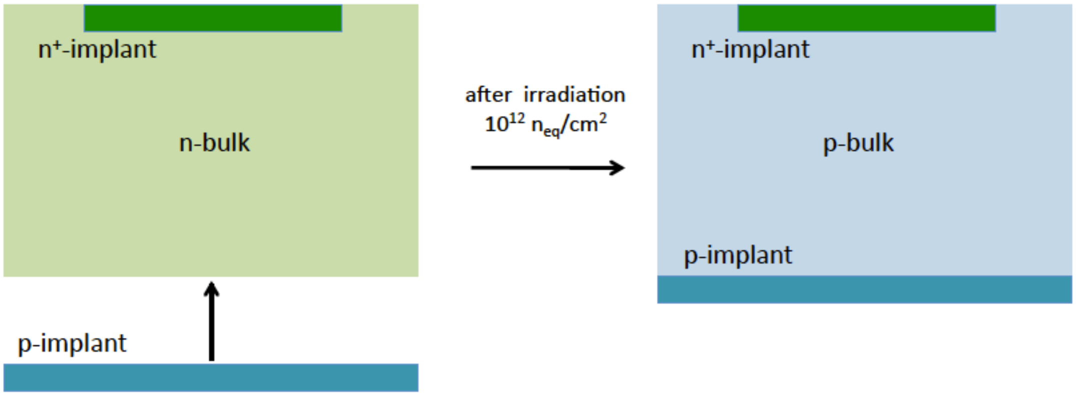

Figure 4.3: Configuration of $p-n$ junction before (left) and after (right) the irradiation that causes the type-inversion of the active volume.

expected to occur primarily from pions produced by LHC collisions. A dose of order 10^{12} n_{eq}cm^{-2} was delivered within days during the startup of the LHC. Exposure to the high particle flux has the adverse effect that it

- changes the effective carrier concentration requiring higher bias voltages to achieve depletion over the full detector depth,
- increases the leakage current,
- reduces the charge collection as free charge carriers get trapped hence near displaced atoms.

Furthermore, noise is introduced by the random release of trapped charges. The pixel detector initially operates at a voltage of 150 V, but higher bias voltages (up to 600 V) will be needed to compensate for irradiation damage in the sensor after irradiation with a fluence of about 10^{15} n_{eq} cm^{-2}. After three years operating at the LHC design conditions, the innermost layer of the detector will need to be replaced. The small gap between the collecting electrodes (i.e. the n-implant) ensures a homogeneous drift field. The $p - n$ junction is placed on the back of the sensor and surrounded by a multi-guard ring structure that allows all sensor edges to be kept to a ground potential (see Figure 4.2). To perform an on-wafer measurement of the current-voltage characteristics, each pixel is connected to a bias grid through a high resistance punch through connection (bias dot).

The pixel detector is arranged in three cylindrical (barrel) layers (BPix) of pixel detector modules at radii of 4.4, 7.3 and 10.2 cm, illustrated in green in Figure 4.4 CMS Collaboration (2006a). The forward pixel (FPix) detector consists of two disks placed at either end of the barrel at $z = \pm 34.5$ and $z = \pm 46.5$ cm. The disks have inner and outer radii of approximately 6 cm and 15 cm and are subdivided in 24 trapezoidal blades, shown in orange in Figure 4.4.

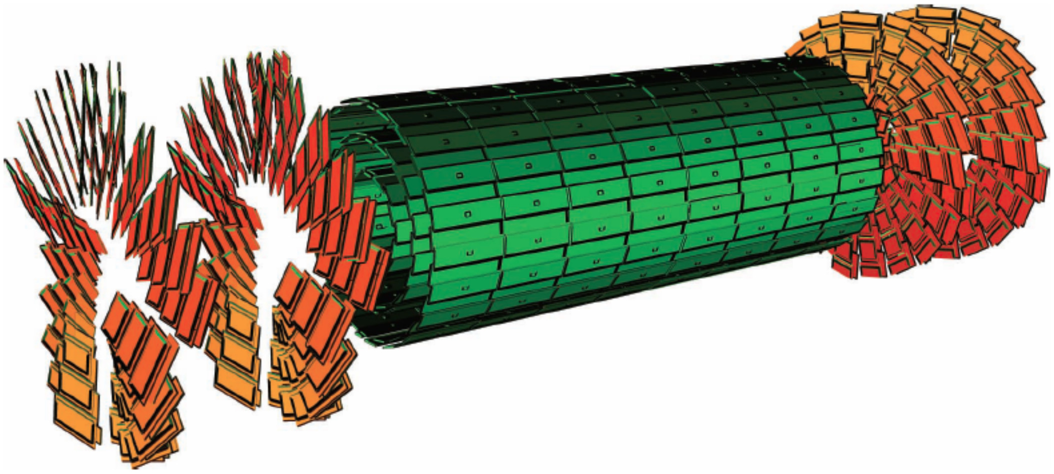

Figure 4.4: Sketch of the CMS forward and barrel pixel detectors. The barrel pixel detector consists of three central layers whereas the forward pixel detector consists of two disks on each side.

When a particle traverses a sensor, the liberated electrons drift towards the collection electrode (with the amount of charge collected proportional to the path length of the particle within the silicon substrate). The hit position is estimated by weighting the location of the pixel readouts by the amount of charge they collected.

$$\bar{x} = \frac{\sum_i Q_i x_i}{Q} \tag{4.1}$$

where $Q = \sum_i Q_i$ is the total charge collected. Interpolating positions between pixels based on the amount of collected charge requires pulse-height information. Without charge sharing, the position cannot be resolved within the pixel boundaries to better than a pixel length/$\sqrt{12}$, which corresponds to a resolution of about 40 μm. With charge sharing, an intrinsic hit resolutions of $10 - 15$ μmcan be obtained.

The shift due to the Lorentz force has to be taken into account when reconstructing the hit position. Hence, the Lorentz angle needs to be known to a high precision. The grazing angle method of measuring the Lorentz angle is shown in Figure 4.5. This method uses well reconstructed tracks that have a shallow impact angle with respect to the direction of the magnetic field. Ionizing particles traversing the detector generate signals which can be seen on several successive pixels. Each pixel in the chain collects charge from a given segment of the particle's trajectory. The signal ends at the pixel row under which the particle leaves the detector. Due to the Lorentz force, the drifting charge carriers reach the surface with a displacement proportional to their drift-length. Therefore, it is expected that pixels near the end of the chain will loose some charge to the adjacent pixel rows. According to Figure 4.5, one can measure the Lorentz-angle as

$$\tan\theta_L = \frac{\tan\beta}{\tan\alpha} \tag{4.2}$$

where α is the grazing angle and β is the angle of the charge deflection measured at the surface.

For the characterization of the barrel pixel detector with the magnetic field of 3.8 T, the Lorentz angle has been measured in collision data (at center-of-mass energy around 3.5 GeV) to be $21.72° \pm 0.01°$ Ivova (2011).

Other corrections to charge smearing effects can be evaluated with the η distribution. It is measured to find the position distribution of the electrons collected by the electrodes. If the charge Q is deposited in two adjacent pixels, left (L) and

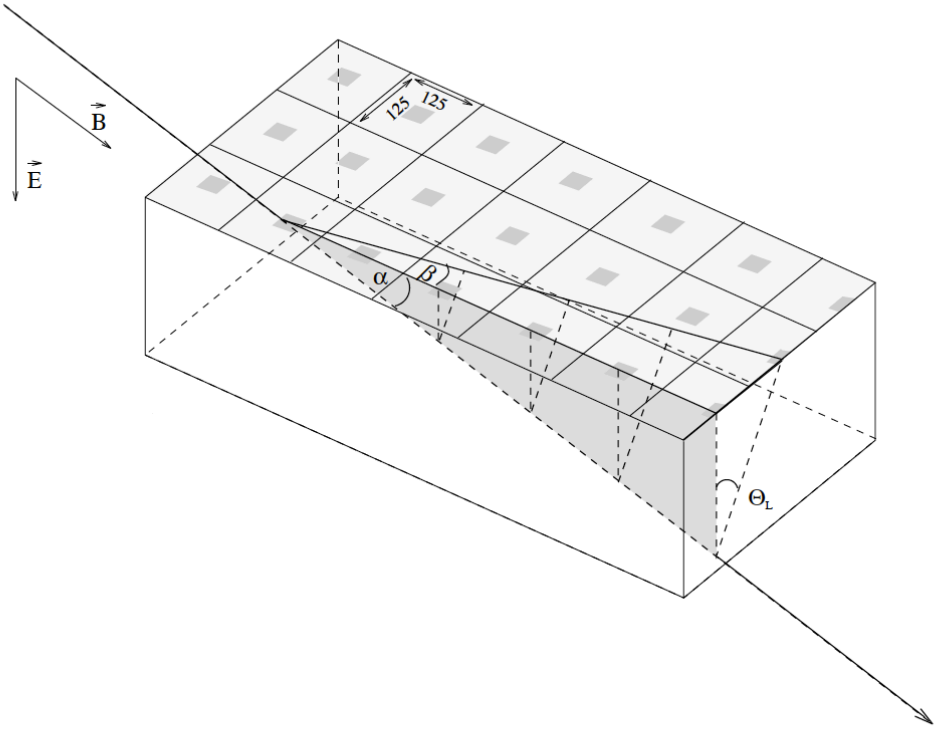

Figure 4.5: Measurement of the Lorentz angle θ_L with the grazing angle method.

right (R), the fraction of charge deposited in the right pixel is

$$\eta = \frac{Q(R)}{Q(R) + Q(L)}. \tag{4.3}$$

For a given passing particle the average impact point between the two pixels and its resolution can be obtained by integrating the η distribution up to the measured η. This method is limited by statistical fluctuations, mainly due to due to electronic noise and electrons from secondary ionization.

The shape of pixels results in comparable resolution in both directions. In the direction parallel to the magnetic field (z-direction), there is no Lorentz drift but sufficiently inclined tracks are detected in more than one pixel, allowing interpolation in both directions. At high rapidity, where tracks hit the barrel detector at low angles, the small z-size is a disadvantage because increasing cluster size in the z-direction is only beneficial for the z-resolution until it exceeds two pixels. Higher multiplicities also overload the readout system. Therefore, the choice was made to complement the barrel detector with pixel disks in forward and backward directions. Sufficient charge sharing in the FPix is achieved with a tilt angle of 20° between the blades. The Lorentz angle measured in the forward pixel detector is smaller and found to be $4.40° \pm 0.55°$ Ivova (2011) in the 2010 cosmic rays data.

4.3 Pixel Readout System

The pixel barrel (BPix) layers and the forward/backward (FPix) disks are composed of modules (and some half-modules) that contain the readout electronics and the power supply. A module consists of:

- 16 ReadOut Chip (ROC): performs the signal readout,
- Token Bit Manager (TBM): controls the read-out of several ROCs,

- High Density Interconnect (HDI): a circuit board that distributes the control and power signals to the readout chips and the TBM,

- Base stripes: used for mechanical stability and as a contact between the module and the cooling structure,

- Kapton cable: transfers the control and analog signals,

- Power cable: supplies the analog, digital, and bias voltages.

Figure 4.6 illustrates the components of a module as they are assembled. The modules are attached to cooling frames, with the cooling tubes being an integral part of the mechanical structure. The analog charge signal is read and digitized at faster using a Flash ADC. A schematic view of the pixel readout is shown in Figure 4.7. The

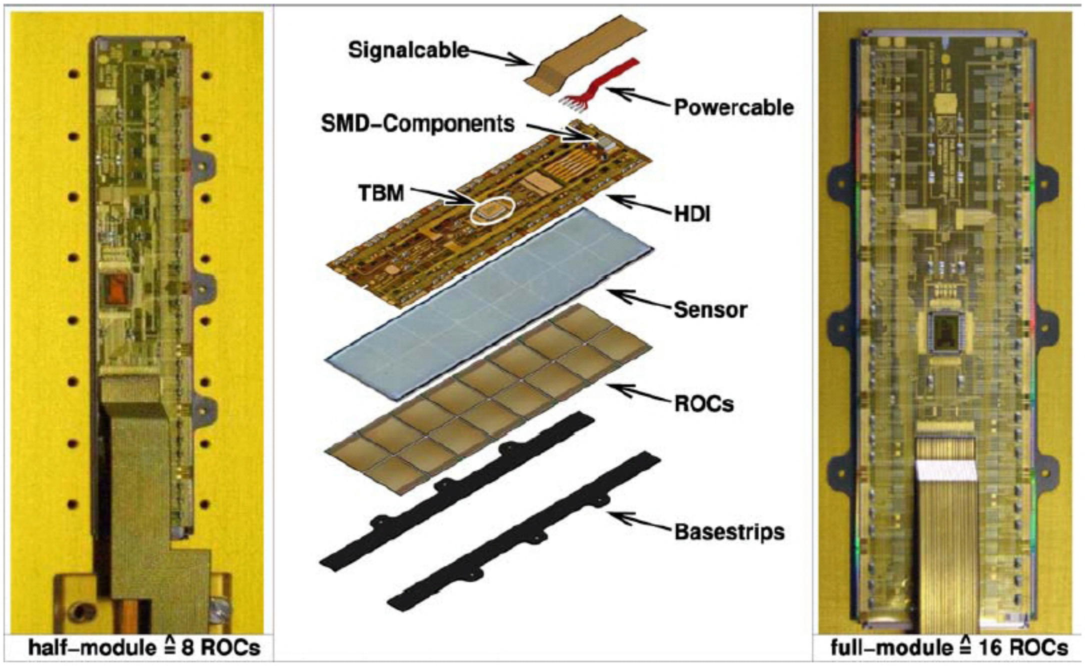

Figure 4.6: View of a half-module (left) and a full module (right) fully assembled. Middle: expanded view of a barrel pixel module showing the two silicon nitride base strips, the 16 readout chips (ROCs), the pixel silicon sensors, the High Density Interconnect (HDI) with the Token Bit Manager (TBM), and the power and Kapton cables.

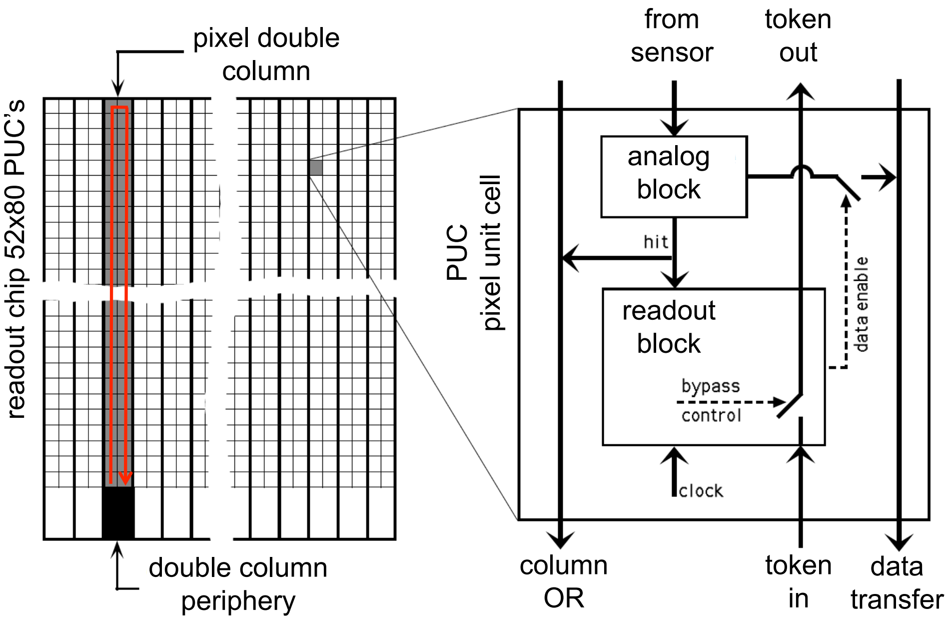

Figure 4.7: A schematic view of the readout chip.

ionization charge of a CMS pixel sensor is read out by a corresponding channelled Pixel Unit Cell (PUC) connected electrically via a bump bond. In a ROC, there are 26 double columns and 80 rows in the active area to read out 4160 pixels in total. The ROC chip periphery contains:

- a serial programming interface to configure the pixels,
- digital-to-analog converters (DAC) to adjust offsets, gains, thresholds, supply voltages, timings, etc.,
- control registers to set the trigger latency and readout speed,
- an analog event generator that collects the pixel hit information from the double columns and generates the output data stream,
- a fast double-column hit counter that can be used in principle by the CMS first level trigger or for self-triggering when no external trigger is available.

A sketch of the PUC is shown in Figure 4.7 on the right. It can be divided into an analog part and the digital logic. The charge produced by an ionizing particle traversing the silicon sensor is collected at the electrode formed by the n-implant and by a capacitor. The charge signal enters a two stage charge sensitive pre-amplifier/shaper system. Alternatively, calibration signals can be injected through an injection capacitor connected directly to the amplifier input node. This feature is used to study pixel efficiencies. A global threshold can be programmed for the whole chip using the DAC. Pixel cells within one double column are connected to its periphery with a set of local bus lines, one of them being the column-OR, which combines all pixel cells in a double column into a global OR. Only signals that are above the threshold are allowed to trigger the digital part of the circuit. Once the comparator is above threshold (zero suppression) the shaper output signal is stored in a memory buffer and the double column periphery is notified immediately through a fast hard-wired column OR. The pixel becomes insensitive and waits for a column readout token (the pixel dead-time is short, ≥ 50 ns). The double column periphery controls the transfer of hit information from the pixels to the storage buffers (column drain mechanism) and performs trigger verification. The column drain cycle takes place within each double-column and runs at 40 MHz. The readout starts with the pixel closest to the periphery on the left side of a double-column and returns along the right side (see Figure 4.7). The time information is stored (within 25 ns) in the time-stamp buffer and the address and the analog signal of each pixel hit is transferred to the column data buffer located in the column periphery. For the average of two pixel hits per double column, about six clock cycles (at 40 MHz) are required to complete the readout. This data has to be stored for 3.2 μswhile waiting for the Level-1 (L1) trigger decision. For every clock, the bunch crossing counter (BC) stored in the time stamp buffer is compared with the search counter (WBC). If both agree the time stamp is considered for trigger confirmation. The data confirmed by the L1 are saved for the second stage of the readout while the unconfirmed data are erased. In the second readout stage, the triggered data are transmitted to the CMS data acquisition (DAQ). They are drained from each double-column and sent via optical links to the readout electronics (Front End Driver modules - FEDs) in a room 100 m away from the detector. Groups of 8 or 16 ROCs are connected to one readout link. In order to synchronize the data transmission a token-bit manager chip (TBM) is used. The TBM controls the readout of the ROCs by initiating a token pass for each incoming L1 trigger. On each token pass, it writes a header and a trailer word to the data stream to facilitate event recognition. The header contains an 8-bit event number and the trailer contains 8-bits of error status. The token bit is passed on from ROC to ROC and finally back to the TBM where the trailer is generated and the TBM becomes ready to accept another trigger. A schematic view of the pixel readout and the token bit mechanism is shown in Figure 4.8.

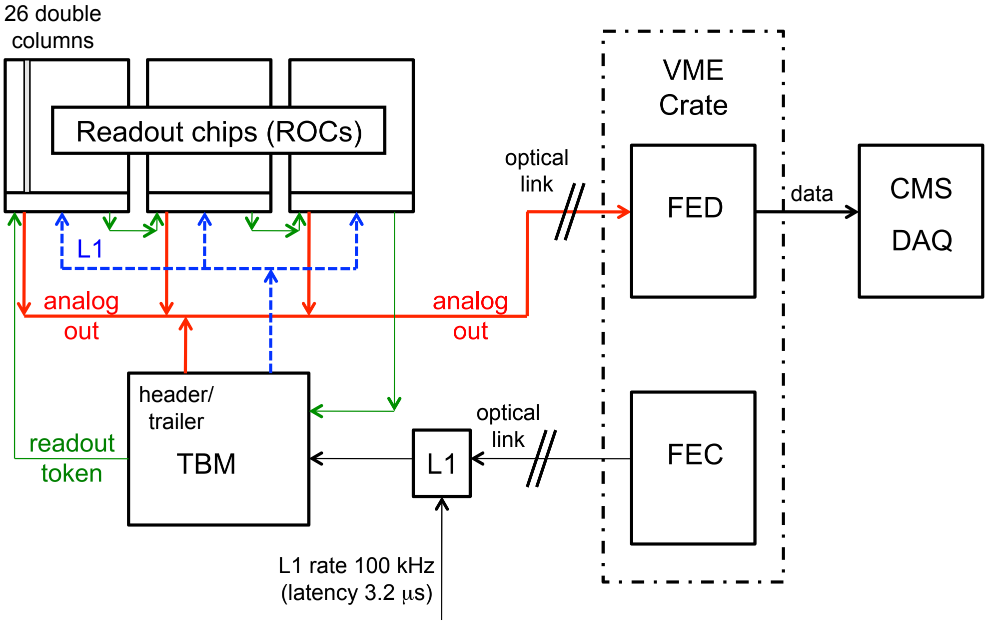

Figure 4.8: A schematic view of the pixel readout system.

The data stream containing all hit information belonging to a single trigger is sent out by the TBM through the module Kapton cable. A single Kapton cable brings the analog signals of one readout group to the printed circuit board on which the Analog Optical Hybrids (AOHs) are placed. The electric analog signals are amplified in an Analog Level Translator (ALT) chip and converted into 40 MHz analog optical signals in the AOHs. Each AOH is equipped with 6 lasers which drive the signal through optical fibers to the Front End Driver modules (FEDs) in the counting room 100 m away from the detector. A FED has 36 optical inputs each equipped with an optical receiver and an ADC. The FED receives the analog data, digitizes the signals, and decodes the pixel address information. It builds event fragments by passing digitized pixel information through three tiers of First In, First Out (FIFO) buffers as follows:

- the decoded output of each optical fiber is assembled into 32-bit data words containing single pixel ADC and address information to be stored in FIFO I buffers. If there is a problem in signal decoding or emptying of a FIFO I into FIFO II, an error word is generated and stored in an Error FIFO.
- words from four or five FIFO I buffers and the Error FIFO responsible for them are joined two at a time into 64-bit words and stored in FIFO II buffers.
- four FIFO II buffers empty into a single FIFO III buffer.

The FED then encapsulates the data stream with 64-bit header and trailer words containing additional information (FED number, bunch crossing, L1 id, and size of event fragment) before transmitting it to the central DAQ system. A single FED can buffer up to 100 events.

The Front-End Control modules (FECs), also located in the counting room, send the clock, trigger and all other control and reset signals to the detector. The ROC chip programming (e.g. setting of the pixel thresholds) is also performed with the FECs. The FED and FEC modules which service the same segment of the detector are located in the same VME crate. This way both can communicate with the same crate controller CPU, allowing for efficient system monitoring and fast resets in case of error conditions. Each crate controller communicates with a monitoring workstation where more global data diagnostics is performed. Other standard components of the pixel readout system are:

- Trigger Timing and Control (TTC): sends the L1 accept signal to the FED and FEC, distributes the 40 MHz clock, and manages various synchronization and calibration commands,

- Local Trigger Control (LTC): is used in combination with the TTC manages the local trigger control,

- Tracker FEC (TKFEC): communicates with the Communication and Control Unit (CCU) which performs slow controls of the pixel readout chips, such as configuring them for data acquisition, calibration, or standby mode, setting thresholds etc.

4.3.1 Detector Commissioning

Tests on modules are necessary to verify that all pixels function correctly, each ROC can be programmed properly, and all modules are calibrated satisfactorily. A list of configuration and calibrations have been performed before the 2011 data taking campaign:

- noise measurements: the noise of a pixel is determined by measuring the efficiency of the pixel as a function of the amplitude of the calibration signal. Noisy pixels may flood the ROC with a high rate of fake hits and cause significant dead time and data losses. Therefore, either the threshold of these pixels has to be increased or the pixels have to be removed from the data taking (masked),

- trimming: the aim of the trim calibration is to unify the thresholds of all pixels on a ROC to the lowest possible value. A common threshold (V_{pix}) for all pixels is set in the ROC. To account for pixel to pixel variations, four-bit trim values (v_{trim}) are set in each PUC. The strength of the correction is determined by the trim voltage (V_{trim}), which is set per ROC. It is set with respect to the absolute threshold ($V_{threshold}$) at which the response has to be unified. The relation is approximately:

$$V_{pix} = V_{threshold} + v_{trim} * V_{trim},$$

- pulse height calibration: this calibration is performed by injecting signals with various amplitudes to each pixel via the PUC calibration capacitor and measuring the corresponding pulse heights. For each pixel, the height of the generated pulse is recorded and an extensive offline analysis performed,
- other calibrations: they involve the testing of the module response to the charge injected to the silicon sensor and the calibration of the internal signal of each ROC.

The turn-around time for calibrating all 66M pixels is about one month. The studies yield pixel response efficiencies of 98.8% and 96.4% (overall 98.2%) for BPix and FPix, respectively.

4.4 Offline Reconstruction

Events selected by the trigger undergo reconstruction in two steps: local reconstruction, and global reconstruction. Local reconstruction involves the translation of digitized raw subdetector data into charge or energy deposits with a 3-dimensional position in the CMS coordinate frame. The global reconstruction processes then build physics objects from the products of local reconstruction, as described in Sections 3.4.1 and 3.4.1. Local reconstruction of Pixel data plays a particularly important role in the construction of physics objects in an event because charge deposits reconstructed in the Pixel subdetector serve as the seeds for track-building. This section gives an overview of the Pixel local reconstruction workflow and describes in detail the development and testing of software necessary to perform the first step in the local reconstruction of raw pixel data.

4.4.1 Overview of Pixel Local Reconstruction

The analog output of each pixel is digitized by the FEDs as a 32-bit raw word that contains an Analog-to-Digital Conversion (ADC) charge value along with pixel address (in terms of ROC and link number read out by the FED). The FED also creates 32-bit words to encode information about errors that occur during processing. The FED then joins together pairs of 32-bit words to form 64-bit words and inserts 64-bit header and trailer words at the beginning and end, respectively, of an event's content to demarcate the event and store additional event information. The formatted raw data is then transmitted over the 64-bit serial link (S-link) to DAQ as input to local reconstruction, which proceeds in three steps:

- Raw-to-Digi conversion: 64-bit raw words transmitted by the Pixel FEDs are translated into 32-bit digital pixel measurements on a plaquette.
- Clusterization: single pixel measurements on a plaquette are combined with neighbors to create charge clusters.

- Hit reconstruction: charge cluster information is combined with templates to reconstruct the location on the plaquette hit by a charged particle from the collision region.

The raw-to-digi process takes in the 64-bit event information formatted for the S-link and outputs a C++ container organized by plaquette number, each entry containing the 32-bit digitized readouts of the pixels (digis) in that plaquette. In addition to formatting event content as C++ objects suitable for use in CMSSW, this step of reconstruction removes words that do not contain pixel information (eg, headers, trailers, and error words) and stores information about errors that occured during data acquisition and processing.

The clusterization process takes the output from the previous step to create a collection of entries containing the charge deposit information collected by the corresponding plaquette. First, the clusterizer algorithm uses pixel calibration information to convert the ADC value of a digi into a charge in electrons. Next, neighboring digis with non-zero charge are grouped together as the basis for a cluster. If the total charge of such a group of digis exceeds a pre-defined minimum, a cluster object is made that contains the total amount of charge (in electrons) of the group, the location of the group's charge-weighted center on the plaquette, and the location and charge of the pixels in the cluster.

The hit reconstruction process takes in the collection of charge clusters in Pixel in order to create a collection of positions on the plaquette (and associated position error) where charged particles from the collision region traversed the Pixel sensor. A hit is reconstructed by performing a χ^2-fit of the charge and position measured in the cluster's pixels to templates of charge distributions left by tracks with similar angles on plaquette in simulation. The hit position on plaquette is estimated from the template with the lowest χ^2-fit, and the χ^2 value itself is used to determine the quality of the hit reconstruction and the error associated with the position estimate Swartz et al. (2007). The 2D hit position on plaquette can then be combined with knowledge of the plaquette position in the 3D CMS coordinate frame to reconstruct the 3D position of pixel hits used as input to track-making.

The entire reconstruction sequence is run in reverse during detector simulation. Once points have been identified at which a simulated charged particle track intersects a plaquette, Pixel simulation goes through the following steps:

- Clusterization: the amount and shape of charge deposited in the plaquette is determined based on templates.
- Digitization: the charge collected by individual pixels is estimated and the ADC value is simulated based on calibration information.
- Digi-to-Raw: the digitized pixel readouts are converted into a raw data collection with the same format as the raw data issued by the FEDs.

4.4.2 Pixel RawToDigi Conversion

The Pixel RawToDigi process is the first level of offline reconstruction of Pixel data, translating raw data from the Pixel FEDs into digis (C++ objects formatted for the CMSSW environment). The unpacker first iterates over the raw data indexed to Pixel FEDs (FED numbers 0-39). The translation proceeds by stripping out the 64-bit S-link header words and checking that the FED number encoded in the header word matches the index of the raw data; unpacking for that FED proceeds only if the numbers match. Once the headers are processed, 64-bit words containing digitized pixel readouts are split in half to form two 32-bit words, each representing the original raw words digitized by the FED. The bit designation for these raw words is shown in Table 4.1.

Table 4.1: The bit designation for 32-bit data and error words created by the FED.

Bit #:	31	30	29	28	27	26	25	24	23	22	21	20	19	18	17	16	15	14	13	12	11	10	09	08	07	06	05	04	03	02	01	00
Data word:	Link #						ROC #					DCOL #					Pixel #								ADC Value							
Error word:							Error Code					Additional Error Information																				

Each data word contains the ADC charge reading and unique address of a pixel; the basic job of converting raw words to digis is to translate the hardware-based addressing of the raw words (identified by FED, link, ROC, and DCOL and Pixel address on ROC) into the geometry-based addressing of the digi words (identified by plaquette index, as well as row and column address within the plaquette). Address translation is performed in two steps: determination of the plaquette index, and transformation of the pixel row and column values from ROC-based to plaquette-based coordinates. The plaquette index is determined by referencing a pre-compiled association map (termed the cabling map) that contains the corresponding plaquette index for every allowed FED, link, and ROC combination. Each ROC entry in the cabling map also contains the offsets and reflections appropriate to transform from the ROC to plaquette coordinate frame, so the cabling map is used to determine the digi row and column address as well. Digis on the same plaquette are grouped together and stored in a container class representing the plaquette. These containers are organized by plaquette index and stored as a collection for further reconstruction. If the raw word is an error word, it is stored in a separate collection containing error information for monitoring in DQM (described in Sec. 4.4.3 and 4.4.4).

An additional function of the Pixel RawToDigi package is to create raw Pixel data from digis during the last step of detector simulation. Each digi is translated into a 32-bit raw word using a reverse cabling map (created by iterating over all associations in the cabling map) to determine the correct FED, link, and ROC number and pixel address on ROC. Pairs of translated words are then joined into 64-bit words and grouped according to FED index. Last, a 64-bit header and trailer are written to encapsulate the raw collection for each FED following the format used for the S-link.

4.4.3 Error Handling in Pixel RawToDigi

The Pixel RawToDigi package records information about problems that occur during online data acquisition or offline translation of raw words into digis. Problems during online data acquisition are identified from error words stored by the FED in the raw data, as discussed in Sec. 4.3. Problems that could occur during offline translation include online addresses that don't correspond to an entry in the cabling map, translated pixel row and column values that exceed the bounds of the plaquette, disagreement between the FED index of the raw data buffer being read out compared to the FED index encoded in the 64-bit header, or disagreement between the number of raw data words received compared to the number of words encoded in the 64-bit trailer. Information about each error is saved in a C++ container class to be monitored in the first level of DQM.

4.4.4 Data Quality Monitoring

Data Quality Monitoring (DQM) refers to a group of computer processes and human operators that monitor information produced at all levels of reconstruction in order to identify problems with CMS data-taking. Data quality is monitored based on a selection of events reconstructed at the HLT (Online DQM) and for all events reconstructed offline at T0 or the T1 sites (Offline DQM). DQM processes devoted to the local reconstruction of a subdetector are monitored by experts chosen by that subdetector. This section describes the DQM software used to monitor Pixel information during CMS operation.

DQM software must perform two basic functions: access the products of reconstruction to histogram quantities important to data quality, and display these histograms in a human-readable Graphical User Interface (GUI) so experts can utilize them. The first function is accomplished by DQM processes dedicated to several levels of Pixel local reconstruction:

- Error: The types of error, as well as FED and link addresses, are monitored. Additional information is monitored for certain kinds of errors.
- Digi: The occupancy and charge of digis is monitored.

- Cluster: The occupancy, charge, and size (in pixels) of clusters is monitored. Separate information is shown for clusters used to make a track (on-track clusters) and clusters not joined to a track (off-track clusters).

The DQM GUI is a web application that outputs DQM information to a web address and can be run on any standard web browser. The GUI has a point-and-click interface, shown in Fig. 4.9. Users can select the dataset, run number, and level of detail to monitor by clicking on their respective entries in the GUI. The GUI has several levels of information available for display. The top level for Pixel contains a summary map of FED performance by lumi section with a green to red color code, shown in figure Fig. 4.10. Green indicates all monitored quantities fall within limits judged acceptable by subdetector experts, red indicates a quantity may fall outside of those limits and require further investigation, and white indicates no data was received from the FED. In the example shown, all FEDs display white until Pixel is turned on at lumi section 50, at which point monitoring indicates a possible problem with data from FED 20 beginning at lumi section 76.

Lower levels of the GUI display histograms of more detailed information down to the resolution of a plaquette. Summary histograms are also made at the ladder and layer level in the barrel, and the blade and disk level in the endcaps. Error information is displayed at the FED level. Fig. 4.11 shows DQM displays of error information. The picture on the left displays how many times each monitored error has occurred in a given FED, while the picture on the right displays how many times any error has occurred in a given link for each FED. Some errors are expected during normal operation, but the appearance of thousands of errors in a matter of minutes or hours notifies an expert to issue a resync command to the FED, clearing its memory buffers before resuming data collection. Such incidents are reported to the Pixel group and investigated further if they occur repeatedly.

Fig. 4.12 shows DQM displays of digi information. The picture on the left displays the average sum ADC charge value collected on a barrel ladder per event, while the

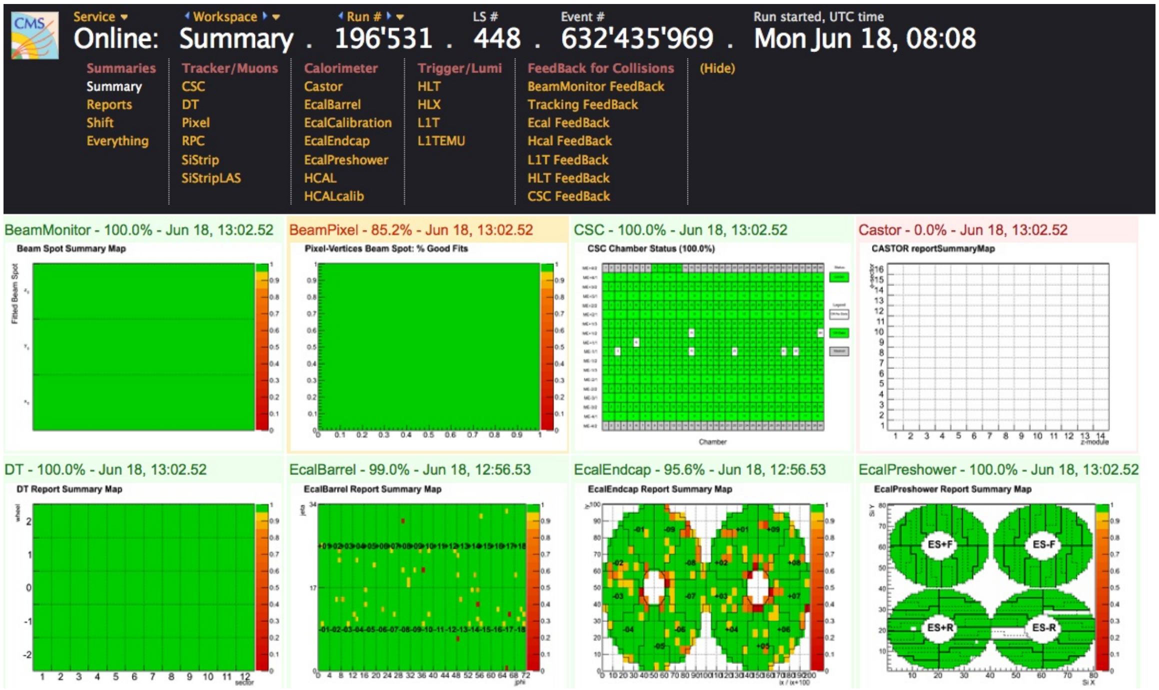

Figure 4.9: The interface for the DQM GUI.

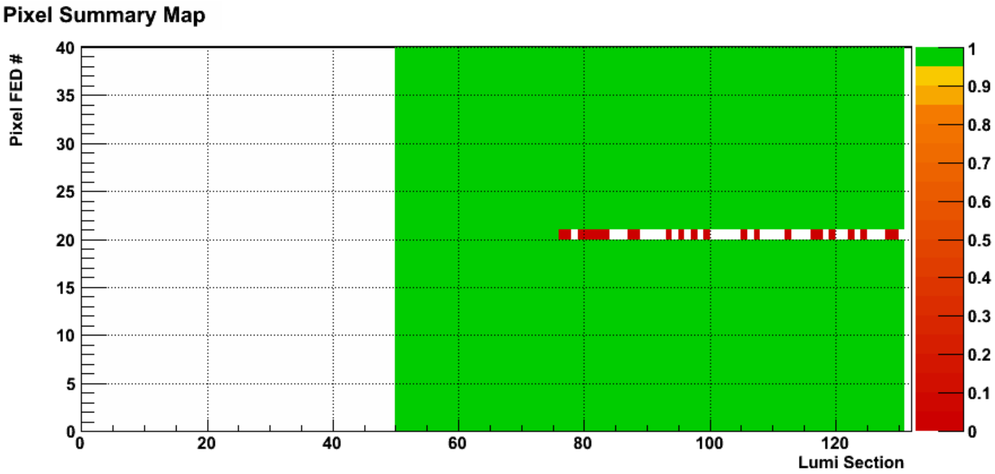

Figure 4.10: An example of the summary map of Pixel FED status for a run. Green indicates all monitored quantities fall within limits judged acceptable by subdetector experts, red indicates a quantity may fall outside of those limits and require further investigation, and white indicates no data was received from the FED.

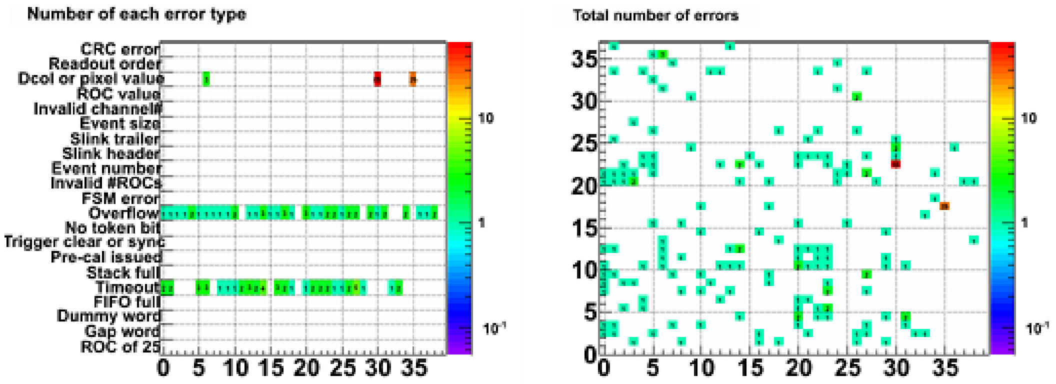

Figure 4.11: Example histograms of error information available in the DQM GUI. The picture on the left displays how many times each monitored error has occurred in a given FED, while the picture on the right displays how many times any error has occurred in a given link for each FED.

picture on the right displays the average number of digis reconstructed per event for a given ladder index. In each case, the blue lines in the display represent acceptable bounds. New noisy pixels (pixels that register charge deposit with pathologically high frequency) are identified from spikes in the ndigis plot and disabled. Poor threshold settings used in ADC charge digitization can be identified from the display of mean ADC charge value.

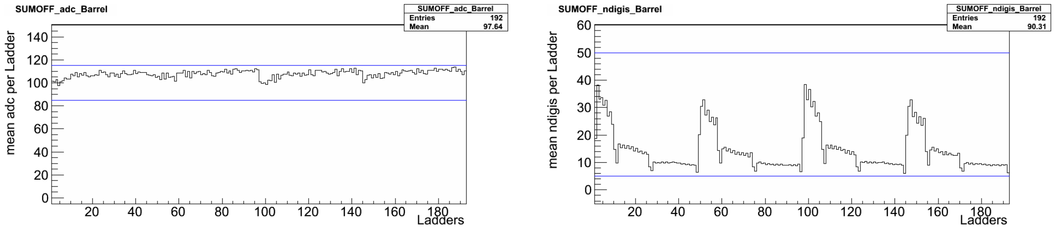

Figure 4.12: Example histograms of digi information available in the DQM GUI. The picture on the left displays the average sum ADC charge value collected on a barrel ladder per event, while the picture on the right displays the average number of digis reconstructed per event for a given ladder index.

Fig. 4.13 shows DQM displays of charge cluster information. The picture on the left displays the charge distribution for on-track clusters, while the picture on the right displays the occupancy (in the CMS coordinate frame) of such clusters. The charge distribution should display a Landau-like shape with a peak around 22 keV;

any significant deviation from such a distribution would invalidate a run for use in physics analysis and prompt investigation. The occupancy plot can be used to identify dead sensors and flag them for possible repair.

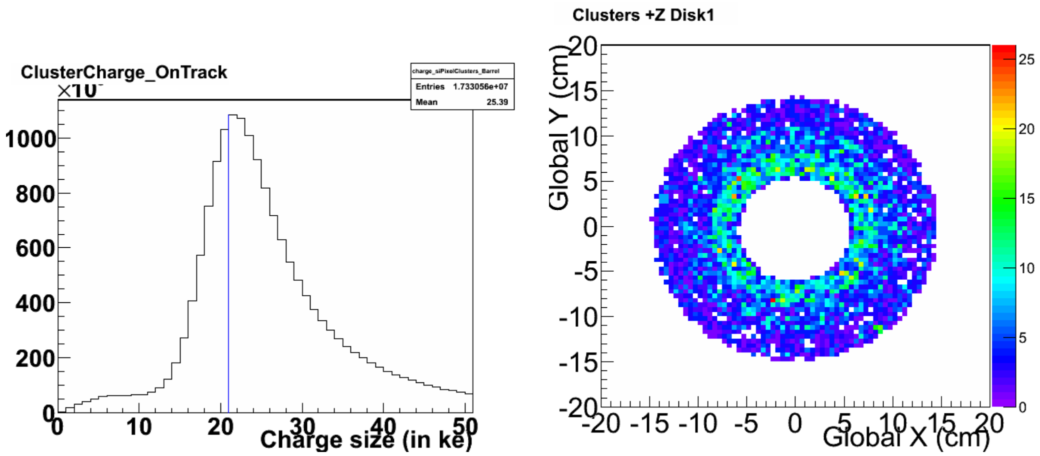

Figure 4.13: Example histograms of cluster information available in the DQM GUI. The picture on the left displays the charge distribution for on-track clusters, while the picture on the right displays the occupancy (in the CMS coordinate frame) of such clusters.

Chapter 5

Measurement of the Production Cross Section

5.1 Introduction

The measurement of the simultaneous production of two J/ψ mesons in the collision of protons at $\sqrt{s} = 7$ TeV provides general insight into how particles are produced during proton collisions in the LHC. With the high flux of incoming partons at the LHC, there is a high probability that more than one pair of the microscopic dynamic constituents of the proton, the gluons and quarks (commonly called partons), scatters in the proton-proton collision Kom et al. (2011). These multi-parton scattering contributions are difficult to address within the framework of perturbative Quantum Chromodynamics (QCD) and experimental studies are needed (see e.g. Ref. Ko et al. (2011) and references therein). The general assumption is that single parton scattering (SPS) is the dominant process. Double parton scattering (DPS) and higher-order multiple parton interactions are widely invoked to account for observations that cannot be explained otherwise, such as the rates for multiple heavy flavor production. New findings can have far reaching implications for LHC physics and will allow creation of more realistic simulations of particle production. The decay of the

J/ψ into muons provides a clean signal in a parton-parton interaction regime that is complementary to studies that are based on hadron jets. Multiple parton interactions can lead to distinct differences in event variables that probe pair-wise balancing, such as the absolute rapidity difference $|\Delta y|$ between the two J/ψ mesons Kom et al. (2011); Gaunt et al. (2011). Two J/ψmesons produced via SPS interaction are strongly correlated, resulting in small values of $|\Delta y|$. Large values of $|\Delta y|$ are possible for production due to DPS.

In contrast to earlier experiments where quark-anti-quark annihilation dominated Badier et al. (1982, 1985), in the case of proton-proton collisions at the LHC, the dominant production process is gluon-gluon fusion Humpert and Mery (1983). At parton level the two J/ψmesons are either produced as color singlet states or color octet states that turn into singlets after emitting gluons. Color octet contributions at double J/ψtransverse momenta below 15 GeV/c and low invariant masses are expected to be negligible, but play a greater role as transverse momenta increase Berezhnoy et al. (2011); Qiao et al. (2010). According to next-to-leading order Quantum Chromodynamics (QCD) calculations, contributions from color singlet heavy-quark pair production can also be enhanced at higher transverse momenta Campbell et al. (2007); Artoisenet et al. (2007); Gong and Wang (2008). The CMS experiment provides access to transverse momentum measurements above 15 GeV/c. Theoretical calculations of double J/ψproduction via SPS, based on leading order color singlet, states predict a cross section of 4 nb within the LHCb acceptance region Berezhnoy et al. (2011, 2012), with an uncertainty of about 30% Novoselov (2011). This prediction is just below the measured value of $5.1 \pm 1.0 \pm 1.1$ nb recently published by the LHCb experiment, though DPS contributions could potentially account for the difference Aaij et al. (2012). The CMS experiment samples a J/ψregime complementary to LHCb, with coverage of higher transverse momenta and lower rapidity values. Hence, double J/ψcross section measurements by CMS provide new information for model-builders.

The bottomonium ground-state meson η_b is expected to decay into two J/ψ mesons in analogy to the η_c charmonium ground-state that decays into two ϕ-mesons Collaboration (2006). However, explicit calculations based on Nonrelativistic QCD (NRQCD) Braaten et al. (2001); Maltoni and Polosa (2004); Jia (2008) predict this decay mode to be highly suppressed, so any observation could indicate the limitations of present NRQCD approaches. Other predicted resonant states that could decay into two J/ψmesons are exotic tetra charm-quark states Berezhnoy et al. (2011). Furthermore, a CP-odd Higgs e.g. in Next-to-Minimal Supersymmetric Standard Models (NMSSM) Dermisek and Gunion (2005) is predicted with mass close to the η_b meson. The mixing between those two states can alter the behavior of η_b with respect to QCD predictions Domingo et al. (2009); Domingo (2011). No evidence for the CP-odd Higgs was found by CMS in the $\mu^+\mu^-$ invariant mass spectrum between 5.5 GeV/$c^2$and 14 GeV/c^2 Chatrchyan et al. (2012b). The η_b state has been observed in radiative transitions with the BaBar experiment Aubert et al. (2009); the double J/ψ decay was probed with the CDF detector, but no significant resonant production was identified Collaboration (2006).

5.1.1 Analysis Strategy

The goal of this analysis is to measure the cross section for prompt double J/ψ production with data recorded by the CMS detector at a center-of-mass energy of 7 TeV, independent of production models. Therefore, acceptance corrections are calculated based on the measured J/ψ kinematics and efficiency corrections are calculated based on the measured decay-muon kinematics of each event. Monte Carlo (MC) samples for different production models with either strongly correlated J/ψ(SPS model) or less correlated J/ψ(DPS model) in the event are used to estimate the acceptance region and validate the correction method. They also provide guidance for the parameterization of event variable distributions. The SPS generator is a color singlet model Berezhnoy et al. (2011) implemented in Pythia 6 Sjostrand et al. (2006), the DPS generator is implemented in Pythia 8 Sjostrand et al. (2008) and uses a color singlet and color octet production model. The dominant background processes are non-prompt J/ψ (mostly from B-meson decays) and combinatorial background from a prompt J/ψ combined with two unassociated muons. Background components and their distributions are extracted from sideband regions in data or simulations of J/$\psi$from B-meson decays. Signal and background events are identified in data by applying muon quality criteria to reconstructed muons, requiring the presence of at least four muons in the event and two $\mu^+\mu^-$ combinations with an invariant mass within 250 MeVof the J/ψ mean mass value.

The cross section measurement is provided in a pre-defined region of the J/ψ acceptance that in turn is constrained by the muon identification and reconstruction capabilities of CMS. The differential cross section of double J/ψ production in bins of event variable x is calculated using the following equation:

$$\frac{d\sigma(pp\rightarrow\ \mathrm{J}/\psi\ \mathrm{J}/\psi + X)}{dx} = \sum_i \frac{n^i_{\mathrm{sig}}}{a_i\cdot\epsilon_i\cdot BF(\mathrm{J}/\psi\ \rightarrow\mu^+\mu^-)\cdot BF(\mathrm{J}/\psi\ \rightarrow\mu^+\mu^-)\cdot\Delta x\cdot\mathcal{L}} \tag{5.1}$$

with:

- the sum over events i in the interval Δx,
- n^i_{sig}, measured signal yield per event extracted with a maximum likelihood fit,
- a_i, acceptance, calculated on an event basis as the probability of the muons from J/ψ that are within the J/ψ acceptance and lie within the muon acceptance,
- ϵ_i, CMS detector efficiency calculated on an event basis for triggering, reconstructing, and identifying muons and J/ψ in the J/ψ acceptance,
- $\mathcal{L}$, total integrated luminosity of the dataset.

The total cross section in the J/ψ acceptance is determined by summing over all intervals Δx on an event-by-event basis. This analysis measures differential production in Δx bins of double J/ψ invariant mass (M_{JJ}), absolute separation in rapidity between the J/ψ($|\Delta y|$), and the double J/ψ transverse momentum, $p_{\mathrm{T}}^{\mathrm{JJ}}$.

A detailed description of the CMS detector can be found elsewhere Chatrchyan et al. (2008). The primary components used in this analysis are the silicon tracker and the muon systems. The tracker operates in a 3.8T axial magnetic field generated by a superconducting solenoid having an internal diameter of 6 m. The tracker consists of three cylindrical layers of pixel detectors complemented by two disks in the forward and backward directions. The radial region between 20 cm and 116 cm is occupied by several layers of silicon strip detectors in barrel and disk configurations, ensuring at least nine hits in the pseudorapidity range $|\eta| < 2.4$, where $\eta = -\ln\left[\tan\left(\theta/2\right)\right]$ and θ is the polar angle of the track measured from the positive z-axis of a right-handed coordinate system, with the origin at the nominal interaction point, the x-axis pointing to the centre of the LHC, the y-axis pointing up (perpendicular to the LHC plane), and the z-axis along the counterclockwise-beam direction. An impact parameter resolution around 15 μm and a p_{T} resolution around 1.5 % are achieved for charged particles with transverse momenta up to 100 GeV/c. Muons are identified in the range $|\eta| < 2.4$, with detection planes made of drift tubes, cathode strip chambers, and resistive plate chambers, embedded in the steel return yoke. The CMS detector response is simulated with a GEANT4 based MC Agostinelli et al. (2003).

5.2 Data and Monte Carlo Samples

5.2.1 Data Samples

The data considered in this analysis were obtained from proton-proton collisions with a 7 TeV center of mass energy recorded by the CMS detector during the year 2011. The only lumi sections considered are those certified for physics analysis in the JSON file:

`Cert_160404 − 180252_7TeV_PromptReco_Collisions11_JSON.txt`

with the exception of the Aug05 ReReco dataset, which used the following:

`Cert_170249 − 172619_7TeV_ReReco5Aug_Collisions11_JSON_v3.txt`

The exact datasets used for this analysis are given in Table 5.1, and correspond to a total integrated luminosity of $4.73 \pm 0.12\ \text{fb}^{-1}$ recorded by CMS. All luminosity estimates given for datasets are calculated using the pixelLumiCalc.py CMS (2013) script with the specified JSON file as input, considering only lumi sections within the run ranges and including the HLT path described in Table 5.1.

Table 5.1: Dataset name, run range, trigger version, and recorded integrated luminosity.

Dataset	Run Range	Trigger Path	$\mathcal{L}\,(\text{pb}^{-\infty})$
/MuOnia/Run2011A-PromptReco-v4/AOD	160431-167913	`HLT_Dimuon0_Jpsi_muon_v1-4`	1157
/MuOnia/Run2011A-05Aug2011-v1/AOD	170826-172619	`HLT_Dimuon0_Jpsi_muon_v6`	390
/MuOnia/Run2011A-PromptReco-v6/AOD	172620-173692	`HLT_Dimuon0_Jpsi_muon_v7`	707
/MuOnia/Run2011B-PromptReco-v1/AOD	175860-180252	`HLT_Dimuon0_Jpsi_muon_v7-11`	2714

Only lumi sections that contain the `HLT_Dimuon0_Jpsi_Muon` trigger path are used in this analysis. This trigger path is seeded by the presence of at least three separate L1 muon segments, and requires the presence of at least three L3 muon candidates, two of which have opposite charge and fit to a common vertex with a vertex fit probability > 0.5% and an invariant mass in the range 2.8-3.35 GeV/c^2. This trigger path was unprescaled over the data-taking period.

5.2.2 Monte Carlo Samples

This analysis utilizes simulated signal and expected background samples to identify suitable variables for a Maximum Likelihood fit, as well as to characterize the shape of signal and background events in the fit. These samples are described below, and summarized in Table 5.2. Unless otherwise specified, all privately produced samples were generated and reconstructed in `CMSSW_4_2_7_hltpatch3` using global tag `START42_V17`, and are publicly available and published in the CMS Data Aggregation Service under the `cms_dbs_ph_analysis_01` server.

Table 5.2: Simulated samples used, along with the number of generated events, assumed production cross section (where applicable), and number of events passing HLT.

Process	N_{gen}, (10^6)	$\sigma_{\mathrm{prod}}(\mu\mathrm{b}^{-1})$	N_{HLT}
DPS Prompt double J/ψ (no PU)	5.3	*	13648
DPS Prompt double J/ψ (w/ PU)	20	*	44937
DPS Prompt double J/ψ (no filter)	0.35	*	348500
SPS Prompt double J/ψ (w/ PU)	16	*	39771
SPS Prompt double J/ψ (no filter)	10	*	*
$B^0 \rightarrow$ J/ψ	4	26.5	34274
$B^+ \rightarrow$ J/ψ	5	29.8	42743
$B_s \rightarrow$ J/ψ	1.3	24.1	10681
$\lambda_b \rightarrow$ J/ψ	0.4	8.1	2814
J/ψ particle gun	100	*	*
Muon particle gun	12	*	*
Data substituted	4.4	*	$2.2 \cdot 10^6$
DPS substituted	4.0	*	$1.6 \cdot 10^6$
SPS substituted	4.0	*	$1.9 \cdot 10^6$
$\eta_b \rightarrow$ J/ψJ/ψ	3.5	*	6073

- DPS Prompt double J/ψ without pileup:

  At the generator level, Double Parton Scattering (DPS) prompt double

J/ψ events are produced in Pythia8 using the CTEQ6L1 pdf set, with double hard scattering and charmonium production enabled. Only J/ψ charmonium states are allowed and J/ψ are forced to decay to two muons (resulting in a four muon final state). A generator level filter was then applied to allow only events containing at least one J/ψ with $|\eta| < 3$ and $p_{\mathrm{T}} > 2$ GeV/c and three muons with $|\eta| < 2.5$ and $p_{\mathrm{T}} > 1$ GeV/c. This filter sped up reconstruction by eliminating approximately two-thirds of generated events, targeting only events unlikely to pass the HLT (finally selected events were compared with an unskimmed sample to ensure final efficiencies and event shapes were unaffected). In addition, only events passing the `HLT_Dimuon0_Jpsi_muon` trigger were reconstructed.

- DPS Prompt double J/ψ with pileup:
  Produced as in the case without pileup, but simulated MinBias events are mixed in after generation according to the guidelines intended to mimic Summer11 production.

- DPS Prompt double J/ψ with no filter:
  This sample was produced in the same way as the prompt sample with pileup, but no filter was applied at the generator level or HLT to remove events. Used to determine acceptance.

- SPS Prompt double J/ψ with pileup:
  The Single Parton Scattering (SPS) signal events were produced using the exact same method employed in a like simulation by LHCb Berezhnoy et al. (2012), wherein signal events are produced in standalone Pythia 6.426 interfaced to LHAPDF to use CTEQ5L parton distribution functions (pdfs). The generated collision event output and decay products were then put through standard full detector simulation in `CMSSW_4_2_9_HLT3` with global tag `START42_V17`, with pileup added in as described earlier. To speed up production, this sample employed a Pythia level filter requiring two J/ψ mesons in the event with $p_{\mathrm{T}} > 2$

GeV/c and $|y| < 2.5$, as well as three muons in the event fulfilling $p_{\mathrm{T}} > 2$ GeV/c for $|\eta| < 1.4$, or $p_{\mathrm{T}} > 1.5$ GeV/c for $1.4 < |\eta| < 2.5$.

- SPS Prompt double J/ψ with no filter:

  SPS events were produced as above, but not filtered and not reconstructed past the generator level. This sample was used for acceptance studies of SPS events.

- Non-prompt J/ψ with pileup:

  Non-prompt J/ψ are simulated through B-hadron decay to J/ψ. Bottom quark production is enabled in Pythia6, Pythia handles an initial round of hadronization and EvtGen handles subsequent decays, where a specified B-hadron type (B^0, B^+, B_s, or λ_b, as given in dataset name) is forced into a J/ψ to muons decay. This follows the Fall11 production of non-prompt J/ψ. The same generator level filter and mixing strategy for pileup as used in the DPS prompt J/ψ case are applied, and only events passing the `HLT_Dimuon0_Jpsi_Muon` trigger are reconstructed. These types of events always include a single displaced J/ψ, but there is no explicit requirement on a second J/ψ, so prompt, non-prompt, and misreconstructed J/ψ are all possible.

- J/ψ particle gun:

  Produced in `CMSSW_4_2_8_patch7` with global tag `START42_V17`, and only reconstructed to the GENSIM stage. Single J/ψ were generated using a Pythia6PtYDistGun with a flat p_{T} distribution from 0-50 GeV/c, and a flat rapidity distribution in $|y| < 2.5$. This sample is used in one method to determine the muon acceptance, as described in Section 5.4.

- Muon particle gun:

  Produced in `CMSSW_4_2_9_HLT3` with global tag `START42_V17`, and reconstructed to AODSIM but without selection on a trigger path. Single muons were generated using a Pythia6PtGun with a flat p_{T} distribution from 0-10 GeV/c, and a flat psuedorapidity distribution in $|\eta| < 2.4$. This sample is used to determine the offline reconstruction efficiency for low p_{T} muons, as described in Section 5.5.

- Data substituted:

  Events are simulated in Pythia 6 as described for SPS production, but the J/ψ and muon kinematics of the event are replaced with the J/ψ and muon kinematics of a data event passing the trigger, reconstruction, and selection requirements. This is only done if the double J/ψ energy of the generated event matches the data event to 1% difference, and the double J/ψ system direction is within 1.57 radians of the data event (otherwise, the generated event is skipped). The event is then input into CMSSW for full detector simulation and reconstruction. This is done repeatedly for each input data event, and the sample is used to determine the event's efficiency. Produced in `CMSSW_4_2_9_HLT3` with global tag `START42_V17`.

- DPS substituted:

  Following the same methodology as the data substituted case above, but using as input DPS produced events that passed the full trigger, reconstruction, and selection requirements.

- SPS substituted:

  Following the same methodology as the data substituted case, but using as input SPS produced events that passed the full trigger, reconstruction, and selection requirements.

- $\eta_b \rightarrow$ J/ψJ/ψ:

  Events are generated in CMSSW with Pythia6 using the CTEQ6L1 pdf set with $g + g \rightarrow \Upsilon + g$ production turned on and the Υ replaced with an η_b meson. Pythia was interfaced to EvtGen to perform the decays, and a decay card was tailored to force $\eta_b \rightarrow$ J/ψJ/ψ and J/$\psi \rightarrow \mu\mu$ decays. A generator level filter was then applied to allow only events containing at least one J/ψ with $|\eta| < 3$ and

$p_{\mathrm{T}} > 2$ GeV/c and three muons with $|\eta| < 2.5$ and $p_{\mathrm{T}} > 1$ GeV/c. Only events passing the `HLT_Dimuon0_Jpsi_muon` trigger were reconstructed.

5.3 Event Reconstruction and Selection

This analysis utilizes the `HLT_Dimuon0_Jpsi_Muon` trigger path, designed by the BPH-trigger group to provide a consistently unprescaled muon trigger to achieve the highest efficiency for J/ψ+ muon searches during the 2011 campaign. This trigger requires the presence of at least three muons, two of which must be oppositely charged and with a dimuon invariant mass in the interval between 2.8 and 3.35 GeV/c^2 and a vertex fit probability greater than 0.5% (as determined by a Kalman vertex algorithm).

All four muons used in the final event selection are required to belong to the `tracker muon` category, created using the arbitration algorithm described in James et al. (2006). Reconstruction of muons proceeds by associating segments in the muon chambers with tracks provided by the silicon tracker. A given muon segment can be associated with more than one silicon track at the time of reconstruction, allowing reconstructed muons to share segments in the muon system. An arbitration algorithm then assigns each muon segment to a unique muon track. Muons are further required to pass the following quality criteria: (i) the associated track segment must have hits in at least two layers of the Pixel tracker and at least 11 total inner tracker hits (Pixel and Strip detectors combined), and (ii) the inner track fit χ^2 divided by degrees of freedom has to be less than 1.8. Muons with a transverse impact parameter greater than 3 cm or a longitudinal impact parameter greater than 30 cm are excluded.

To find J/ψ candidates, all muon candidates in an event passing the above quality criteria are then combined into opposite-sign electric charge pairs. These dimuon candidates are fit to a common vertex using a Kalman Vertex algorithm Fruhwirth (1987b). The dimuon invariant mass after the vertex fit has to stay within 2.8-3.35 GeV/c^2 and the fit probability has to be greater than 0.5%. The final event selection requires that two J/ψ candidates are created from four unique muon candidates. If there is more than one double J/ψ combination in an event, the highest vertex-fit probability candidate is chosen as the first J/ψ, and the second highest vertex probability candidate is chosen as the second J/ψ. For signal MC samples in

Table 5.3: The yield after implementing successive quality cuts in event selection for double J/ψ candidates.

	2011 Data		
Requirement	N$_{\mathrm{evt}}$	Fraction$_{\mathrm{step}}$	Fraction$_{\mathrm{total}}$
Trigger	1892853	1	1
>3 muons found	1155516	0.6105	0.6105
1 matched segment/ muon	504596	0.4367	0.2666
2 pixel layers / track	367954	0.7292	0.1944
11 tracker hits / track	312557	0.8494	0.1651
track $d_0 < 3$ cm, $dZ < 30$ cm	312386	0.9995	0.1650
track $\chi^2/ndof < 1.8$	275801	0.8829	0.1457
muon acceptance	211457	0.7667	0.1117
two $\mu^+\mu^-$ candidates	120168	0.5683	0.0635
J/ψ fit probability > 0.005	86732	0.7218	0.0458
J/ψ mass$\in$[2.8,3.35] GeV/c^2	7951	0.0917	0.0042
J/ψ $d_0 < 2$ cm	7934	0.9979	0.0042
J/ψ acceptance	4958	0.6249	0.0026
two J/ψ candidates	2755	0.5557	0.0015
3 μ L3 matching	2616	0.9495	0.0014
Event variable criteria	1043	0.3987	0.0006

which pileup is included, this selection process found the correct dimuon combinations for 99.7% of the selected events.

In addition, a muon momentum and a geometrical acceptance are imposed. At least three muons must pass the tag and probe Wöhri et al. (2011) acceptance criteria:

- $|\eta^\mu| < 1.2$ and $p_{\mathrm{T}}^{\mu} > 3.5$ GeV/c OR
- $1.2 < |\eta^\mu| < 1.6$ and $p_{\mathrm{T}}^{\mu} > 3.5 \rightarrow 2.0$ GeV/c (where p_{T} scales linearly with $|\eta|$) OR
- $1.6 < |\eta^\mu| < 2.4$ and $p_{\mathrm{T}}^{\mu} > 2.0$ GeV/c

and be matched to muon candidates that fired the trigger. To match both, the offline reconstructed muon and the muon reconstructed by the trigger have to agree within an azimuthal angle and pseudorapidity range defined as: $\sqrt{\Delta\phi^2 + \Delta\eta^2} < 0.1$, and have a p_{T} difference no greater than 10 GeV/c. The acceptance regime for the fourth muon that is not associated with the trigger is wider:

- $|\eta^{\mu}| < 1.2$ and $p_{\mathrm{T}}^{\mu} > 3.0$ GeV/c OR
- $1.2 < |\eta^{\mu}| < 2.4$ and $|p|^{\mu} > 3.0$ GeV/c

Each J/ψ must fulfill the acceptance requirement:

- $|y^{\mathrm{J}/\psi}| < 1.2$ and $p_{\mathrm{T}}^{\mathrm{J}/\psi} > 6.5$ GeV/c OR
- $1.2 < |y^{\mathrm{J}/\psi}| < 1.43$ and $p_{\mathrm{T}}^{\mathrm{J}/\psi} > 6.5 \rightarrow 4.5$ GeV/c (where p_{T} scales linearly with $|y|$) OR
- $1.43 < |y^{\mathrm{J}/\psi}| < 2.2$ and $p_{\mathrm{T}}^{\mathrm{J}/\psi} > 4.5$ GeV/c

The two J/ψ candidates in an event are categorized according to their transverse momentum such that J/ψ^1 refers to the higher-p_{T} J/ψ and J/ψ^2 refers to the lower-p_{T} J/ψ of the pair.

In addition to the two $\mu^+\mu^-$ invariant masses close to the J/ψ resonance mass, two event variables are used that are sensitive to the prompt double J/ψ topology:

- the proper decay length of the highest-p_{T} J/ψ candidate, $ct^{\mathrm{J}/\psi}$. The primary vertex for an event is defined as the vertex created by charged particle tracks with the the highest sum of transverse momentum squared that can be fit to a common position without beam spot constraint. The J/ψ candidates are considered secondary vertices. If the muons from the J/ψ candidates are also joined to the primary vertex, they are removed from the primary vertex and the primary vertex is refit. The left plot of Fig. 5.1 demonstrates that this definition of primary vertex matches up well with the true generated event origin in simulated events with pileup. The refit primary vertex information is then used for the $ct^{\mathrm{J}/\psi}$ determination. The proper decay length is calculated from the decay length in the laboratory frame $L_{xy}^{\mathrm{J}/\psi} = (\vec{r_{\mathrm{T}}}\vec{p_{\mathrm{T}}}^{\mathrm{J}/\psi})/|p_{\mathrm{T}}^{\mathrm{J}/\psi}|$, where $\vec{r_{\mathrm{T}}}$

is the vector pointing from the primary vertex to the J/ψ vertex in the transverse plane: $ct^{\mathrm{J}/\psi} = (m^{\mathrm{J}/\psi}/p_{\mathrm{T}}^{\mathrm{J}/\psi}) \cdot L_{xy}^{\mathrm{J}/\psi}$. The proper decay length is required to range from -0.05 cm to 0.1 cm.

- the so-called separation significance, $d^{\mathrm{J}/\psi}$. It is calculated from the difference in position $\Delta\vec{r}$ between the two J/ψ candidate decay vertices and the uncertainty of the distance, $\sigma_{\Delta\vec{r}}$, which includes the uncertainty of the vertex given by the Kalman fit and the uncertainty of the muon track fit: $d^{\mathrm{J}/\psi} = \Delta\vec{r}/\sigma_{\Delta\vec{r}}$. The requirement $d^{\mathrm{J}/\psi} < 8$ is imposed. From simulations it is determined that the variables are in agreement between SPS and DPS production, shown in Fig. 5.1. Furthermore, from data samples it is established that the variables are in agreement between low pileup (less than 6 primary vertices) and high-pileup (more than 6 primary vertices) scenarios. The behavior is confirmed with signal MC samples generated with and without pileup.

The event reduction due to these offline requirements is shown in Table 5.3. From a sample of proton-proton collisions taken in 2011 corresponding to an integrated luminosity of 4.73 ± 0.12 fb^{-1} CMS (2013), 1043 double J/ψ events are found.

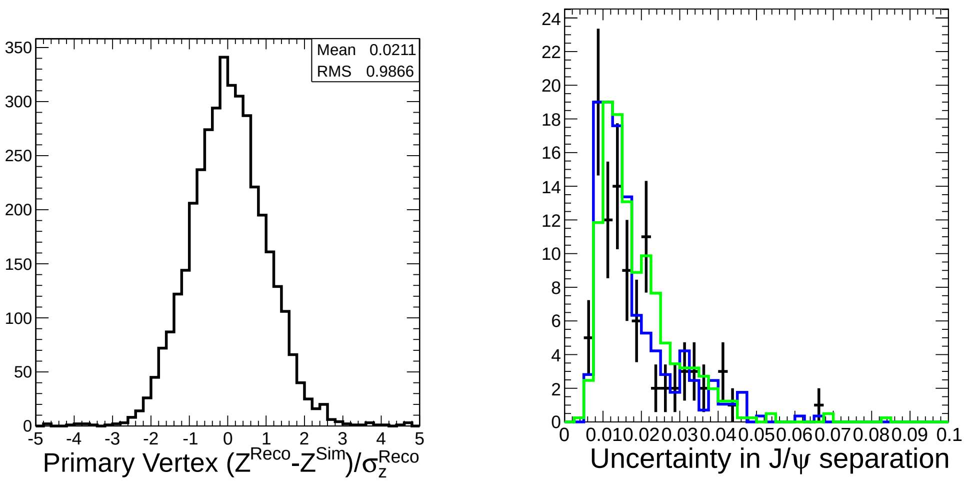

Figure 5.1: The left plot shows the difference between the reconstructed primary vertex position and the generated event origin divided by the reconstruction uncertainty (all in the Z-direction) based on SPS signal MC with pileup. The right plot shows position uncertainty in data (in black, with statistical error shown) overlayed with SPS (blue) and DPS (green) signal MC for selected events with J/ψ separation less than 1 mm. The MC distributions have been scaled to the size of the data distribution for the overlay.

5.4 Acceptance

The muon acceptance requirements reflect the geometric coverage of the CMS detector, as well as the muon momentum necessary to reach the muon chambers in a 3.8T magnetic field. The muon acceptance region is defined based on studies of simulated prompt double J/ψ events, and the J/ψ acceptance region is then defined based on the muon acceptance requirements. Acceptance corrections are determined on an event-by-event basis by repeatedly simulating the decay of both J/ψ in the event into muons based on the measured J/ψ four-momenta.

5.4.1 Definition of the Acceptance Region

Figure 5.2 shows the kinematics of generated prompt J/ψ particles, as well as of their muon decay products.

In order for a muon to be detected, it must fall within the pseudo-rapidity range covered by the inner silicon tracker and muon stations. In addition, it must have sufficient momentum to penetrate the detector material prior to the muon stations, and sufficient transverse momentum if in the Barrel region to reach the muon stations without being deflected back into the inner tracker by the 3.8T solenoidal magnetic field. Figure 5.3 shows the kinematic distribution of reconstructed signal MC muons that pass the muon quality requirements described in Section 5.3.

Previous studies Wöhri et al. (2011) have shown that a kinematic acceptance region of

- $|\eta^{\mu}| < 1.2$ and $p_{\mathrm{T}}^{\mu} > 3.5$ GeV/c OR
- $1.2 < |\eta^{\mu}| < 1.6$ and $p_{\mathrm{T}}^{\mu} > 3.5 \rightarrow 2.0$ GeV/c OR
- $1.6 < |\eta^{\mu}| < 2.4$ and $p_{\mathrm{T}}^{\mu} > 2.0$ GeV/c

does not depopulate the sample based on the transverse momentum (p_{T}) and psudo-rapidity (η) of the three highest p_{T} muons in an event, as shown in Fig. 5.3. They

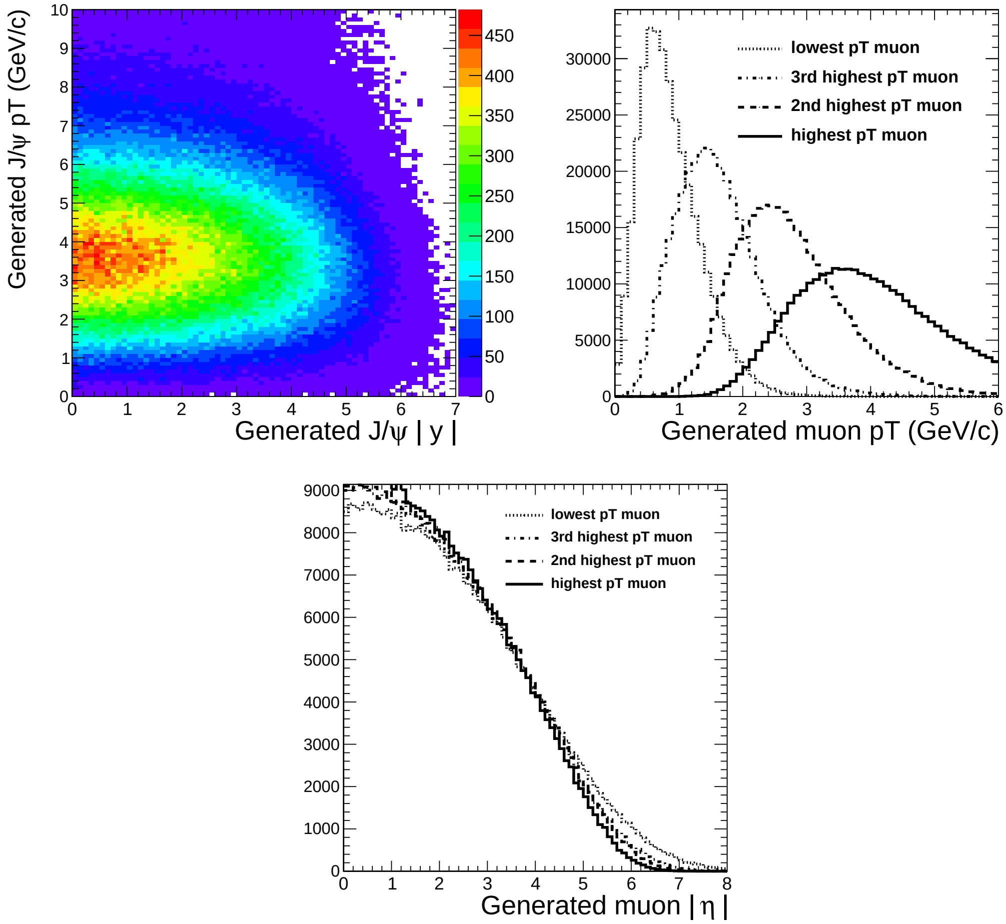

Figure 5.2: Kinematic distribution of unfiltered prompt J/ψ particles in DPS MC, and transverse momentum and pseudorapidity of their muon decay products distinguished by their p_{T} values (all at generator level).

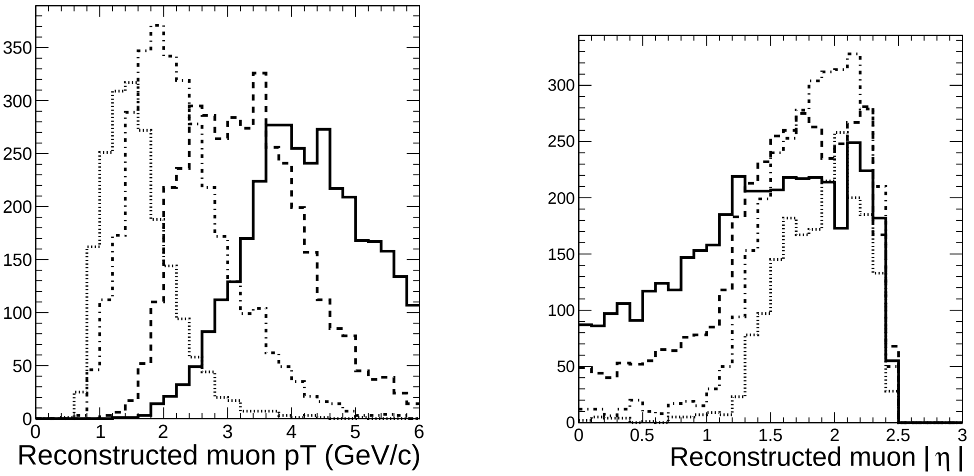

Figure 5.3: Kinematic distribution of pT-sorted reconstructed muons from unfiltered, simulated DPS prompt J/ψ sample.

were designed to ensure that the offline muon reconstruction efficiency is always higher than 50% with reasonable systematic uncertainty. However, the lowest p_{T} muon per signal event frequently falls outside of this acceptance region, as shown in Fig. 5.4 with signal MC events.

In order to avoid a 40% reduction in signal yield, a looser acceptance region for the fourth muon was defined based on the kinematic distribution of the lowest p_{T} muon in signal MC events shown in Fig. 5.4. The final muon acceptance requirements are defined as three muons in the region:

- $|\eta^{\mu}| < 1.2$ and $p_{\mathrm{T}}^{\mu} > 3.5$ GeV/c OR
- $1.2 < |\eta^{\mu}| < 1.6$ and $p_{\mathrm{T}}^{\mu} > 3.5 \to 2.0$ GeV/c OR
- $1.6 < |\eta^{\mu}| < 2.4$ and $p_{\mathrm{T}}^{\mu} > 2.0$ GeV/c

and a fourth muon within a looser acceptance region of:

- $|\eta^{\mu}| < 1.2$ and $p_{\mathrm{T}}^{\mu} > 3.0$ GeV/c OR
- $1.2 < |\eta^{\mu}| < 2.4$ and $|p|^{\mu} > 3.0$ GeV/c

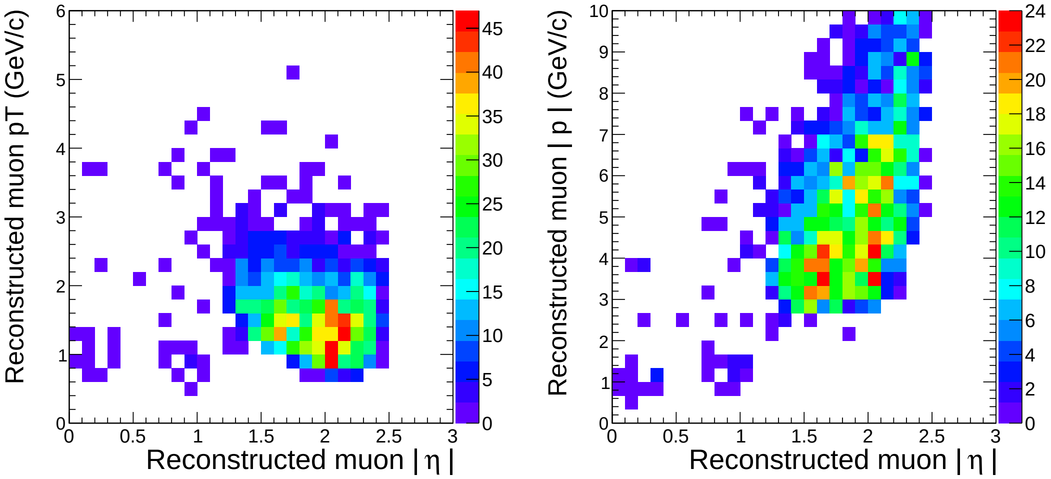

Figure 5.4: Kinematic distribution of the lowest p_{T} muon per event from unfiltered, simulated DPS prompt J/ψ sample. The left plot displays p_{T} vs $|\eta|$, while the right plot displays total momentum vs $|\eta|$.

Because both of the muon decay products from at least one of the J/ψ will need to pass the tighter muon criteria, the choice of J/ψ acceptance is driven by this requirement. The muon acceptance is probed using the J/ψ particle gun MC sample. The definition of the J/ψ acceptance region is based on the probability for the muons from a J/ψ to fall within the muon acceptance requirements (defined above). The probabilities (based on J/ψ p_{T} and $|y|$) for both muons to pass the tight muon acceptance or have one tight and one loose muon are shown in Fig. 5.5. The acceptance region boundary in J/ψ p_{T} and $|y|$ for the two J/ψ mesons is indicated by the red line in the figure. It is as inclusive as possible, while avoiding unpopulated bins:

- $|y^{J/\psi}| < 1.2$ and $p_{\mathrm{T}}^{J/\psi} > 6.5$ GeV/c OR
- $1.2 < |y^{J/\psi}| < 1.43$ and $p_{\mathrm{T}}^{J/\psi} > 6.5 \rightarrow 4.5$ GeV/c (where p_{T} scales linearly with $|y|$) OR
- $1.43 < |y^{J/\psi}| < 2.2$ and $p_{\mathrm{T}}^{J/\psi} > 4.5$ GeV/c

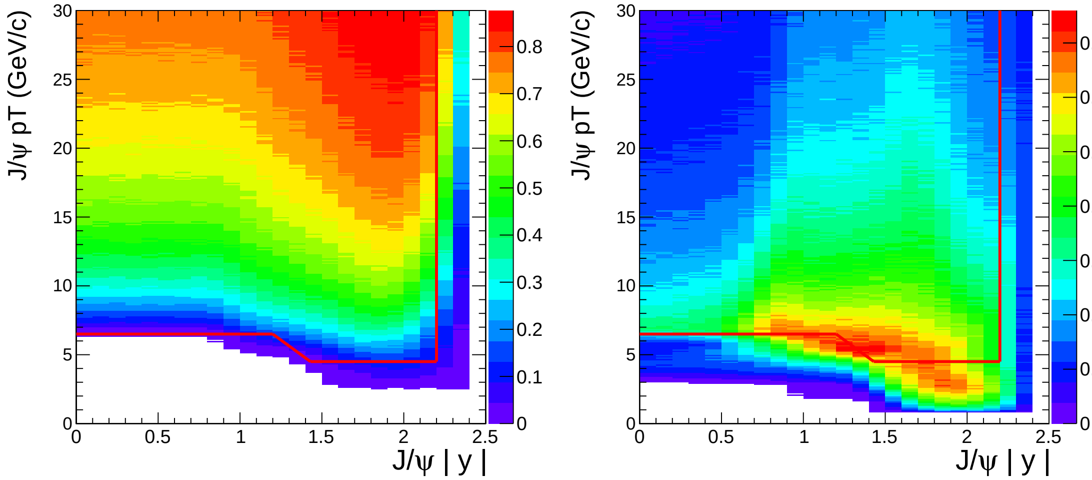

Figure 5.5: The probability for the decay muons from a J/ψ to fall within the tight muon acceptance criteria (left) or have a single muon within the loose acceptance criteria (right) based on a simulated J/ψ particle gun sample, with 25 bins in $|y|$ and 300 bins in p_{T}, and the chosen acceptance region delineated in red.

This definition covers a region that is mostly complementary to the one accessible by the LHCb experiment Berezhnoy et al. (2012), as shown in Fig. 5.6.

5.4.2 Event-by-Event Acceptance Correction

For the evaluation of the muon acceptance on an event-by-event basis, the two J/ψ mesons in the event are decayed repeatedly in simulation using their measured four-momenta. The acceptance correction a_i for a given event i is the number of times the resulting decay muons pass the muon acceptance criteria, N_i^{Pass}, divided by the total number of trials for the event, N_i^{Tot}: $a_i = N_i^{\mathrm{Pass}}/N_i^{\mathrm{Tot}}$. It is assumed that the angle of the decay muons with respect to the direction of flight of the parent J/ψ in the J/ψ rest frame is isotropically distributed. Deviations from this assumption are considered and discussed later. Ten thousand decays are simulated for each value a_i.

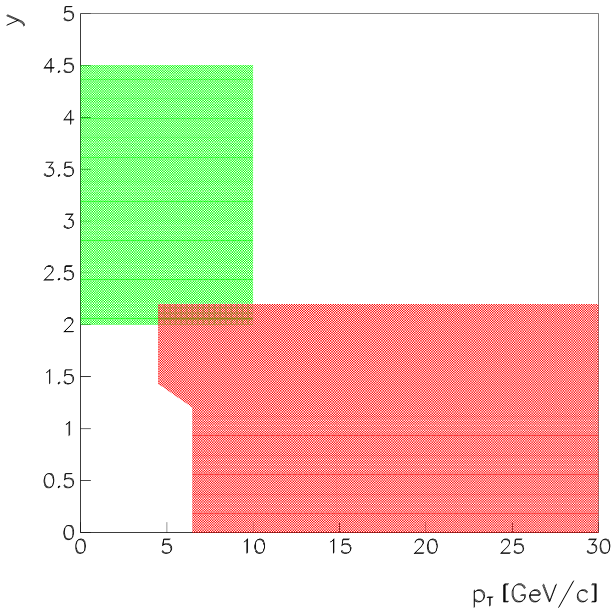

Figure 5.6: The single J/ψ acceptance region of CMS (red) and LHCb (green).

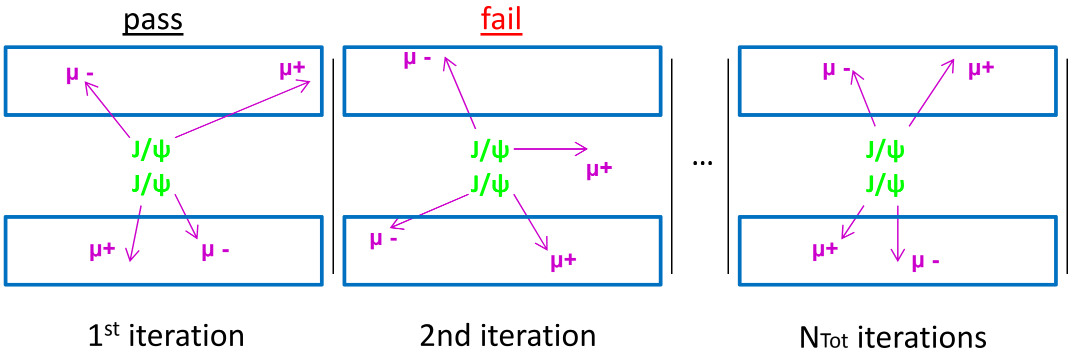

Figure 5.7: Conceptual illustration of the procedure used to obtain the event acceptance value a_i. The blue boxes represent the CMS muon acceptance region; any decay muon falling outside of that region causes the decay to fail. Each double J/ψ event is repeatedly decayed N_i^{Tot} times, with the direction of the decay muons assumed to be isotropically distributed in the J/ψcenter-of-mass frame. The muons are then subjected to the muon acceptance criteria in the detector frame and the value a_i is calculated as the number of resulting events to pass the muon acceptance criteria, N_i^{Pass}, divided by N_i^{Tot}.

5.4.3 Closure Test

The event-by-event acceptance correction procedure is validated with signal SPS and DPS MC samples. They are generated with unpolarized J/ψ. For each sample of N_{J} events within the J/ψ acceptance region, the muon acceptance criteria is applied to obtain a sample of N_μ survivors. This sample corresponds to events in data after efficiency correction.

For each of the surviving N_μ events, the event-based acceptance corrections a_i are calculated as described above. The corrected number of signal events within the J/ψ acceptance, N'_{J}, is then calculated as $N'_{\mathrm{J}} = \sum_i^{N_\mu} 1/a_i$. The matching between N_{J} and N'_{J} represents the closure for this method of acceptance correction. Systematic uncertainty is calculated as:

$$\mathrm{Error} = \pm\frac{|N'_{\mathrm{J}} - N_{\mathrm{J}}|}{N'_{\mathrm{J}} + N_{\mathrm{J}}} \tag{5.2}$$

This is the deviation of the original yield within the J/ψacceptance region compared to the corrected yield. The uncertainty is dominated by the sample size N_μ which consequently limits the precision of N'_{J}. The values of N_{J} and N'_{J} determined in bins of the double J/ψ invariant mass are shown in Table 5.4, in bins of the absolute separation in rapidity in Table 5.5, and in bins of the double J/ψ transverse momentum in Table 5.6.

Table 5.4: Values of N_{J} and N'_{J} in SPS and DPS MC in bins of double J/ψ invariant mass, M_{JJ}.

M_{JJ} (GeV/c^2)	6-8	8-13	13-22	22-35	35-80	Total
SPS N_{J}	380	4737	6971	736	32	12856
SPS N'_{J}	343	4621	6879	691	38	12571
DPS N_{J}	287	885	1159	958	821	4110
DPS N'_{J}	336	776	1200	935	871	4118

Table 5.5: Values of N_{J} and N'_{J} in SPS and DPS MC in bins of absolute separation in rapidity, $|\Delta y|$, between the J/ψ.

$\|\Delta y\|$	0-0.3	0.3-0.6	0.6-1	1-1.6	1.6-2.6	2.6-4.4	Total
SPS N_{J}	5009	3484	2495	1456	402	10	12856
SPS N'_{J}	4925	3294	2473	1521	343	16	12571
DPS N_{J}	665	498	382	527	711	1327	4110
DPS N'_{J}	592	537	295	494	784	1417	4118

Table 5.6: Values of N_{J} and N'_{J} in SPS and DPS MC in bins of double J/ψ transverse momentum, $p_{\mathrm{T}}^{\mathrm{JJ}}$.

$p_{\mathrm{T}}^{\mathrm{JJ}}$ (GeV/c)	0-5	5-10	10-14	14-18	18-23	23-40	Total
SPS N_{J}	6199	4988	1448	190	26	5	12856
SPS N'_{J}	6139	4735	1432	227	33	5	12571
DPS N_{J}	886	1385	1347	405	73	14	4110
DPS N'_{J}	625	1684	1307	422	68	12	4118

5.5 Efficiency

5.5.1 Event-by-Event Correction

The efficiency correction is determined on a per-event basis by repeatedly substituting an events measured decay muons into a generated event, which is then subjected to the complete CMS detector simulation and reconstruction chain. The efficiency correction ϵ_i for an event i is the rate at which the substitution events pass the trigger and reconstruction requirements. As the simulation is therefore based on measured muon kinematic quantities, model dependence is minimized. An SPS generator is used to simulate the underlying event. To approximately fullfill energy and momentum conservation in the complete event, a simulated candidate at the generator level has to match the following double J/ψ kinematics: (i) the energy in the double J/ψ system has to agree within 1% and (ii) the direction of flight of the double J/ψ system has to agree within an opening angle of 1.5 rad with the reconstructed direction of flight in the data event. Then the muons of the generated event are discarded and replaced by the measured ones. For each of the reconstructed candidate events i in the data sample, $n_{\mathrm{gen},i} = 4000$ different substitution events are generated ($n_{\mathrm{gen},i} = 2000$ for the same procedure on SPS/DPS MC), resulting in a total sample of about 4.4 million events. The events are then subjected to the trigger emulation and recontruction code. The efficiency correction ϵ_i is the number of triggered and reconstructed substitution events $n_{\mathrm{reco},i}$ divided by the number of generated substitution events, $n_{\mathrm{gen},i}$, for event i: $\epsilon_i = n_{\mathrm{reco},i}/n_{\mathrm{gen},i}$. The substitution procedure is diagrammed in Fig. 5.8. Figure 5.9 displays the distribution of ϵ_i for the data sample as well as reconstructed SPS and DPS simulation.

In order to ensure the statistical precision of the efficiency value, only reconstructed events with an efficiency ϵ_i greater than half of a percent are considered in both the data and MC samples.

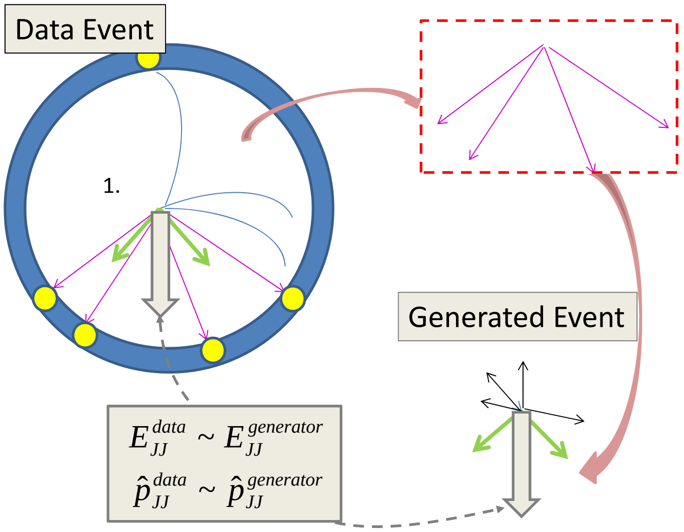

Figure 5.8: The substitution method to determine the trigger and detection efficiency based on the measured kinematics. The double J/ψ system in the laboratory serves as reference - its measured energy and direction of flight is compared to the system in a generated SPS event. If they match within certain criteria (see text) the four-momenta and charge assignment of the muons in the event are replaced by the measured values. Then the event is subjected to the full GEANT detector simulation and reconstruction chain. The procedure is repeated 4000 times for a given data event; the efficiency for the event is defined by the amount of substitution events that survive trigger, reconstruction, and selection criteria.

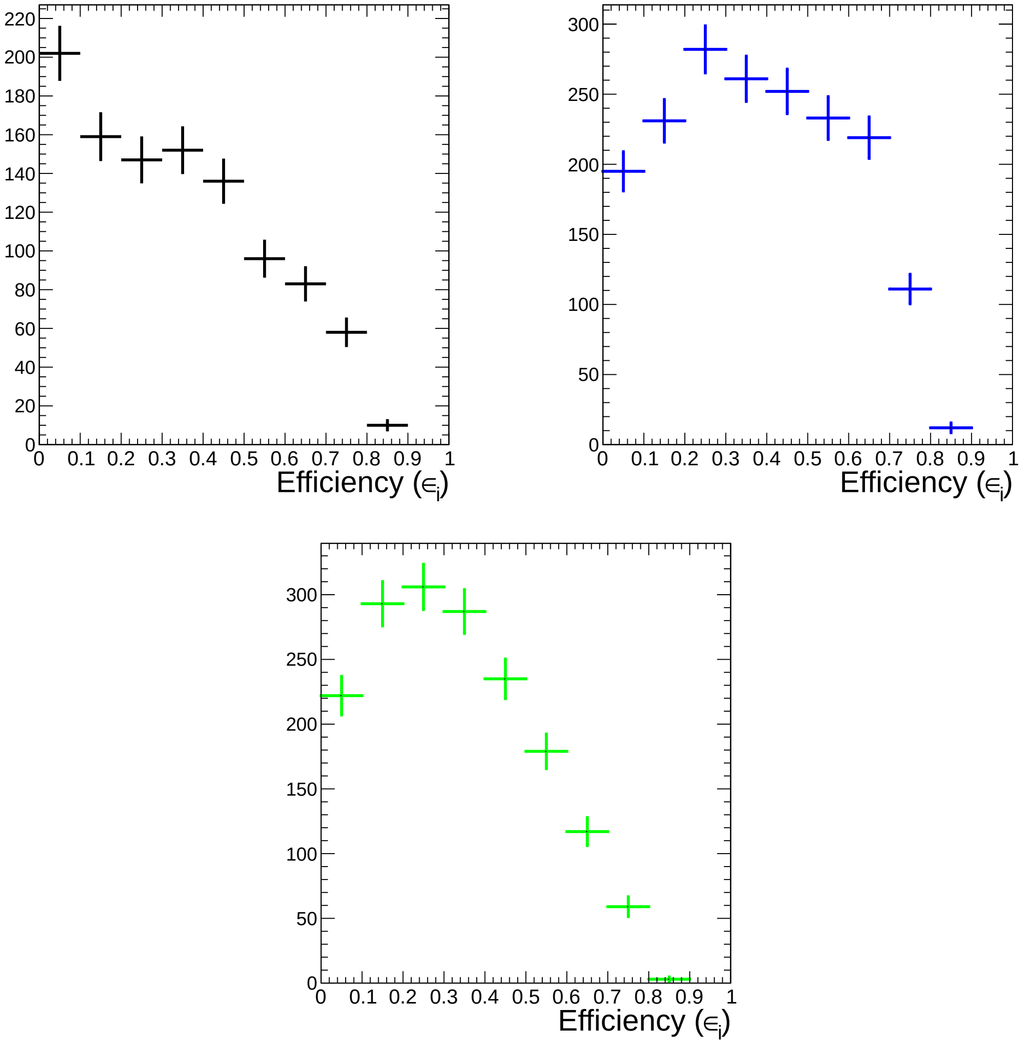

Figure 5.9: ϵ_i distribution in 1043 selected data events (black), SPS simulation (blue), and DPS simulation (green). Statistical error only is shown.

5.5.2 Scaling Factor

The acceptance criteria in data are based on measured muon momenta. Smearing of these quantities due to detector resolution causes a depopulation near the kinematic boundary. As this concerns mostly low efficiency events, the substitution method overestimates the efficiency. To account for this, an efficiency scaling factor is calculated. Average efficiency for samples of SPS and DPS MC is obtained as the sample size of events that survive the trigger and reconstruction requirements divided by the sample size after applying efficiency corrections. For comparison, the efficiency is also defined as the number of events in the sample surviving trigger and reconstruction criteria divided by the original number of events in the sample generated within the J/ψ and muon acceptance regions. The difference between these average efficiencies is used to develop a scaling factor for the event based efficiency correction method.

The average efficiency determined by generating events and stepping forward through the normal detector simulation is designated the *forward* efficiency, defined as:

$$\epsilon_{\mathrm{f}} = \frac{N_{\mathrm{Reco}}}{N_{\mathrm{Gen}}} \tag{5.3}$$

for a given kinematic bin (M_{JJ}, $|\Delta y|$, or $p_{\mathrm{T}}^{\mathrm{JJ}}$), where:

- N_{Gen} is the number of events generated in the J/ψ and muon acceptance region in the bin,
- N_{Reco} is the number of events generated in the bin that also pass the trigger and reconstruction selection criteria.

The comparable average efficiency determined by correcting back to the generated population using the event-based efficiency values, ϵ_i, is designated the *backward* efficiency, defined as:

$$\epsilon_b = \frac{N_{\mathrm{Reco}}}{N_{\mathrm{Gen}}} \tag{5.4}$$

for a given kinematic bin (M_{JJ}, $|\Delta y|$, or $p_{\mathrm{T}}^{\mathrm{JJ}}$), where:

- $N_{selected}$ is the number of events that also pass the trigger and reconstruction criteria in the bin,

- N_{Gen} is the size of the efficiency corrected population in the bin, calculated as the sum over events in that bin $N'_{\mathrm{Gen}} = \sum_{i=1}^{N_{\mathrm{Reco}}} \frac{1}{\epsilon_i}$.

The backward efficiency from data events in bins of several double J/ψ kinematic variables is shown in Fig. 5.10.

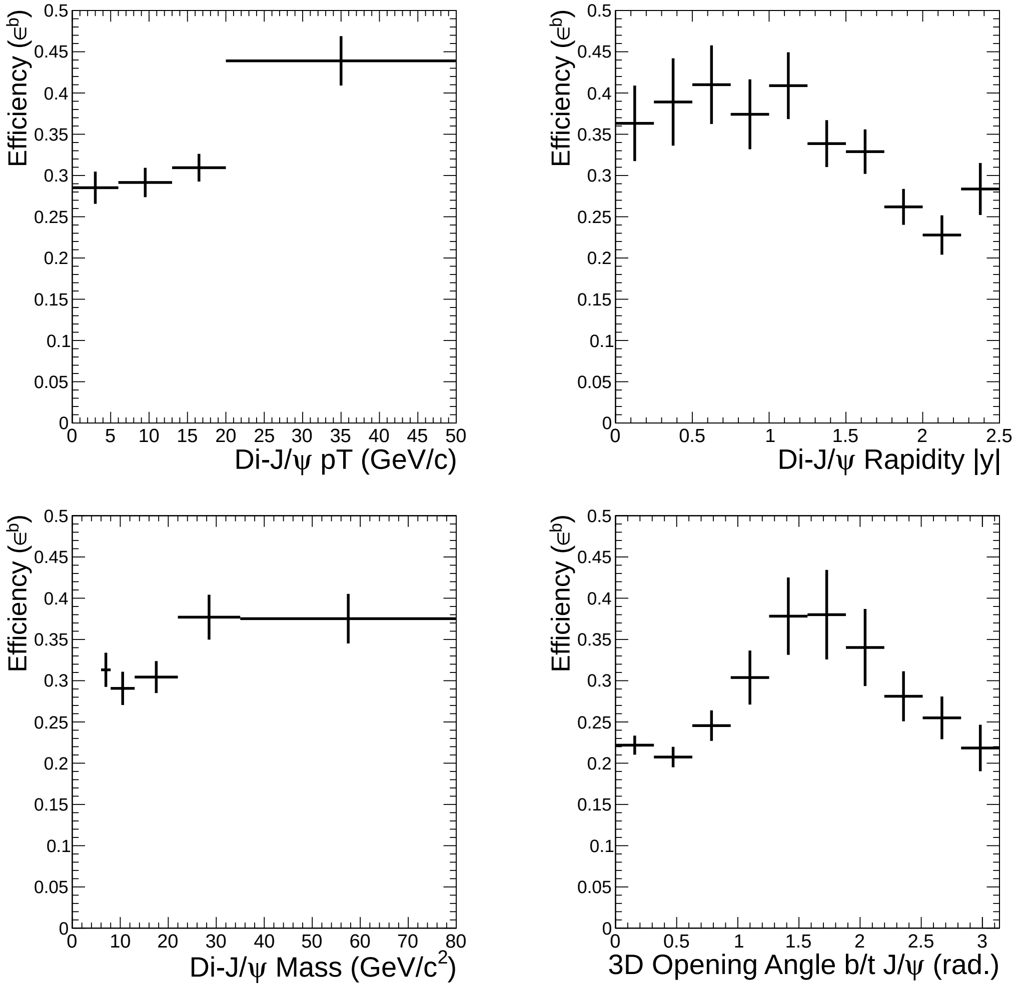

Figure 5.10: ϵ_{b} in bins of the double J/ψ system's transverse momentum, rapidity, invariant mass, and the 3D opening angle between the two J/ψ mesons.

The scaling factor S is calculated as the ratio of the forward and backward efficiencies, $S = \frac{\epsilon_\mathrm{f}}{\epsilon_\mathrm{b}}$, in bins of the kinematic variables x for the SPS and DPS MC samples. Table 5.7 displays the calculated ϵ_f, ϵ_b, and S from SPS and DPS simulation in bins of the double J/ψ invariant mass, M_JJ. Table 5.8 shows the comparison in bins of absolute separation in rapidity, $|\Delta y|$, between the J/ψ. Table 5.9 shows the comparison in bins of double J/ψ transverse momentum, p_T^JJ. The final event-based efficiency values used to determine total or differential cross section in data are calculated using the average scaling factor from SPS and DPS MC:

$$\epsilon_i^{Data} = \bar{S} \cdot \frac{n_{\mathrm{reco},i}}{n_{\mathrm{gen},i}} \tag{5.5}$$

where $\bar{S} = 0.5 \cdot (S^\mathrm{SPS} + S^\mathrm{DPS})$. The fluctuation between S^SPS and S^DPS is used to calculate the uncertainty in the scaling factor:

$$Error = \pm \frac{|S^\mathrm{SPS} - S^\mathrm{DPS}|}{S^\mathrm{SPS} + S^\mathrm{DPS}} \tag{5.6}$$

Table 5.7: Average efficiency (as %) for events in the J/ψ and muon acceptance region for signal events in SPS and DPS MC, determined using the fraction of generated events within the acceptance that were reconstructed, ϵ_f, the average efficiency calculated using repeated substitution of events that passed the selection criteria, ϵ_b, and the scaling factor from the two values, S, in bins of double J/ψ invariant mass, M_JJ. Error shown is due to the number of generated events and, in the case of ϵ_b, due to the statistical uncertainty of the number of events found back from the substitution method, $n_{\mathrm{reco},i}$.

M_JJ (GeV/c^2)	6-8	8-13	13-22	22-35	35-80	Total
SPS ϵ_f	2.2±0.7	4.7±0.2	14.0±0.3	32.9±1.1	47.5±4.9	13.2±0.2
SPS ϵ_b	2.5±0.3	8.5±0.3	17.8±0.3	39.6±0.4	59.0±0.5	18.1±0.3
S^SPS	0.898	0.548	0.790	0.829	0.805	0.731
DPS ϵ_f	6.3±0.6	8.1±0.4	12.8±0.4	12.6±0.5	11.0±0.4	10.9±0.2
DPS ϵ_b	13.4±0.4	10.1±0.8	16.2±1.3	18.9±0.4	15.1±0.7	15.0±0.5
S^DPS	0.469	0.801	0.787	0.670	0.726	0.728

Table 5.8: Average efficiency (as %) for events in the J/ψ and muon acceptance region for signal events in SPS and DPS MC, determined using the fraction of generated events within the acceptance that were reconstructed, ϵ_f, the average efficiency calculated using repeated substitution of events that passed the selection criteria, ϵ_b, and the scaling factor from the two values, S, in bins of absolute separation in rapidity, $|\Delta y|$, between the J/ψ. Error shown is due to the number of generated events and, in the case of ϵ_b, due to the statistical uncertainty of the number of events found back from the substitution method, $n_{\mathrm{reco},i}$.

$\lvert\Delta y\rvert$	0-0.3	0.3-0.6	0.6-1	1-1.6	1.6-2.6	2.6-4.4	Total
SPS ϵ_f	10.9±0.3	12.2±0.4	15.4±0.6	19.4±0.8	20.3±1.7	23.1±9.4	13.2±0.2
SPS ϵ_b	14.5±0.5	18.2±0.4	20.4±0.5	27.9±0.7	24.9±1.2	31.5±0.7	18.1±0.3
S^SPS	0.756	0.672	0.755	0.695	0.816	0.733	0.731
DPS ϵ_f	8.7±0.4	9.5±0.5	13.8±0.7	14.4±0.8	14.9±0.6	9.3±0.3	10.9±0.2
DPS ϵ_b	13.0±0.8	14.5±1.2	16.5±0.4	19.0±1.9	18.1±1.7	13.2±0.5	15.0±0.5
S^DPS	0.665	0.657	0.837	0.760	0.824	0.707	0.728

Table 5.9: Average efficiency (as %) for events in the J/ψ and muon acceptance region for signal events in SPS and DPS MC, determined using the fraction of generated events within the acceptance that were reconstructed, ϵ_f, the average efficiency calculated using repeated substitution of events that passed the selection criteria, ϵ_b, and the scaling factor from the two values, S, in bins of double J/ψ transverse momentum, p_T^JJ. Error shown is due to the number of generated events and, in the case of ϵ_b, due to the statistical uncertainty of the number of events found back from the substitution method, $n_{\mathrm{reco},i}$.

p_T^JJ (GeV/c)	0-5	5-10	10-14	14-18	18-23	23-40	Total
SPS ϵ_f	11.8±0.3	12.3±0.3	16.3±0.7	27.3±1.9	38.7±5.6	45.5±14.4	13.2±0.2
SPS ϵ_b	17.4±0.3	16.1±0.5	21.3±0.5	35.3±0.4	50.1±0.4	57.2±1.0	18.1±0.3
S^SPS	0.683	0.763	0.766	0.773	0.773	0.795	0.731
DPS ϵ_f	7.7±0.3	9.1±0.3	9.6±0.3	16.6±0.7	24.5±1.5	34.0±3.6	10.9±0.2
DPS ϵ_b	11.4±0.5	13.7±0.4	12.1±1.0	21.7±0.7	32.7±0.6	43.8±0.4	15.0±0.5
S^DPS	0.675	0.672	0.803	0.770	0.750	0.776	0.728

5.6 Fitting Procedure

An extended maximum likelihood fit to data is performed in order to extract signal weights using the sPlot technique Pivk and Le Diberder (2005). Four kinematic variables are selected to discriminate the double J/ψ signal from residual background in our sample:

- $\mu^+\mu^-$ invariant mass $M^1_{\mu\mu}$ of the high-p_{T} J/ψ;
- $\mu^+\mu^-$ invariant mass $M^2_{\mu\mu}$ of the low-p_{T} J/ψ;
- proper decay length ct^{J/ψ_1} of the high-p_{T} J/ψ;
- separation significance $d^{\mathrm{J}/\psi}$ between the two J/ψ candidates.

Four categories of events are defined: the double prompt J/ψ signal; non-prompt J/ψ; prompt J/ψ plus unassociated muon tracks; pure combinatorial background.

The likelihood for event j is obtained by summing the product of yields n_i and probability density functions (PDFs) $P_i(M^1_{\mu\mu}), Q_i(M^2_{\mu\mu}), R_i(ct^{\mathrm{J}/\psi_1}), S_i(d^{\mathrm{J}/\psi})$ with shape parameters for each of the signal and background hypotheses i. The extended likelihood function is the product of likelihoods for each event j:

$$\begin{aligned}
\mathcal{L}_j &= n_{\mathrm{sig}}\left[P_1(M^1_{\mu\mu}) * Q_1(M^2_{\mu\mu}) * R_1(ct^{\mathrm{J}/\psi_1}) * S_1(d^{\mathrm{J}/\psi})\right] && (5.7)\\
&+ n_{non-prompt}\left[P_2(M^1_{\mu\mu}) * Q_2(M^2_{\mu\mu}) * R_2(ct^{\mathrm{J}/\psi_1}) * S_2(d^{\mathrm{J}/\psi})\right] && (5.8)\\
&+ n_{\mathrm{J}/\psi-bkg+bkg-\mathrm{J}/\psi}\left[f * P_3(M^1_{\mu\mu}) * Q_3(M^2_{\mu\mu}) * R_3(ct^{\mathrm{J}/\psi_1})_{\mathrm{J}/\psi-bkg} * S_3(d^{\mathrm{J}/\psi})_{\mathrm{J}/\psi-bkg}\right] && (5.9)\\
&+ n_{\mathrm{J}/\psi-bkg+bkg-\mathrm{J}/\psi}\left[(1-f) * P_4(M^2_{\mu\mu}) * Q_4(M^1_{\mu\mu}) * R_4(ct^{\mathrm{J}/\psi_1})_{bkg-\mathrm{J}/\psi} * S_4(d^{\mathrm{J}/\psi})_{bkg-\mathrm{J}/\psi}\right] && (5.10)\\
&+ n_{bkg-bkg}\left[Q_4(M^1_{\mu\mu}) * Q_3(M^2_{\mu\mu}) * R_5(ct^{\mathrm{J}/\psi_1}) * S_5(d^{\mathrm{J}/\psi})\right] && (5.11)\\
& && (5.12)
\end{aligned}$$

The yields n_i are determined by minimizing the quantity $-\ln\mathcal{L}$ Verkerke and Kirkby (2003). To maintain minimal model dependence, shapes and parameters of probability density functions for combinatorial background categories are extracted from sidebands in data. MC is used to parameterize the prompt and non-prompt J/ψ distributions. Both the DPS and SPS MC are used for the signal category; the distributions of the four event variables agree between these samples, as Fig. 5.11 demonstrates.

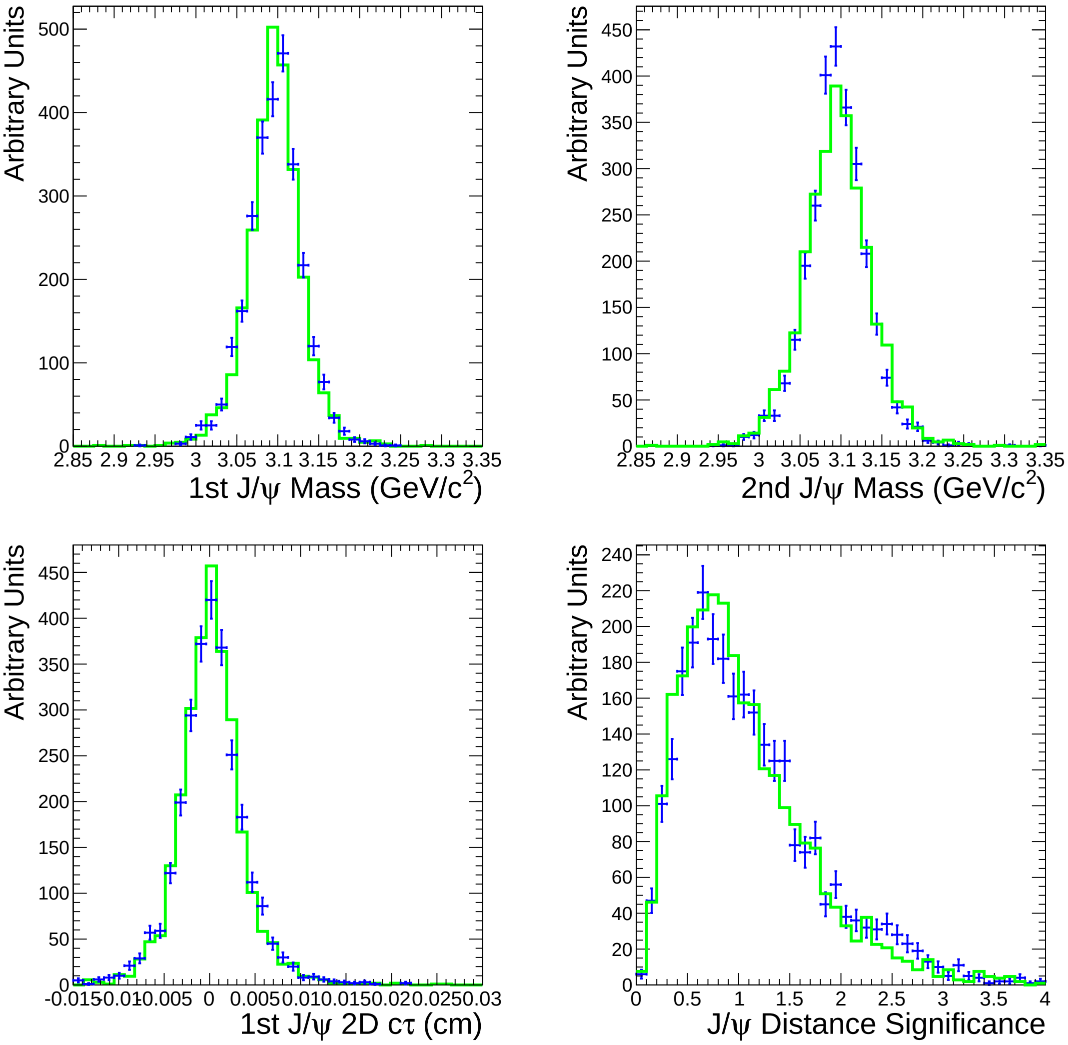

Figure 5.11: Fit variable distributions shown for SPS (in blue) and DPS (in green) simulation. Only candidates passing the full event selection are shown, J/ψ are sorted by p_{T}, and error bars are based on statistics.

The linear correlation coefficients between the event variables are derived from DPS MC in Table 5.10. With the exception of the mass and ct for the high-p_{T} J/ψ, which has a correlation coefficient in MC of 13%, most variables were uncorrelated and had coefficients below 5%.

Table 5.10: Correlation coefficients of the variables selected for the ML analysis reconstructed in DPS signal MC.

Variable	J/ψ_1 Mass	J/ψ_2 Mass	ct^{J/ψ_1}	Distance Significance
J/ψ_1 Mass	1.00			
J/ψ_2 Mass	0.01	1.00		
ct^{J/ψ_1}	0.13	0.03	1.00	
Distance Significance	0.01	0.02	0.05	1.00

5.6.1 Probability Density Functions

Several parameterizations are tried for our variables. The guiding principle in designing the PDFs is to use the simplest function with the least number of parameters necessary to adequately describe the observed distribution of events. For parameterizations that result in equally good descriptions of the data (as measured by the χ^2 in variable projections), the difference in yields is used as a measure of systematic uncertainty. The DPS simulation was used to extract signal PDF shapes for the primary fit, but PDFs extracted from SPS simulation were used in an alternate fit for comparison, and the resulting difference in signal yield taken as uncertainty due to model dependence of the fit. This uncertainty was found to be 0.1%.

Tables 5.11, 5.12, and 5.13 list the functional forms used to define the PDFs. Systematic uncertainties on yields are determined due to our (potentially) incomplete knowledge of the true distributions conservatively with alternative parameterizations (see Section 5.9).

Mass Distributions

The sum of two Gaussians with a common mean is used to parametrize the signal J/ψ mass shapes (see Fig. 5.12); the same parameters are used to describe the non-prompt component and the J/ψ part of the J/ψ-combinatorial and combinatorial-J/ψ components. The widths of the double Gaussian are fixed to the best fit to DPS simulation, but the mean is free to float in the fit to data. A Crystal Ball function convolved with a single Gaussian was also tried and compared to a double Gaussian to describe the J/ψ mass distribution, resulting in only a 0.2% difference in signal yield and similar fit convergence. Insufficient statistics to characterize the tail of the J/ψ mass distribution as well as similar fit results led to the selection of the double Gaussian as the least parameterized PDF in the primary fit. Third-order Chebyshev polynomial functions are used to describe the purely combinatorial components (see Fig. 5.16). The extraction of the combinatorial PDFs is done with a data-driven method described in detail in Section 5.6.2.

ct

A double Gaussian resolution function is used for the signal *ct* PDF shapes and shown in Fig. 5.13. The non-prompt background component is fit by an exponential function convolved with a single Gaussian resolution function, shown in Fig. 5.15). A different double Gaussian resolution function is used to describe each of the combinatorial background components and is extracted from the $\mu^+\mu^-$ invariant mass sidebands from data (see Figures 5.17, 5.18, and 5.19). The PDF parameters for each of the components are determined from the best fit to their respective samples with the exception of the lifetime parameter of the non-prompt component, which is left free to float in the final fit to data.

Table 5.11: Summary of the functional forms for the $M_{J/\psi}$ distributions in the sample components. The widths for the double Gaussians are fixed from signal MC, but the mean is left free to float in the final fit. $\{\mu,\sigma\}$ are the {mean, standard deviation} for a Gaussian, a_i are constants.

Component	PDF M_{J/ψ_1}	PDF M_{J/ψ_2}	Parameters
Signal	2G	2G	$\mu^i, \sigma_1^i, \sigma_2^i, f^i\ (i = 1, 2)$
Non-prompt background	2G	2G	$\mu^i, \sigma_1^i, \sigma_2^i, f^i\ (i = 1, 2)$
J/ψ-bkg	2G	Pol3	$\mu^1, \sigma_1^1, \sigma_2^1, a_0^2, a_1^2, a_2^2, f$
bkg-J/ψ	Pol3	2G	$a_0^1, a_1^1, a_2^1, \mu^2, \sigma_1^2, \sigma_2^2, (1 - f)$
bkg-bkg	Pol3	Pol3	$a_0^i, a_1^i, a_2^i\ (i = 1, 2)$

Significance of the Distance Between Two J/ψ Candidates

For signal and non-prompt samples, the significance of the distance, $d^{J/\psi}$, between two J/ψ candidates has been parametrized with a single Gaussian resolution function convolved with an exponential function for the signal and non-prompt components, as shown by Fig. 5.13 and Fig. 5.18) respectively. The $d^{J/\psi}$ for J/ψ-combinatorial backgrounds is parameterized by a Landau function plus a first degree Chebyshev polynomial, shown in Figures 5.17, 5.17, 5.18, 5.17, and 5.19. For estimating the systematic uncertainty due to the incomplete knowledge of this variable distribution, the effect of using a single Gaussian convolved with an exponential is also tested for all components and finds only a 0.6% variation in resulting signal yield.

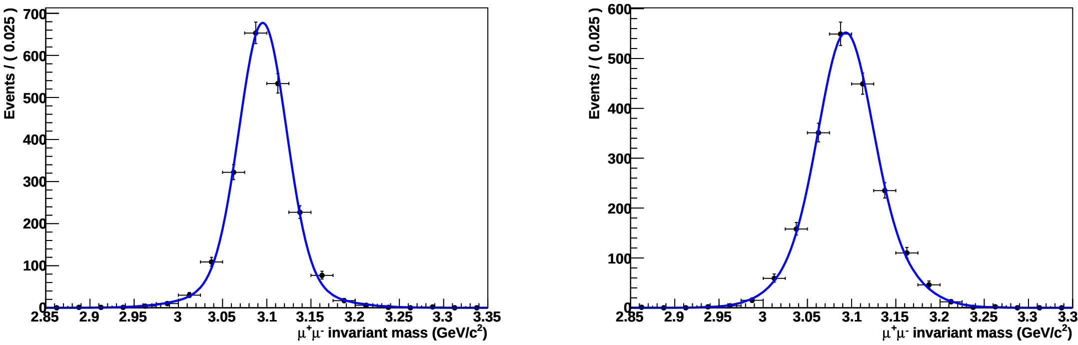

Figure 5.12: Fits to determine PDF parameters for M_{J/ψ_1} (left) and M_{J/ψ_2} (right) in DPS signal MC.

Table 5.12: The ct PDFs used in the fit. The signal ct resolution function is defined as the sum of two Gaussians, one for the core and one for the tail. For the non-prompt background components, the ct resolution function is defined as a single Gaussian function. For the combinatorial components, the resolution functions are defined as the sum of two Gaussians. All the resolution functions are different and extracted from MC (for signal and non-prompt components) and the J/ψ sidebands on data (for the remaining). By definition $\lambda = c\tau$.

Component	PDF $ct_{xy}^{\mathrm{J}/\psi_1}$	Parameters
Signal	$2G$	$\mu_1^1, \sigma_1^1, \mu_2^1, \sigma_2^1, f$
Non-prompt background	$G \otimes e^{-ct/\lambda_1}$	$\mu^1, \sigma^1, \lambda^1$
J/ψ-bkg	$2G$	$\mu_1^1, \sigma_1^1, \mu_2^1, \sigma_2^1, f$
bkg-J/ψ	$2G$	$\mu_1^1, \sigma_1^1, \mu_2^1, \sigma_2^1, f$
bkg-bkg	$2G$	$\mu_1^1, \sigma_1^1, \mu_2^1, \sigma_2^1, f$

Table 5.13: Summary of the functional forms for the $d^{\mathrm{J}/\psi}$ distributions in the sample components. Only the signal and non-prompt shapes have been fixed from MC. $\{\mu,\sigma\}$ are the {mean, standard deviation} for a Gaussian, λ_i are the lifetime constants.

Component	PDF $d^{\mathrm{J}/\psi}$	Parameters
Signal	$G \otimes e^{-ct/\lambda_1}$	$\mu_1, \sigma_1, \lambda_1$
Non-prompt background	$G \otimes e^{-ct/\lambda_2}$	$\mu_2, \sigma_2, \lambda_2$
J/ψ-bkg	$L \oplus Pol2$	a_0, a_1, f, μ, σ
bkg-J/ψ	$L \oplus Pol2$	a_0, a_1, f, μ, σ
bkg-bkg	$L \oplus Pol2$	a_0, a_1, f, μ, σ

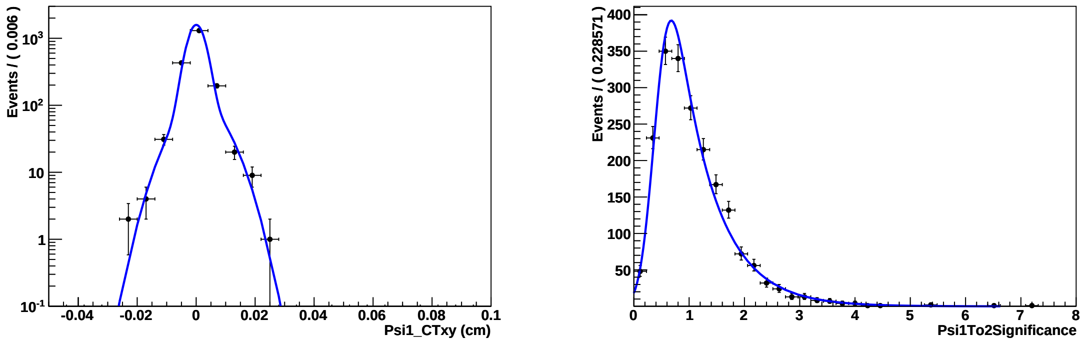

Figure 5.13: Fits to determine PDF parameters for the $ct_{xy}^{\mathrm{J}/\psi_1}$ (left) and significance of the distance between the two J/ψ candidates (right) in DPS signal MC.

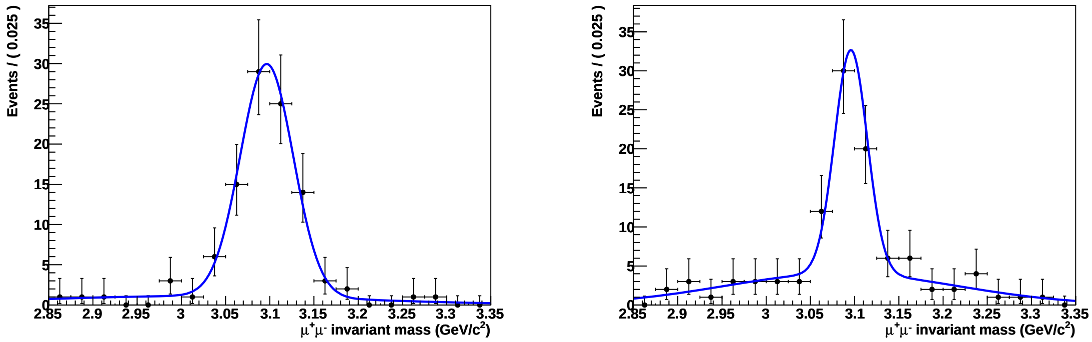

Figure 5.14: Fits to determine PDF parameters for M_{J/ψ_1} (left) and M_{J/ψ_2} (right) in the non-prompt sample (a cocktail of B-background MC). These shapes are assumed to be signal-like and, therefore, obtained by DPS signal MC events.

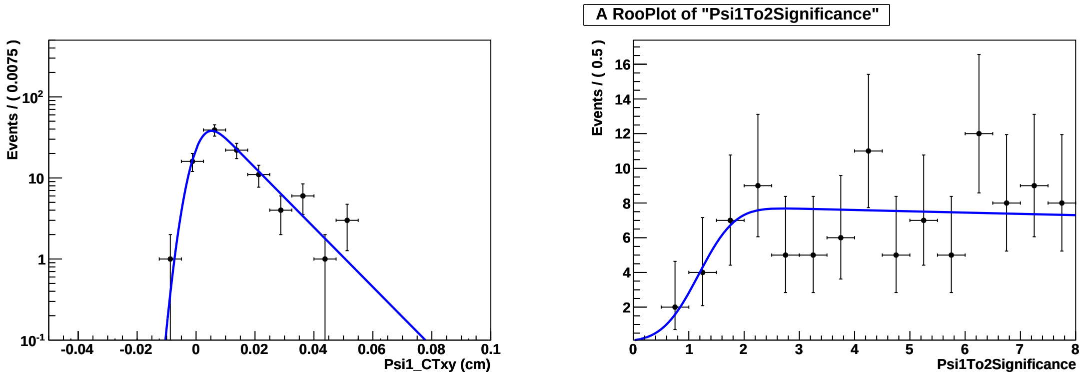

Figure 5.15: Fits to determine PDF parameters for the $ct_{xy}^{\mathrm{J}/\psi_1}$ (left) and significance of the distance between the two J/ψ candidates (right) in the non-prompt sample (a cocktail of B-background MC).

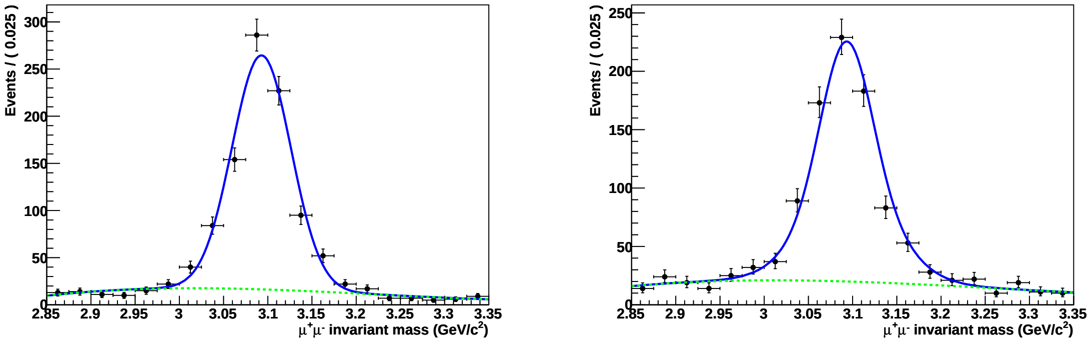

Figure 5.16: Fits to determine PDF parameters for the combinatorial components of M_{J/ψ_1} (left) and M_{J/ψ_2} (right), shown by the green dotted line. The explanation of the method is given in Section 5.6.2.

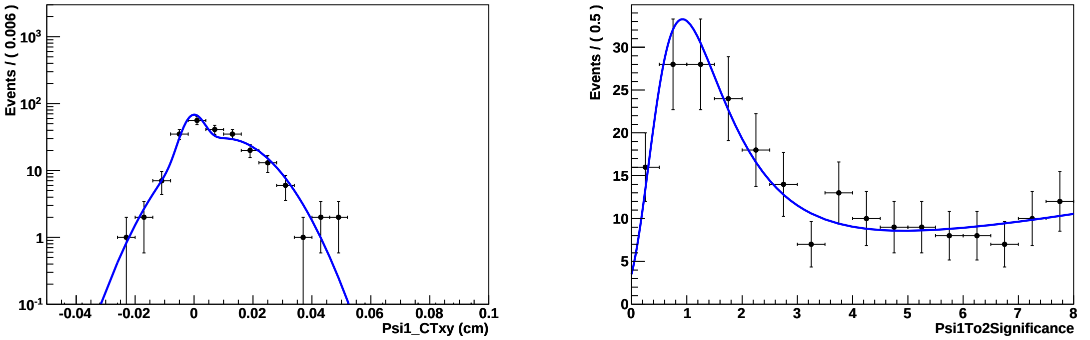

Figure 5.17: Fits to determine PDF parameters for $ct_{xy}^{\mathrm{J}/\psi_1}$ (left) and the significance of the distance (right) between the two J/ψ candidates from the sidebands extracted from data for the J/ψ-combinatorial component. The explanation of the method is given in Section 5.6.2.

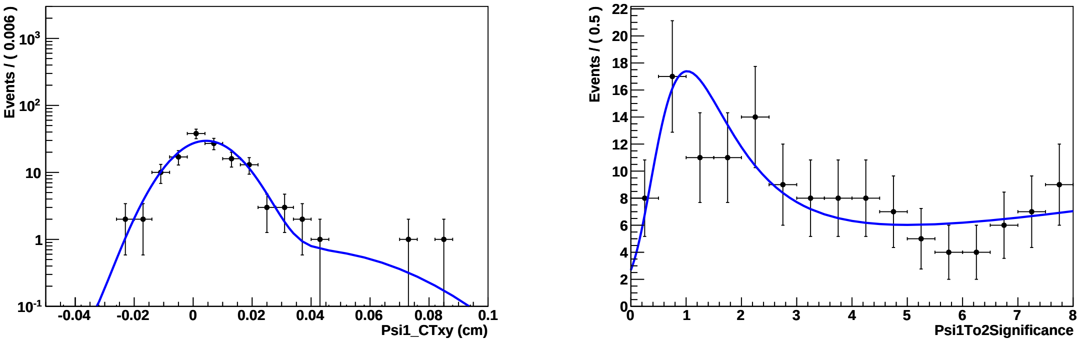

Figure 5.18: Fits to determine PDF parameters for $ct_{xy}^{\mathrm{J}/\psi_1}$ (left) and the significance of the distance (right) between the two J/ψ candidates from the sidebands extracted from data for the combinatorial-J/ψ component. The explanation of the method is given in Section 5.6.2.

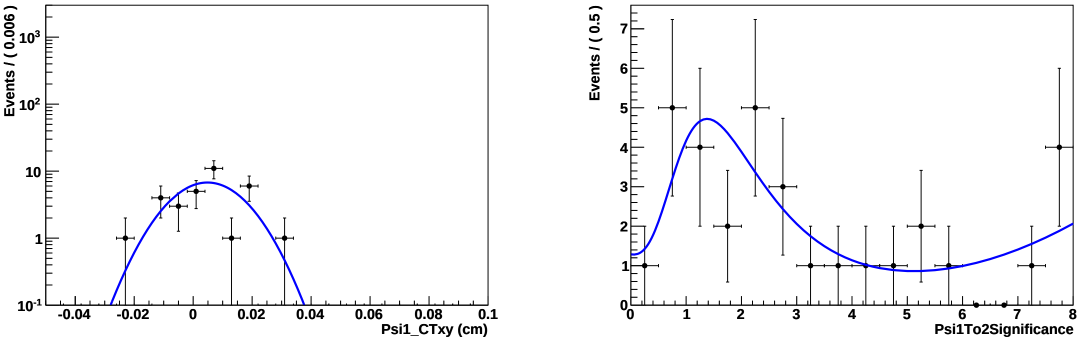

Figure 5.19: Fits to determine PDF parameters for $ct_{xy}^{\mathrm{J}/\psi_1}$ (left) and the significance of the distance between the two J/ψ candidates (right) from both sidebands extracted from data for the combinatorial-combinatorial component. The explanation of the method is given in Section 5.6.2.

5.6.2 Data-driven Procedure to Determine PDF Parameters for the Combinatorial Background

Background shapes are obtained directly from data, relying on the assumption that in the $M_{\mathrm{J}/\psi}$ sidebands there are only contributions from the combination of true J/ψ candidates and combinatorial background. The two $M_{\mathrm{J}/\psi}$ sideband regions have been defined between $[2.85, 3.00]$ and $[3.20, 3.35]$ GeV/c^2, as shown in Fig. 5.20. The $\mu\mu$ invariant mass parameters, resolution functions, and the significance of the J/ψ distance parameters are extracted from the sidebands to describe the combinatorial background components.

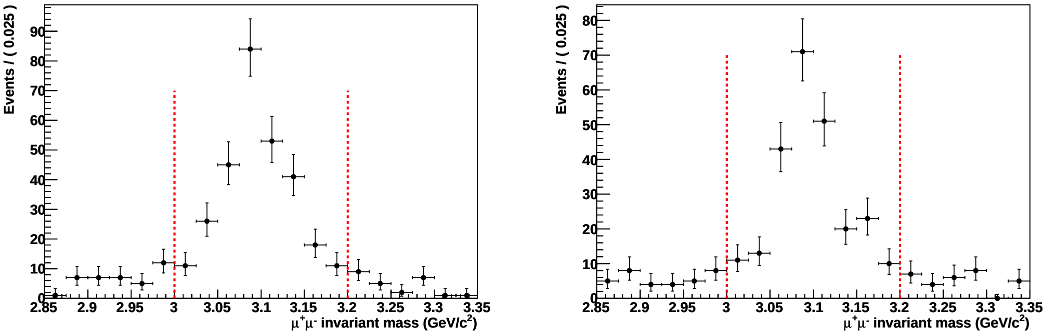

Figure 5.20: Plot of the two $\mu^+\mu^-$ invariant masses as obtained from data. The sidebands are delimited by the two red dashed lines.

The fit proceeds in steps. Three distinct categories (J/ψ-combinatorial, combinatorial-J/ψ, and combinatorial-combinatorial) are separated and parameterized with the following criteria:

– The mass distributions in data are assumed to be fully described by a prompt J/ψ shape (parameterized by a double Gaussian) added to a combinatorial component (parameterized by a third order Chebyshev polynomial). The parameters for the double Gaussian are fixed to the fit of signal MC while the polynomial parameters are left free to float and extracted from a fit to the J/ψ_1 and J/ψ_2 mass distributions from data. These polynomials are used to parameterize the respective combinatorial $\mu^+\mu^-$ invariant mass in each of the three combinatorial components.

– For the J/ψ-combinatorial component, events are selected that populate the sidebands of the second $\mu^+\mu^-$ invariant mass. For this region, the parameters are obtained to describe the J/ψ_1 proper decay length and the significance of the distance between the two J/ψ mesons from the best fit to the distribution.

– The above procedure is repeated for the combinatorial-J/ψ component by selecting events that populate the sidebands of the first J/ψ and fitting the J/ψ_1 proper decay length and $d^{\mathrm{J}/\psi}$ distributions. The relative ratio of J/ψ-combinatorial to combinatorial-J/ψ cases is left free to float in the final fit.

– The parameters describing the J/ψ_1 proper decay length and the significance of the distance between the J/ψ for the combinatorial-combinatorial component are extracted from a fit to events that populate the sidebands of both J/ψ at the same time.

5.7 The Maximum Likelihood Fit

5.7.1 The 4D Fit to Data

The fit to the full data sample is presented below. Table 5.14 lists the numerical results while Figure 5.21 shows the breakdown within the fit variables. In the fits the mean value of the central Gaussian functions of the two $\mu^+\mu^-$ invariant masses are left free to float. The fit converges with a negative log likelihood of -10781.1.

Table 5.14: Summary of signal and background yields determined by fitting simultaneously M_{J/ψ^1}, M_{J/ψ^2}, $ct_{xy}^{\mathrm{J}/\psi_1}$, and $d^{\mathrm{J}/\psi}$ for 1043 selected candidate events.

Parameter	Yield
N_{sig}	446 ± 23
$N_{\mathrm{non-prompt}}$	182 ± 18
$N_{\mathrm{J}/\psi-\mathrm{bkg}+\mathrm{bkg}-\mathrm{J}/\psi}$	321 ± 28
$N_{\mathrm{bkg-bkg}}$	94 ± 16

The fit produces signal weights for each selected event using the sPlot technique Pivk and Le Diberder (2005).

5.7.2 Fit Validation

The fit is validated by repeatedly generating simulated samples from the probability density functions for all components. 10,000 such toy experiments are performed to reproduce the likelihood value; the signal yield pull distribution is consistent with zero and the width consistent with 1. The distributions of these experiments for the 1043 candidate data events are listed in Fig. 5.22.

Potential bias due to residual correlation between the variables in signal events is tested by embedding signal and background MC events in the data sample. Since this would tend to magnify any correlations, the results are considered to be a conservative upper limit on potential bias due to correlations between the fit variables. In the first test, 103 non-prompt MC events are added to the dataset and the fit performed on the

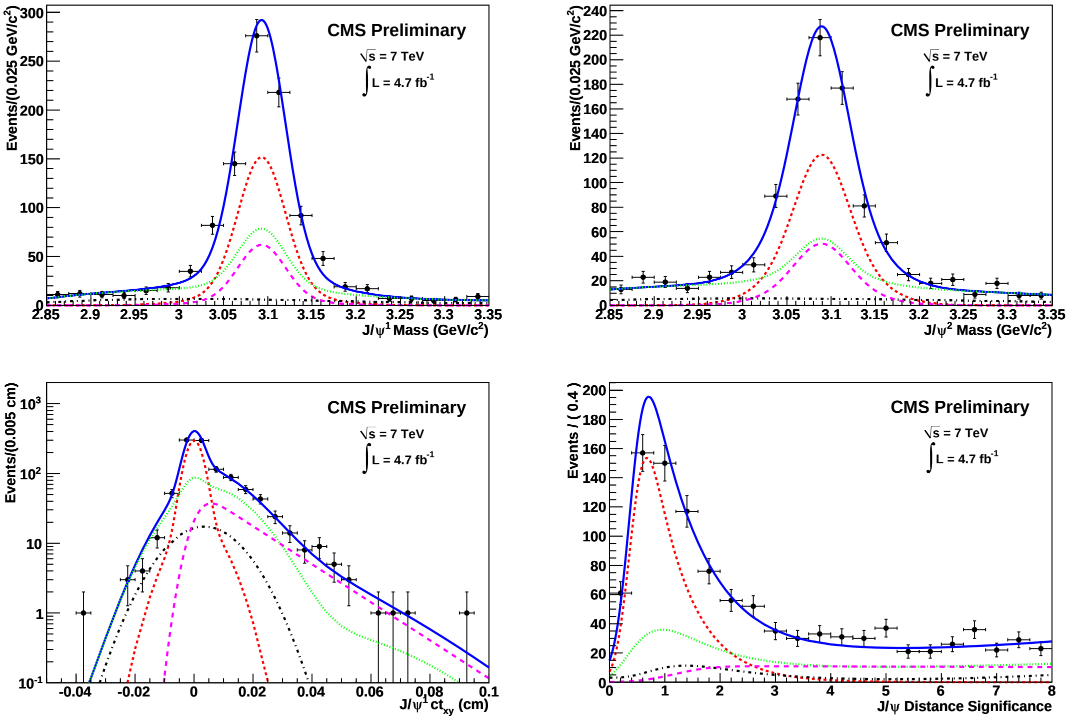

Figure 5.21: Projections of the fit results in M_{J/ψ^1} (top left), M_{J/ψ^2} (top right), $ct_{xy}^{\mathrm{J}/\psi_1}$ (bottom left), and distance significance (bottom right) for 1043 candidate events. Individual contributions from the various components are shown in different colors: signal (dashed red), B background (dashed purple), all combinatorial contributions (dashed green), and the combinatorial-combinatorial only (dashed black).

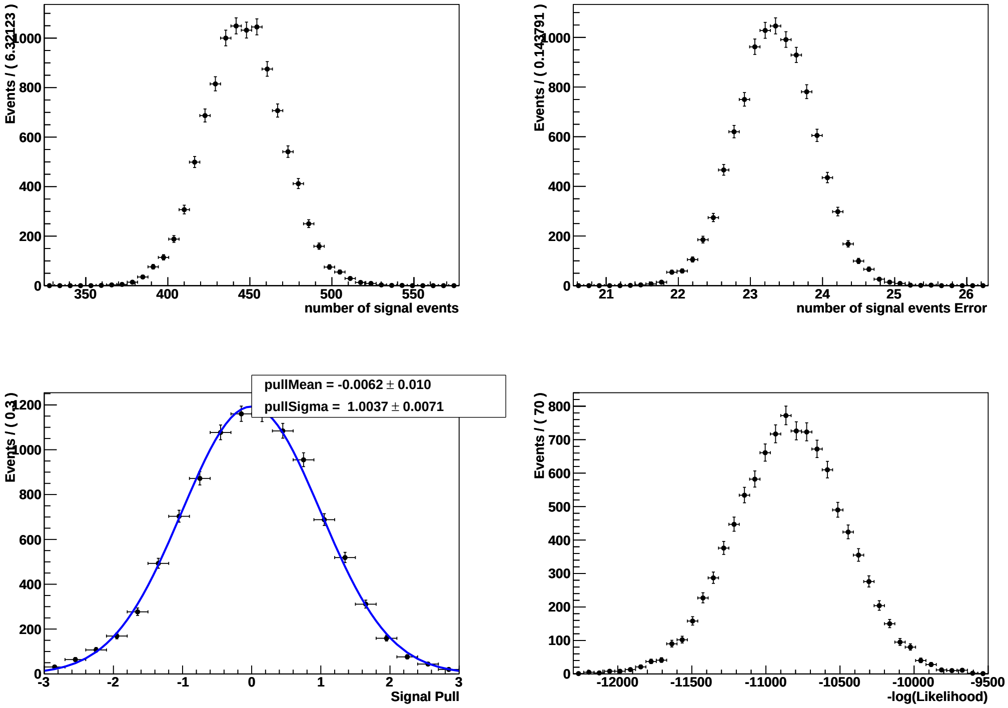

Figure 5.22: Top: The signal yield distribution (left) and statistical uncertainty (right) on signal yield for 10,000 toy experiments simulating the 4D final fit. Bottom: The corresponding pull distribution of the signal yield (left) and the likelihood distribution (right) from the 10,000 experiments.

new background-enhanced sample. In the second one, 400 SPS signal MC events are added to the dataset and the sample refit. In the third one, 200 DPS signal MC events are added to the dataset and the sample refit. For the fourth one, a combination of both 400 SPS and 200 DPS signal MC events were added to the dataset and the sample refit. For the last test, a mixed sample of 400 SPS signal MC events, 200 DPS signal MC events, and 103 background MC events was added to data. The yields from these fits are listed in Tables 5.15, 5.16, 5.17, 5.18, and 5.19. The fitted signal yields are consistent with expectation from the input values and primary fit results (described in Section 5.7.1). The signal yield is well reproduced, independent of the yields in the background components.

Table 5.15: Summary of signal and background yields after adding 103 background events from the non-prompt MC sample to the sample of 1043 events.

Parameter	Yield
N_{sig}	443 ± 24
$N_{\mathrm{non-prompt}}$	250 ± 20
$N_{\mathrm{J/\psi-bkg+bkg-J/\psi}}$	357 ± 29
$N_{\mathrm{bkg-bkg}}$	96 ± 16

Table 5.16: Summary of signal and background yields determined after adding 400 SPS signal MC events to the sample of 1043 events.

Parameter	Yield
N_{sig}	840 ± 31
$N_{\mathrm{non-prompt}}$	187 ± 18
$N_{\mathrm{J/\psi-bkg+bkg-J/\psi}}$	321 ± 28
$N_{\mathrm{bkg-bkg}}$	94 ± 31

Table 5.17: Summary of signal and background yields determined after adding 200 DPS signal MC events to the sample of 1043 events.

Parameter	Yield
N_{sig}	645 ± 28
$N_{\mathrm{non-prompt}}$	183 ± 18
$N_{\mathrm{J/\psi-bkg+bkg-J/\psi}}$	320 ± 28
$N_{\mathrm{bkg-bkg}}$	94 ± 16

Table 5.18: Summary of signal and background yields determined after adding 400 SPS and 200 DPS signal MC events to the sample of 1043 events.

Parameter	Yield
N_{sig}	1039 ± 34
$N_{\mathrm{non-prompt}}$	188 ± 19
$N_{\mathrm{J/\psi-bkg+bkg-J/\psi}}$	321 ± 28
$N_{\mathrm{bkg-bkg}}$	94 ± 16

Table 5.19: Summary of signal and background yields determined after adding 400 SPS and 200 DPS signal MC events, as well as 103 non-prompt MC events to the sample of 1043 events.

Parameter	Yield
N_{sig}	1034 ± 34
$N_{\mathrm{non-prompt}}$	259 ± 29
$N_{\mathrm{J/\psi-bkg+bkg-J/\psi}}$	358 ± 29
$N_{\mathrm{bkg-bkg}}$	96 ± 16

5.8 Results from Sub-Samples

To ensure that the cross section determination was insensitive to changing conditions, the stability of the variables used in the likelihood fit are compared with different amounts of pileup and for each of the two major 2011 run periods. Event variable distributions in low pileup events (defined as containing six reconstructed primary vertices or less) are compared to distributions in high pilup events (more than six primary vertices). The distributions are also compared between the two major 2011 run periods. As a cross-check, the 1043 event sample is also split into three equal sized consecutive samples and refit.

5.8.1 Effects of Run Conditions

The effect of run conditions on the shape of variables selected for the likelihood fit is measured. Figure 5.23 shows selected variables in a low pileup event (defined as containing six reconstructed primary vertices or less) compared to a high pileup event (more than six primary vertices). The high pileup case (in blue) is scaled by statistics relative to the low pileup case since only the shape is being compared. The high and low pileup cases are in agreement within the limits of the statistical error.

Figure 5.24 shows selected variables based on events during the Run 2011A data-taking period compared to the Run 2011B data-taking period. The Run 2011B case (in blue) is scaled by statistics relative to the Run 2011A case since only the shape is being compared. Run conditions such as collision rate and accrued radiation damage changed during the run periods, but these effects did not significantly impact the selected variables.

5.8.2 Results from Separate Fits in Mass Bins

As a cross-check, the 1043 event sample is refit after splitting it into three similarly signal-populated bins of double J/ψ invariant mass. Figures 5.25, 5.26, and 5.27 show

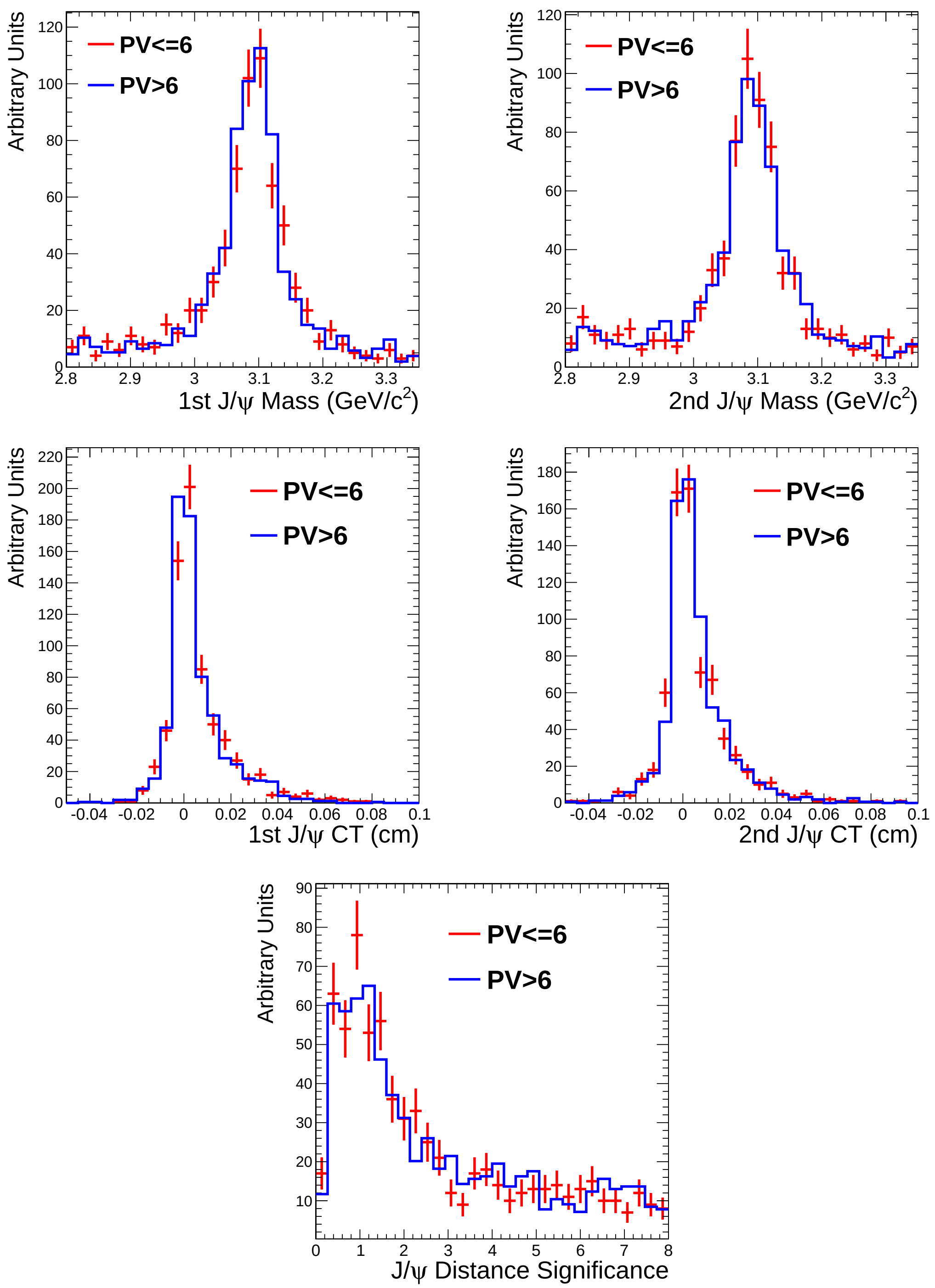

Figure 5.23: Key variables shown under different pileup conditions in the 2011 data-taking. Only candidates passing the full event selection are shown, J/ψ are sorted by p_{T}, and error bars are based on statistics.

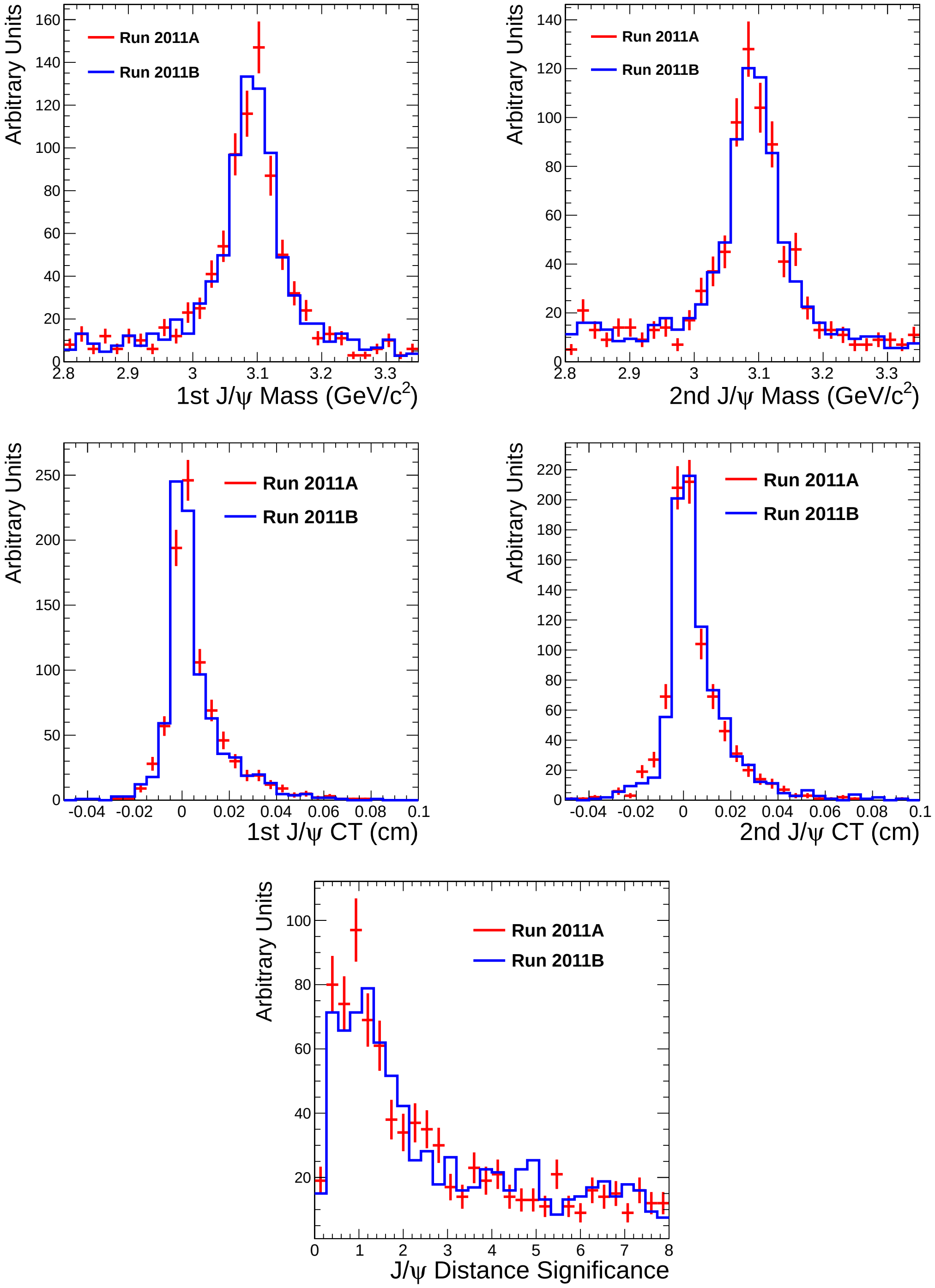

Figure 5.24: Key variables shown based on events in the Run 2011A and Run 2011B data-taking period. Only candidates passing the full event selection are shown, J/ψ are sorted by p_{T}, and error bars are based on statistics.

the distributions for the fit in each of these mass bins. The signal yields of the three new separate fits are compared to the signal-weighted yield of the primary fit in each bin in Table 5.20. The largest difference in signal yield in a single bin is one event.

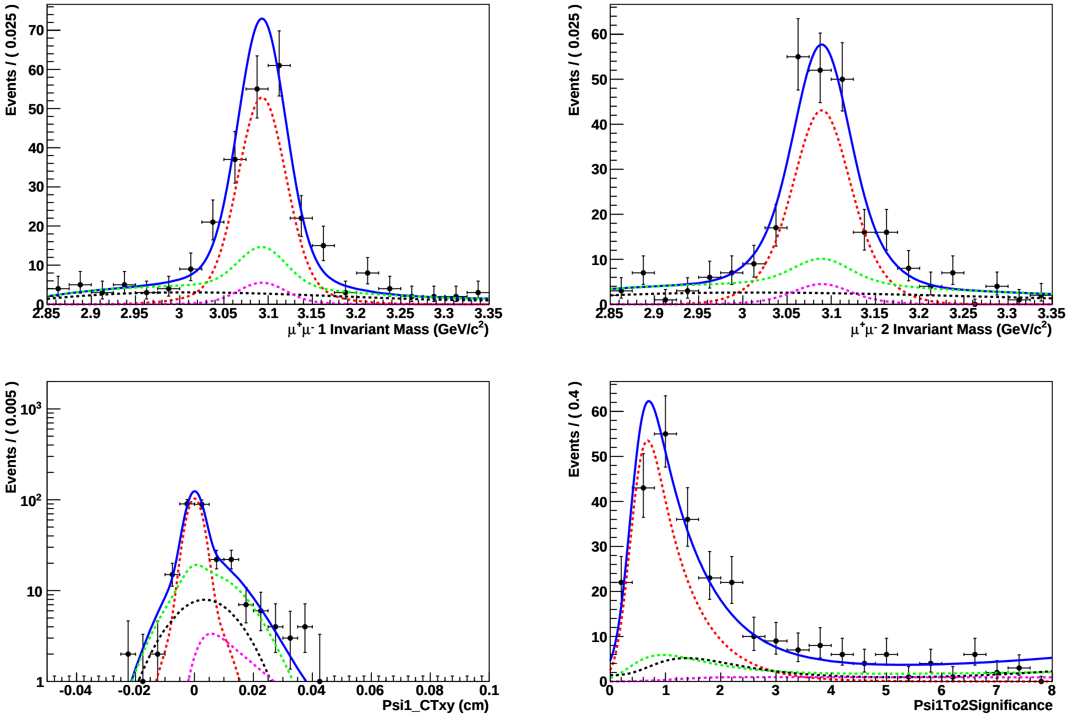

Figure 5.25: Projections of the fit results in M_{J/ψ^1} (top left), M_{J/ψ^2} (top right), ct^{J/ψ_1} (bottom left), and distance significance (bottom right) for the mass range range $6-8.7$ (GeV/c^2). Individual contributions from the various components are shown in different colors: signal (dashed red), B background (dashed purple), J/ψ-combinatorial and viceversa (dashed green), and combinatorial-combinatorial (dashed black).

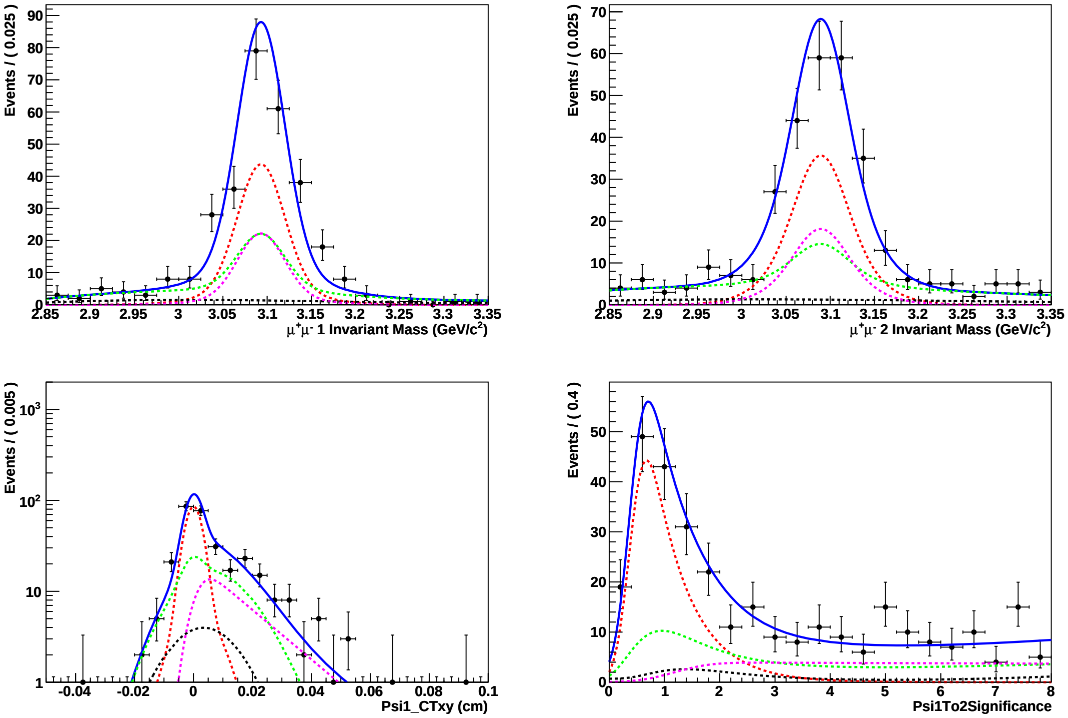

Figure 5.26: Projections of the fit results in M_{J/ψ^1} (top left), M_{J/ψ^2} (top right), ct^{J/ψ_1} (bottom left), and distance significance (bottom right) for the mass range range $8.7 - 17.8$ (GeV/c^2). Individual contributions from the various components are shown in different colors: signal (dashed red), B background (dashed purple), J/ψ-combinatorial and viceversa (dashed green), and combinatorial-combinatorial (dashed black).

Table 5.20: Summary of signal yields after refitting sample in separate M_{JJ} bins (left column) compared to the yields from the primary fit with signal weights applied (right column).

M_{JJ} (GeV/c^2)	Refit Signal Yield	Primary Fit w/ sw
$6 - 8.7$	155 ± 13	154
$8.7 - 17.8$	129 ± 13	129
$17.8 - 80$	160 ± 14	160

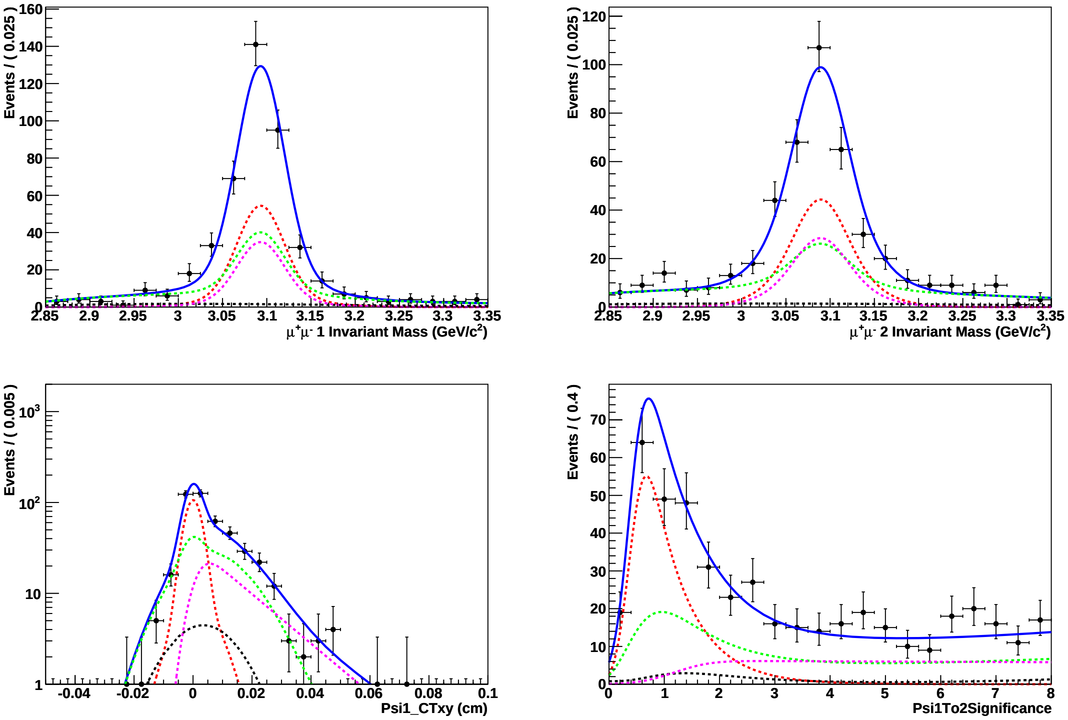

Figure 5.27: Projections of the fit results in M_{J/ψ^1} (top left), M_{J/ψ^2} (top right), ct^{J/ψ_1} (bottom left), and distance significance (bottom right) for the mass range range $17.8 - 80$ (GeV/c^2). Individual contributions from the various components are shown in different colors: signal (dashed red), B background (dashed purple), J/ψ-combinatorial and viceversa (dashed green), and combinatorial-combinatorial (dashed black).

5.9 Systematic Uncertainties

Several sources of systematic uncertainty on the total cross section measurement are considered and the main contributions described here.

- **Branching Fractions** – the uncertainty of the branching fractions for the J/ψ decays are those reported by the Particle Data Group Beringer et al. (2012).

- **Integrated Luminosity** – The systematic uncertainty corresponding to the luminosity normalization is estimated to be about 2.5% CMS (2013).

- **Acceptance Correction** – It is determined on an event-by-event basis. Using simulations with two different production models, SPS and DPS, the closure as described in Section 5.4 is used to estimate the uncertainty of the method: a sample of (N_{J}) simulated events is subjected to the acceptance criteria and then the acceptance correction is applied to arrive at a corrected yield (N'_{J}). The uncertainty for a given production model is taken as half the fractional difference between the two yields, N_{J} and N'_{J}. The relative uncertainty is 1.1% for the SPS sample and 0.1% for the DPS sample. The worst value of the two is quoted.

- **Efficiency Calculation** – The precision of the event-basd efficiency correction is limited by the sample size of the reconstructed events, $N_{reco,i}$, for each event i in data. The cross section is calculated for yields repeatedly generated according to gaussian functions with width $\sqrt{n_{reco,i}}$. The width of the resulting cross section distribution is used as an estimate of the efficiency uncertainty, found to be 4.4% for the data sample.

- **Efficiency Scaling Factor** – The relative scaling factor for the efficiency is determined from SPS and DPS MC samples, representing very different scenarios of double J/ψkinematics. The uncertainty due to model dependence of the scaling factor is defined as the difference in the cross section between any model and their average. The resulting relative uncertainty is found to be 0.2%, demonstrating little model dependence.

- **Muon Tracking** – The muon track reconstruction efficiency is derived from simulated events. The uncertainty due to differences in data versus MC is estimated from tag and probe tables. For each muon in an event the tracking efficiency in data, $\epsilon_{\text{data}}^{\text{track}}$, and simulation, $\epsilon_{\text{sim}}^{\text{track}}$, is obtained from Table 1 of CMS Collaboration (2010) based on the measured pseudo-rapidity. The relative uncertainty is defined as: $|\epsilon_{\text{data}}^{\text{track}} - \epsilon_{\text{sim}}^{\text{track}}|/\epsilon_{\text{data}}^{\text{track}}$. For the event, the individual muon uncertainties are added linearly and signal-weighted. The uncertainty averaged over the events in data is 3.0%.

- **Detector Efficiency** – The efficiency to trigger and reconstruct double J/ψ events relies on detector simulations. The uncertainty due to differences between data and MC simulation is estimated from tag and probe efficiency tables Wöhri et al. (2011, 2012) that have been obtained from single J/ψ control samples in data and simulation. Hence, correlations among the two J/ψ in the event are neglected. Efficiencies from data and simulation tables are calculated for the events in data, and the difference in the two corrected signal yields is used as measure of the uncertainty.

The event-based efficiency correction ϵ_i is defined as

$$\epsilon_i = \epsilon_{\text{HLT},i} \cdot \epsilon_{\text{Offline},i} \tag{5.13}$$

where $\epsilon_{\text{HLT},i}$ is the event efficiency calculated for triggering the event (given that all muons were found offline) and $\epsilon_{\text{Offline},i}$ is the event efficiency for reconstructing, identifying, and selecting offline all four muons in an event.

The Trigger Efficiency

The `HLT_Dimuon0_Jpsi_muon` trigger path requires at least three muons to be found at the L3 stage, two of which must fit to a J/ψ vertex. The L1, L2, L3,

Table 5.21: L1, L2, L3, and overall HLT tags used in the specified run ranges.

Scenario	Run Range	HLT version	L1 Seed	L2	L3
1	165088-167913	`HLT_Dimuon0_Jpsi_Muon_v1-4`	`L1_DoubleMu0`	`TripleMuonL2`	`JpsiMuonL3`
2	170249-180252	`HLT_Dimuon0_Jpsi_Muon_v6-11`	`L1_TripleMu0`	`TripleMuonL2`	`JpsiMuonL3`

and overall HLT tags used over the data-taking period are shown in their given run ranges in Table 5.21.

It should be noted that although the name of the L1 seed changed from `L1_DoubleMu0` to `L1_TripleMu0` between the two periods, the actual L1 definition and requirement for three L1 muons did not. An event's HLT efficiency $\epsilon_{HLT,i}$ is calculated from the single muon HLT efficiencies $\epsilon^{\mu_j}_{HLT,i}$ ($j = 1, 2, 3, 4$ muon index) and vertexing efficiency ϵ_{vtx} as follows:

$$\begin{aligned}
\epsilon_{HLT,i} = {} & \epsilon^{\mu1}_{HLT,i} \cdot \epsilon^{\mu2}_{HLT,i} \cdot \epsilon^{\mu3}_{HLT,i} \cdot \epsilon^{\mu4}_{HLT,i} \cdot (2 \cdot \epsilon_{vtx} - \epsilon_{vtx} \cdot \epsilon_{vtx}) \\
& + \epsilon^{\mu1}_{HLT,i} \cdot \epsilon^{\mu2}_{HLT,i} \cdot \epsilon^{\mu3}_{HLT,i} \cdot (1 - \epsilon^{\mu4}_{HLT,i}) \cdot \epsilon_{vtx} \\
& + \epsilon^{\mu1}_{HLT,i} \cdot \epsilon^{\mu2}_{HLT,i} \cdot (1 - \epsilon^{\mu3}_{HLT,i}) \cdot \epsilon^{\mu4}_{HLT,i} \cdot \epsilon_{vtx} \\
& + \epsilon^{\mu1}_{HLT,i} \cdot (1 - \epsilon^{\mu2}_{HLT,i}) \cdot \epsilon^{\mu3}_{HLT,i} \cdot \epsilon^{\mu4}_{HLT,i} \cdot \epsilon_{vtx} \\
& + (1 - \epsilon^{\mu1}_{HLT,i}) \cdot \epsilon^{\mu2}_{HLT,i} \cdot \epsilon^{\mu3}_{HLT,i} \cdot \epsilon^{\mu4}_{HLT,i} \cdot \epsilon_{vtx} \ .
\end{aligned} \tag{5.14}$$

The single muon HLT efficiency is determined as the product of the L1, L2, and L3 efficiencies. The `L1_DoubleMu0` and `L1_TripleMu0` L1 seeds reference the same quality requirements, as do the `DoubleMuonL2` and `TripleMuonL2` modules. Therefore, the official tag and probe L1×L2 efficiencies as calculated for the `L1_DoubleMu0` are used from lookup tables in terms of muon p_{T} and η for seagull and cowboy topologies Wöhri et al. (2011, 2012). Likewise, `Dimuon0` lookup tables for the L3 trigger efficiency are used. Only muons that fullfill the tight acceptance definition are matched to L3 information. The J/ψ vertexing efficiency of the HLT is adopted from the tag and probe study Wöhri et al. (2011, 2012).

Offline Reconstruction Efficiency

The total offline reconstruction efficiency is the product of single muon efficiencies. The offline reconstruction efficiency for a muon passing the tight muon acceptance is given as

$$\epsilon^{\mu}_{\text{Reco}} = \epsilon^{\mu}_{\text{Tk}} \cdot \epsilon^{\mu}_{\text{Id}} \cdot \epsilon^{\mu}_{\text{Qual}} \tag{5.15}$$

where Tk refers to tracking ($\epsilon^{\mu}_{\text{Tk}} = 98.8\%$), Id to identification, and Qual to offline quality criteria. For muons that fail the tight muon acceptance but pass the loose muon acceptance (at most one muon per event), the $\epsilon^{\mu}_{\text{Reco}}$ is determined from a map in muon p_{T} and η generated with the muon particle gun (see Fig. 5.28). To arrive at an uncertainty in the comparison data versus simulation the data-based loose muon efficiency is varied by an amount Δ_i that is estimated from previous studies The CMS Collaboration (2012). The single muon efficiencies as function of muon transverse momentum from those studies are shown in Fig. 5.29. The Δ_i is calculated as relative variation $\Delta_i = \frac{|\epsilon_i^{\text{data}} - \epsilon_i^{\text{sim}}|}{\epsilon_i^{\text{sim}}}$. The resulting loose muon efficiency is calculated as $\epsilon^{\mu}_i = (1 \pm \Delta_i) \cdot \epsilon^{\mu}_{\text{Reco}}$. Both positive and negative variation due to Δ_i are considered. The

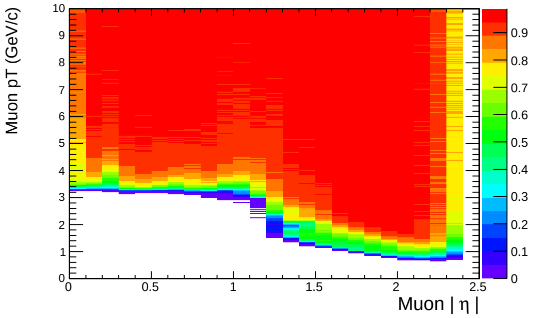

Figure 5.28: Map of the muon reconstruction efficiency from the muon particle gun simulation, with 25 bins in $|\eta|$ and 300 bins in p_{T}.

greatest variation of the signal yield is chosen as a conservative measure of the uncertainty. It should be noted that there is also an offline J/ψ vertex fit requirement of fit probability greater than 0.5%. However, in both our SPS and DPS signal samples the likelihood to successfully fit both vertices in an event is greater than 99% (99.9% for SPS and 99.6% for DPS), so the offline event reconstruction efficiency is considered to be entirely a product of the muon reconstruction efficiencies.

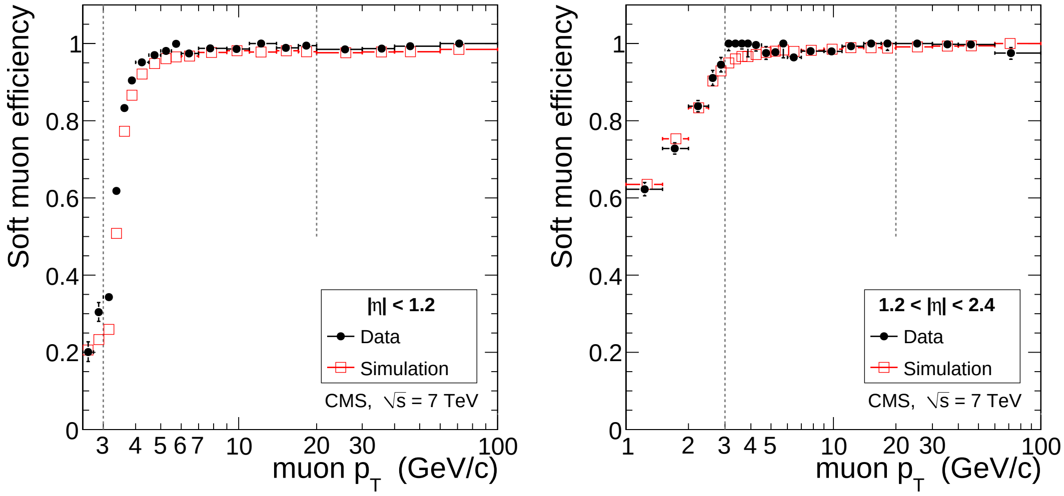

Figure 5.29: Single muon reconstruction efficiency in data (black) and simulation (red), reprinted from The CMS Collaboration (2012).

The relative difference in the total corrected signal yield, $|N^{\text{data}} - N^{\text{sim}}|/N^{\text{sim}}$, is found to be 6.5%.

- **Parameterization Uncertainties** – All PDF parameters that are fixed for the final fit are varied by their uncertainty as determined from the fits to data sideband and MC samples. The resolution function used to describe the *ct* of the prompt J/ψ has been parameterized as a double-Gaussian, but the outcome has been compared with the fit using a triple-Gaussian resolution function. For the background models, alternative fit shapes such as a third order polynomial or an exponential function are used. For the parameterization of the distribution of the J/ψ invariant mass alternatively a Crystal Ball function is considered. For the separation significance, a resolution function convolved with an exponential function (instead of a Landau plus Chebyshev polynomial) is considered for combinatorial background components. The largest difference of the signal yields in the fits with the two signal shape parameterizations, 0.6%, is taken as uncertainty to account for imperfect knowledge of the PDF. The alternate fits are defined in Appendix B.

- **Model Dependence of Signal Parameterization** – A reconstructed DPS and SPS sample is used to parameterize the signal. The difference in the signal yields between those two fits is accounted for as systematic uncertainty.

Table 5.22: Summary of relative systematic uncertainties (%) for the total cross section.

Source	Relative Uncertainty [%]
Branching Fractions	± 1.4
Luminosity	± 2.5
Acceptance Closure	± 1.1
Efficiency Calculation	± 4.4
Efficiency Scaling Factor	± 0.2
Muon Tracking	± 3.0
Detector Efficiency	± 6.5
Parameterization	± 0.6
Model for Signal	± 0.1
Systematic Total	± 9.0

Table 5.23: Summary of relative systematic uncertainties (%) for each M_{JJ} bin.

M_{JJ} (GeV/c^2)	6-8	8-13	13-22	22-35	35-80
Acceptance Closure	±7.9	±6.6	±1.7	±3.2	±8.6
Efficiency Calculation	±4.2	±7.5	±2.9	±6.0	±12.5
Efficiency Scaling Factor	±31.4	±18.8	±0.2	±10.6	±5.1
Detector Efficiency	±5.2	±9.8	±4.4	±9.8	±9.8
Systematic Total	±33.3	±23.8	±7.0	±16.5	±19.2

Table 5.24: Summary of relative systematic uncertainties (%) for each $|\Delta y|$ bin.

$\|\Delta y\|$	0-0.3	0.3-0.6	0.6-1	1-1.6	1.6-2.6	2.6-4.4
Acceptance Closure	±5.8	±3.8	±12.8	±3.3	±8.0	±23.6
Efficiency Calculation	±6.0	±7.3	±10.8	±9.6	±4.4	±11.0
Efficiency Scaling Factor	±6.4	±1.1	±5.1	±4.4	±0.5	±1.8
Detector Efficiency	±4.5	±10.8	±3.6	±10.8	±17.0	±10.5
Systematic Total	±12.2	±14.3	±18.4	±16.0	±19.7	±28.4

Table 5.25: Summary of relative systematic uncertainties (%) for each $p_{\mathrm{T}}^{\mathrm{JJ}}$ bin.

$p_{\mathrm{T}}^{\mathrm{JJ}}$ (GeV/c)	0-5	5-10	10-14	14-18	18-23	23-40
Acceptance Closure	±17.3	±9.7	±1.5	±9.0	±12.2	±9.4
Efficiency Calculation	±12.5	±15.1	±7.8	±5.3	±3.1	±3.6
Efficiency Scaling Factor	±0.6	±6.3	±2.3	±0.2	±1.5	±1.2
Detector Efficiency	±4.2	±9.0	±5.4	±8.3	±11.0	±8.1
Systematic Total	±22.1	±21.5	±10.8	±14.0	±17.3	±13.6

The individual relative uncertainties for the total cross section are listed in Table 5.22. The total systematic uncertainty is calculated as the sum in quadrature of the individual uncertainties. The systematic uncertainty for the differential cross sections is evaluated on a per-bin basis for the Acceptance Closure, Efficiency Calculation, Efficiency Scaling Factor, and Detector Efficiency sources of uncertainty, and their relative contribution for each kinematic bin are shown in Tables 5.23, 5.24, and 5.25.

To study the effect of a non-isotropic muon decay on the measured cross section, the event-based acceptance is determined using extreme scenarios. With θ_+ defined as the angle between the μ^+ direction in the J/ψrest frame and the J/ψdirection in the pp center-of-mass frame, the angular distribution of decay muons is parameterized as:

$$\frac{dN}{d\cos\theta_+} = 1 + \lambda\cos^2\theta_+ \tag{5.16}$$

where λ is a polarization observable; $\lambda = 0$ corresponds to an isotropic J/ψdecay, while $\lambda = +1$ ($\lambda = -1$) corresponds to longitudinal (transverse) polarization of the

J/ψin accordance with e.g. Chao et al. (2012). As compared to the $\lambda = 0$ case, the total cross section is 30.6% lower for $\lambda = -1$ and 27.2% higher for $\lambda = +1$. Table 5.26 lists the change in total cross section in data for different assumptions of λ_θ relative to the assumption of isotropic J/ψ decays. Figure 5.30 shows the differential cross section in data as a function of the kinematic variables under the extreme scenarios of $\lambda_\theta = \pm 1$, scaled to the same total cross section as for $\lambda_\theta = 0$. The differential cross section measurements for $\lambda = \pm 1$ lie within the statistical uncertainties of the $\lambda = 0$ case when scaled to the same total cross section, indicating that different polarization assumptions result in the same relative distribution.

Table 5.26: The percent change of total cross section calculated under the assumption of decay distributions parameterized by different λ_θ values relative to the isotropic assumption $\lambda_\theta = 0$.

λ_θ used	-1	-0.9	-0.8	-0.7	-0.6	-0.5	-0.4	-0.3	-0.2	-0.1
$\frac{\Delta\sigma}{\sigma_{\lambda=0}}$ (%)	-30.6	-27.0	-23.9	-20.8	-17.7	-14.6	-12.0	-9.2	-5.2	-2.6
λ_θ used	0.1	0.2	0.3	0.4	0.5	0.6	0.7	0.8	0.9	1
$\frac{\Delta\sigma}{\sigma_{\lambda=0}}$ (%)	+4.2	+5.7	+8.7	+11.0	+14.9	+16.4	+20.4	+23.3	+25.8	+27.2

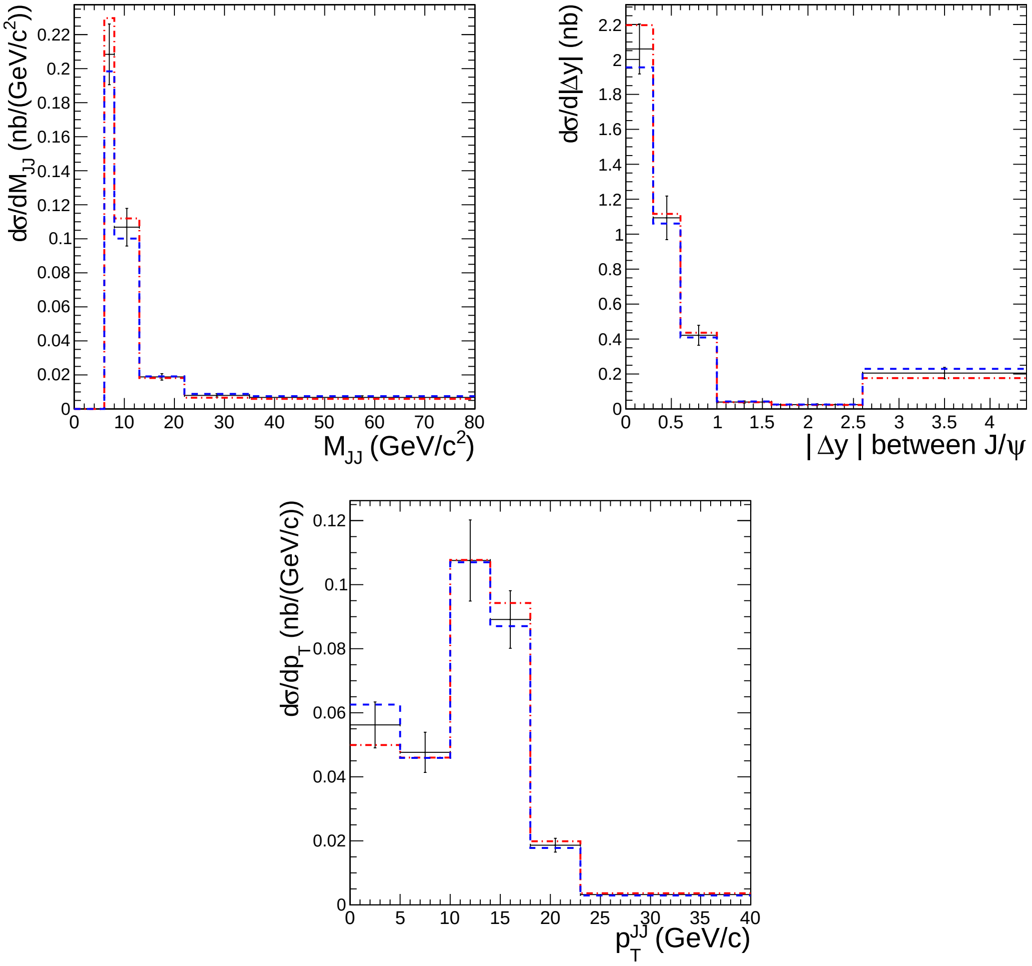

Figure 5.30: Differential cross section $d\sigma$ for prompt double J/ψ production, as a function of the JJ invariant mass (top left), the absolute rapidity difference $|\Delta y|$ (top right), and the double J/ψ transverse momentum (bottom) under different J/ψ decay parameterizations. The black bars represent the isotropic decay assumption $\lambda_\theta = 0$, and the error bars depict statistical error only. The distributions assuming $\lambda_\theta = +1$ (blue, dashed) and assuming $\lambda_\theta = -1$ (red, dotted and dashed) have been scaled to the same total cross section as the $\lambda_\theta = 0$ case.

5.10 Results

5.10.1 Cross Section Evaluation

Signal weights n^{i}_{sig} for each selected event in data are obtained from our maximum likelihood fit using the sPlot technique Pivk and Le Diberder (2005) and the cross section is obtained according to the sum of Eq. 5.1. For the calculation, $\mathcal{L}$ = (4.73±0.12) fb^{-1} and $BF(\mathrm{J}/\psi \rightarrow \mu^{+}\mu^{-})$ = (5.93± 0.06) % are used. All cross section results are determined within the J/ψ acceptance region.

The differential cross section as a function of M_{JJ} is shown in Fig. 5.31, with the corresponding numerical values summarized in Table 5.27. The differential cross section as a function of $|\Delta y|$ is shown in Fig. 5.32, with the corresponding numerical values summarized in Table 5.28. The differential cross section as a function of $p_{\mathrm{T}}^{\mathrm{JJ}}$ is shown in Fig. 5.33, with the corresponding numerical values summarized in Table 5.29.

Table 5.27: Summary of differential cross section $d\sigma/dM_{\mathrm{JJ}}$ (nb/(GeV/c^2)) in bins of M_{JJ}. The uncertainties are statistical first, then systematic.

Mass Bin (GeV/c^2)	$d\sigma/dM_{\mathrm{JJ}}$ (nb/(GeV/c^2))
$6-8$	$0.208 \pm 0.018 \pm 0.069$
$8-13$	$0.107 \pm 0.011 \pm 0.025$
$13-22$	$0.019 \pm 0.002 \pm 0.001$
$22-35$	$0.008 \pm 0.001 \pm 0.001$
$35-80$	$0.007 \pm 0.001 \pm 0.001$

The total cross section is determined by summing over the sample on an event-by-event basis as:

$$\sigma(pp \rightarrow \mathrm{J}/\psi\ \mathrm{J}/\psi + X) = 1.49 \pm 0.07 \pm 0.13\ \mathrm{nb} \tag{5.17}$$

with statistical and systematic uncertainty shown, respectively.

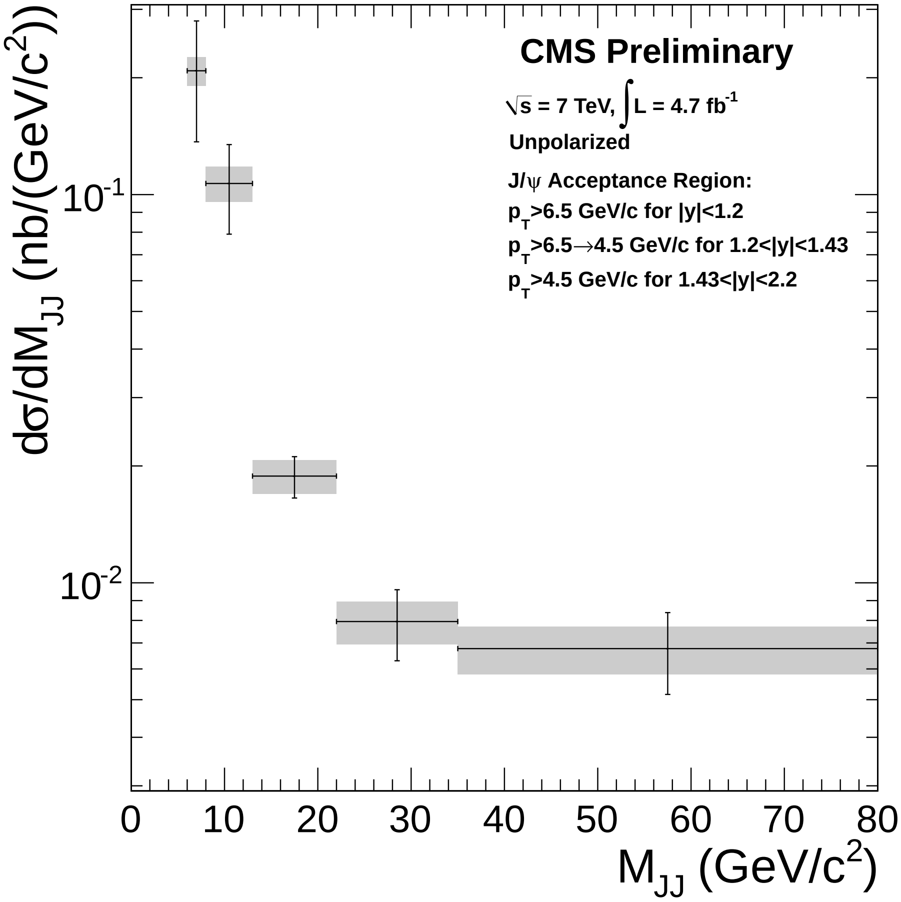

Figure 5.31: Summary of the measured differential cross section $d\sigma/dM_{\rm JJ}$ for double J/ψ production. The box represents statistical error, and the error bars represent statistical and systematic error added in quadrature.

Table 5.28: Summary of differential cross section $d\sigma/d|\Delta y|$ (nb) in bins of $|\Delta y|$. The uncertainties shown are statistical first, then systematic.

$\|\Delta y\|$ Bin	$d\sigma/d\|\Delta y\|$ (nb)
$0 - 0.3$	$2.06 \pm 0.143 \pm 0.251$
$0.3 - 0.6$	$1.09 \pm 0.125 \pm 0.156$
$0.6 - 1.0$	$0.421 \pm 0.057 \pm 0.077$
$1.0 - 1.6$	$0.040 \pm 0.006 \pm 0.006$
$1.6 - 2.6$	$0.025 \pm 0.005 \pm 0.005$
$2.6 - 4.4$	$0.205 \pm 0.033 \pm 0.058$

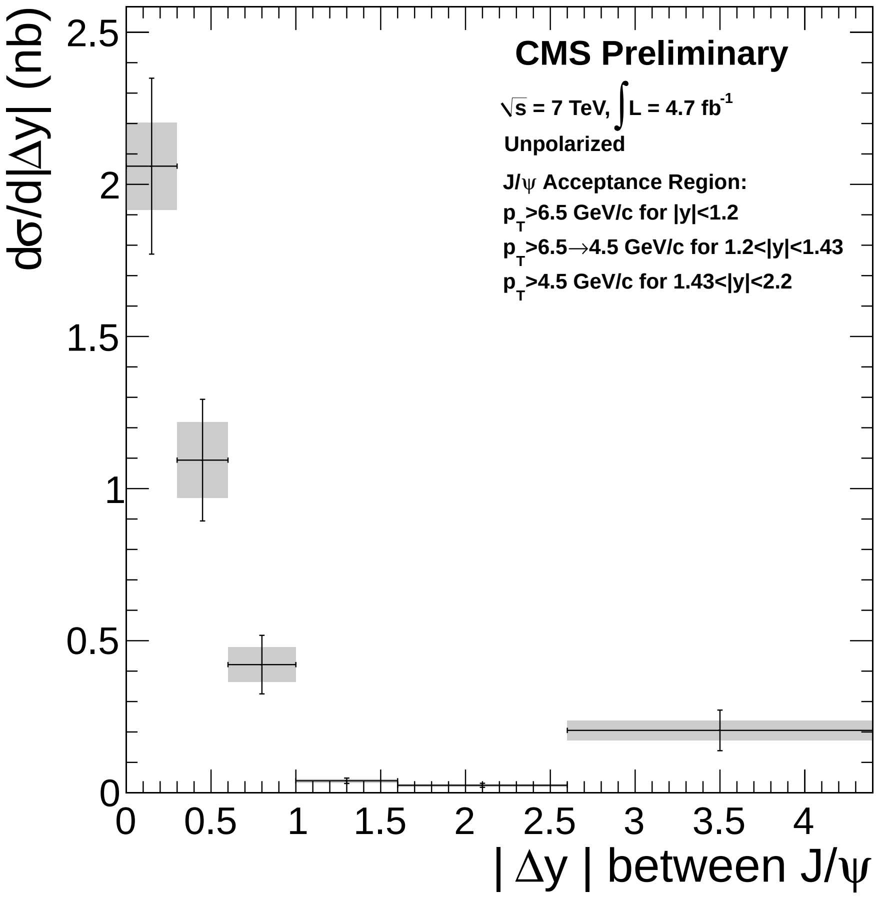

Figure 5.32: Summary of the measured differential cross section $d\sigma/d|\Delta y|$ for double J/ψ production. The boxes represents statistical error and the error bars represent statistical and systematic error added in quadrature.

Table 5.29: Summary of differential cross section $d\sigma/dp_{\mathrm{T}}^{\mathrm{JJ}}$ (nb/(GeV/c)) in bins of double J/ψ transverse momentum. The uncertainties shown are statistical first, then systematic.

$p_{\mathrm{T}}^{\mathrm{JJ}}$ Bin (GeV/c)	$d\sigma/dp_{\mathrm{T}}^{\mathrm{JJ}}$ (nb/(GeV/c))
$0-5$	$0.056 \pm 0.007 \pm 0.012$
$5-10$	$0.048 \pm 0.006 \pm 0.010$
$10-14$	$0.108 \pm 0.013 \pm 0.012$
$14-18$	$0.089 \pm 0.009 \pm 0.012$
$18-23$	$0.019 \pm 0.002 \pm 0.003$
$23-40$	$0.003 \pm 0.0004 \pm 0.0004$

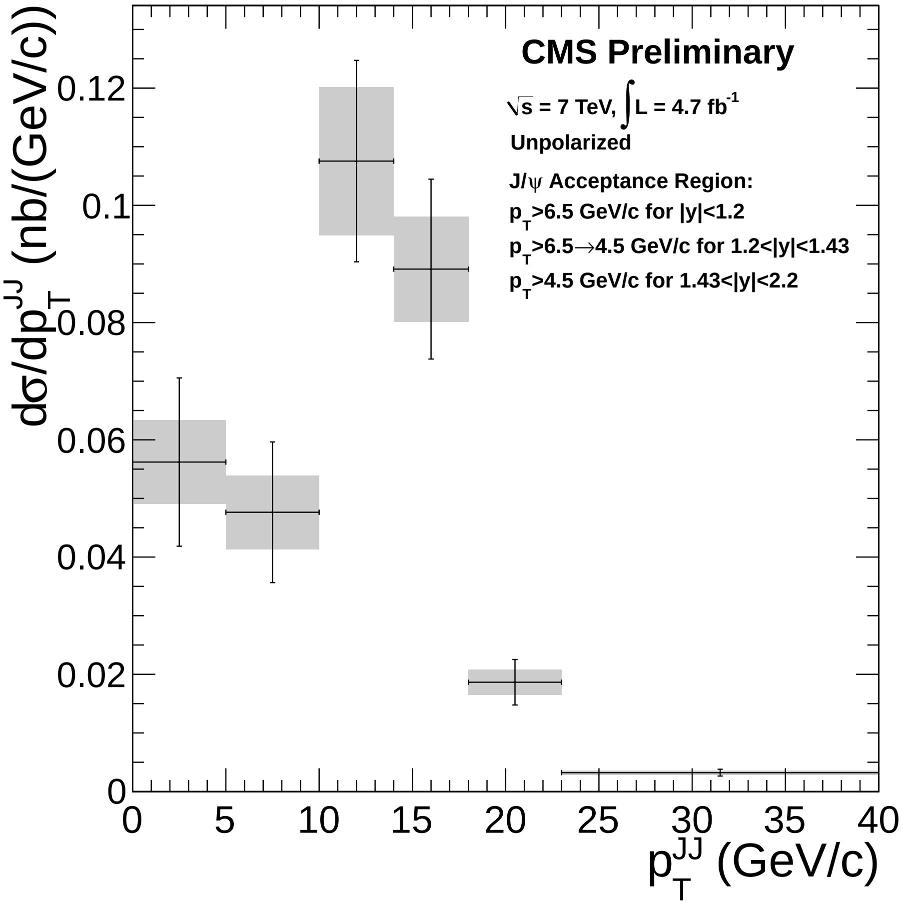

Figure 5.33: Summary of the measured differential cross section $d\sigma/dp_{\mathrm{T}}^{\mathrm{JJ}}$ for double J/ψ production. The boxes represents statistical error and the error bars represent statistical and systematic error added in quadrature.

5.10.2 Resonance Search

The reconstructed gaussian width of the η_b is 0.08 GeV/c^2, as determined from the η_b sample described in Section 5.2 with standard selection criteria applied. A signal interval of $9.16 - 9.64$ GeV/c^2 is defined, corresponding to three standard deviations on either side of the mean mass value. Two sideband regions with the same width are defined in the intervals $8.68 - 9.16$ GeV/c^2 and $9.64 - 10.12$ GeV/c^2. Fig. 5.34 shows the M_{JJ} distribution for reconstructed η_b simulation. To understand the manner in which the CMS acceptance coverage and efficiency can impact the final M_{JJ} distribution, the SPS and DPS MC samples are studied. For both types of production, the M_{JJ} distribution of events that pass the final reconstruction and selection criteria is divided by the M_{JJ} distribution for all generated events (before the J/ψ or muon acceptance criteria have been applied), shown in Fig. 5.35. For both the SPS and DPS events, the relative fraction of the M_{JJ} events reconstructed by CMS in the signal interval agrees (within the uncertainty) to the mean of the sideband intervals. Figure 5.36 shows the double J/ψ invariant mass distribution in data around the nominal η_b mass Beringer et al. (2012), before efficiency and acceptance correction. The dashed bars in Fig. 5.36 delineate the signal interval and the two sideband intervals. A first degree polynomial is fit to the yields in the sideband regions. Integrating this function over the signal region predicts 15 ± 4 non-resonant events. The total double J/ψyield in data for this region is 15 ± 4 events with statistical error. Hence, no significant resonant contribution is observed.

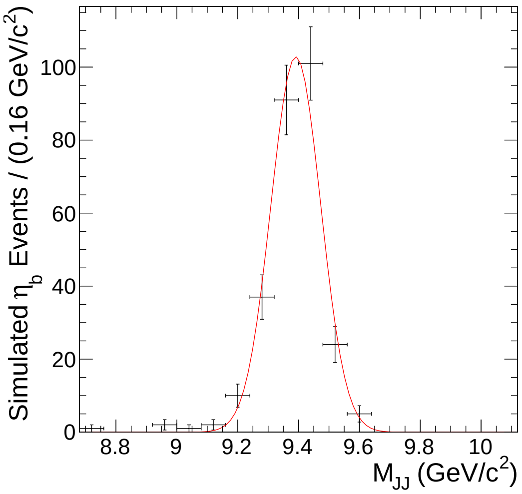

Figure 5.34: M_{JJ} distribution for simulated η_b events fit to a Gaussian distribution.

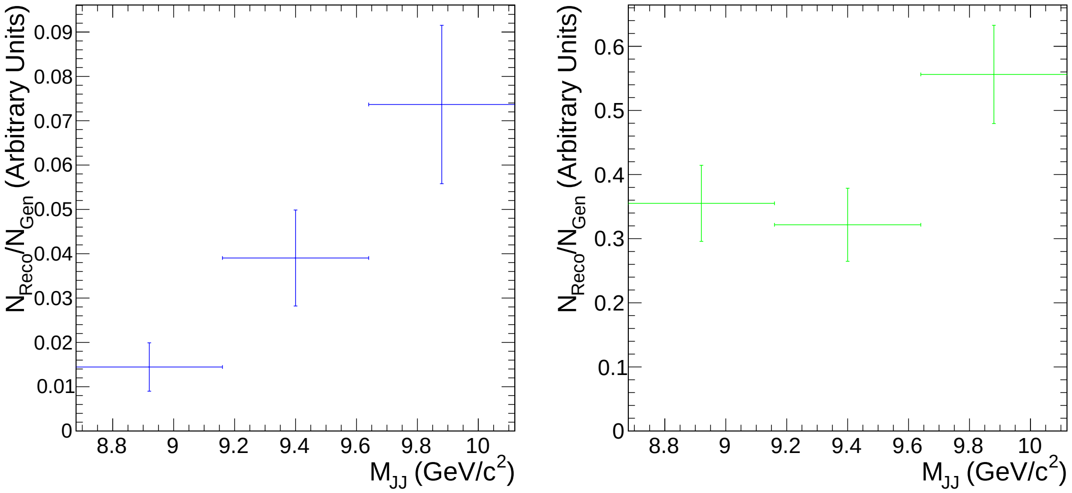

Figure 5.35: The M_{JJ} distribution of events that pass the final reconstruction and selection criteria is divided by the M_{JJ} distribution for all generated events (before the J/ψ or muon acceptance criteria have been applied), shown for the SPS (left, blue) and DPS (right, green) mass centered around the η_b mass region. Error bars represent statistical error due to the population in the reconstructed distribution. The y-axis is shown in arbitrary units as only the relative shape is being examined.

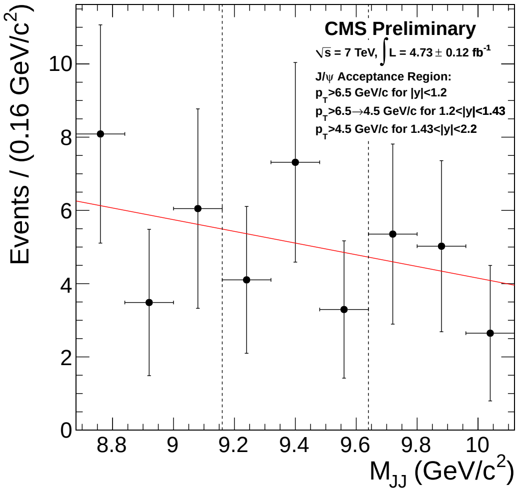

Figure 5.36: Prompt double J/ψ events in bins of the JJ invariant mass centered around the η_b mass region. The error bars represent statistical error.

5.11 Conclusion

A signal yield of 446 ± 23 events for the production of two prompt J/ψ mesons originating from a common vertex has been observed with the CMS detector in proton-proton collisions at $\sqrt{s} = 7$ TeV at the LHC from a sample corresponding to an integrated luminosity of 4.73 ± 0.12 fb^{-1}. A data-based method was used to correct for acceptance and efficiency minimizing the model dependence of the cross section determination. The total cross section of double J/ψ production was measured within an acceptance region defined by the individual J/ψtransverse momentum and rapidity and was found to be $\sigma = 1.49 \pm 0.07 \pm 0.13$ nb, where the first uncertainty is statistical and the second systematic. Differential cross sections were obtained in bins of the double J/ψ invariant mass, the absolute rapidity difference between the two J/ψ mesons, and the transverse momentum of the double J/ψ system. These measurements probe a higher J/ψ transverse momenta region than previous measurements, a region where double J/ψproduction via octet J/ψ states and higher order corrections are important. The differential cross section in bins of $|\Delta y|$ is sensitive to DPS contributions to prompt double J/ψ production. The data show evidence for excess at $|\Delta y| > 2.6$, a region that current models suggest is exclusively populated via DPS production Kom et al. (2011); Gaunt et al. (2011); Novoselov (2011). In the M_{JJ} event distribution, no excess above the background expectation derived from non-resonant sidebands was observed.

Bibliography

Bibliography

(2008). Wikimedia Commons. `http://commons.wikimedia.org/wiki/Main_Page`. 5

(2013). CMS Luminosity Based on Pixel Cluster Counting - Summer 2013 Update. Technical Report CMS-PAS-LUM-13-001, CERN, Geneva. 91, 100, 139

Aad, G. et al. (2012). Observation of a new particle in the search for the Standard Model Higgs boson with the ATLAS detector at the LHC. *Phys.Lett.*, B716:1–29. 1, 5

Aaij, R. et al. (2012). Observation of double charm production involving open charm in pp collisions at $\sqrt{s}$=7 TeV. *JHEP*, 1206:141. 87

Agostinelli, S. et al. (2003). Geant4 - a simulation toolkit. *Nuclear Instruments and Methods in Physics Research Section A: Accelerators, Spectrometers, Detectors and Associated Equipment*, 506(3):250 – 303. 90

Artoisenet, P., Lansberg, J., and Maltoni, F. (2007). Hadroproduction of J/ψ and υ in association with a heavy-quark pair. *Phys.Lett.*, B653:60–66. 87

Aubert, B. et al. (2009). Evidence for the eta(b)(1S) Meson in Radiative Upsilon(2S) Decay. *Phys.Rev.Lett.*, 103:161801. 22, 88

Badier, J. et al. (1982). Evidence for $\psi\psi$ Production in π^- Interactions at 150-GeV/c and 280-GeV/c. *Phys.Lett.*, B114:457. 87

Badier, J. et al. (1985). $\psi\psi$ Production and Limits on Beauty Meson Production From 400-GeV/c Protons. *Phys.Lett.*, B158:85. 87

Berezhnoy, A., Likhoded, A., Luchinsky, A., and Novoselov, A. (2011). Double J/psi-meson Production at LHC and 4c-tetraquark state. *Phys.Rev.*, D84:094023. 22, 87, 88

Berezhnoy, A., Likhoded, A., Luchinsky, A., and Novoselov, A. (2012). Double $c\bar{c}$ production at LHCb. *Phys.Rev.*, D86:034017. 87, 93, 106

Beringer, J. et al. (2012). Review of Particle Physics (RPP). *Phys. Rev. D*, 86:010001. 18, 61, 139, 152

Braaten, E., Fleming, S., and Leibovich, A. K. (2001). NRQCD analysis of bottomonium production at the Tevatron. *Phys.Rev.*, D63:094006. 22, 88

Brning, O. S., Collier, P., Lebrun, P., Myers, S., Ostojic, R., Poole, J., and Proudlock, P. (2004). *LHC Design Report*. CERN, Geneva. 23

Campbell, J. M., Maltoni, F., and Tramontano, F. (2007). QCD corrections to J/psi and Upsilon production at hadron colliders. *Phys.Rev.Lett.*, 98:252002. 87

Chao, K.-T., Ma, Y.-Q., Shao, H.-S., Wang, K., and Zhang, Y.-J. (2012). J/ψ Polarization at Hadron Colliders in Nonrelativistic QCD. *Phys.Rev.Lett.*, 108:242004. 146

Chatrchyan, S. et al. (2008). The CMS experiment at the CERN LHC. *JINST*, 3:S08004. 24, 32, 49, 90

Chatrchyan, S. et al. (2012a). Observation of a new boson at a mass of 125 GeV with the CMS experiment at the LHC. *Phys.Lett.*, B716:30–61. 1, 5

Chatrchyan, S. et al. (2012b). Search for a light pseudoscalar Higgs boson in the dimuon decay channel in pp collisions at $\sqrt{s} = 7$ TeV. *Phys.Rev.Lett.*, 109:121801. 22, 88

CMS Collaboration (1997a). *The CMS Hadron Calorimeter Project: Technical Design Report*. Technical Design Report CMS. CERN, Geneva. 45

CMS Collaboration (1997b). *The CMS Muon Project: Technical Design Report*. Technical Design Report CMS. CERN, Geneva. 49

CMS Collaboration (2002). *CMS trigger and data-acquisition project: Technical Design Report*. Technical Design Report CMS. CERN, Geneva. 53, 55

CMS Collaboration (2005). *CMS computing: Technical Design Report*. Technical Design Report CMS. CERN, Geneva. 56

CMS Collaboration (2006a). *CMS Physics Technical Design Report Volume I: Detector Performance and Software*. Technical Design Report CMS. CERN, Geneva. 24, 32, 66

CMS Collaboration (2006b). *CMS TriDAS project: Technical Design Report I; the trigger systems*. Technical Design Report CMS. CERN, Geneva. 53

CMS Collaboration (2010). Measurement of tracking efficiency. CMS Physics Analysis Summary CMS-PAS-TRK-10-002, CERN. 140

Collaboration, C. (2006). Search for etab at CDF. CDF Public Note 20066/8448, Fermilab. 22, 88

Dermisek, R. and Gunion, J. F. (2005). Escaping the large fine tuning and little hierarchy problems in the next to minimal supersymmetric model and h to aa decays. *Phys.Rev.Lett.*, 95:041801. 22, 88

Domingo, F. (2011). Updated constraints from radiative Υ decays on a light CP-odd Higgs. *JHEP*, 1104:016. 22, 88

Domingo, F., Ellwanger, U., and Sanchis-Lozano, M.-A. (2009). Bottomoniom spectroscopy with mixing of eta(b) states and a light CP-odd Higgs. *Phys.Rev.Lett.*, 103:111802. 22, 88

Evans, L. and Bryant, P. (2008). Lhc machine. *Journal of Instrumentation*, 3(08):S08001. 23

Fruhwirth, R. (1987a). Application of kalman filtering to track and vertex fitting. *Nucl. Instrum. Methods Phys. Res., A*, 262(HEPHY-PUB-503):444. 58

Fruhwirth, R. (1987b). Application of Kalman filtering to track and vertex fitting. *Nucl.Instrum.Meth.*, A262:444–450. 97

Gaunt, J. R., Kom, C., Kulesza, A., and Stirling, W. (2011). Probing double parton scattering with leptonic final states at the LHC. 87, 155

Glashow, S. (1961). Partial Symmetries of Weak Interactions. *Nucl.Phys.*, 22:579–588. 11

Gong, B. and Wang, J.-X. (2008). QCD corrections to polarization of J/ψ and υ at Tevatron and LHC. *Phys.Rev.*, D78:074011. 87

Greenberg, O. (1964). Spin and Unitary Spin Independence in a Paraquark Model of Baryons and Mesons. *Phys.Rev.Lett.*, 13:598–602. 9

Griffiths, D. (2005). *Introduction to Quantum Mechanics*. Pearson international edition. Pearson Education, Limited. 5

Humpert, B. and Mery, P. (1983). psi psi Production at Collider Energies. *Z.Phys.*, C20:83. 87

Ivova, M. (2011). Lorenz angle in the cms pixel detector. In *Talk at Tracker DPG, CERN, Switzerland*. 67, 69

James, E., Maravin, Y., Mulders, M., and Neumeister, N. (2006). Muon identification in CMS. 97

Jia, Y. (2008). Which hadronic decay modes are good for eta(b) searching: double J/psi or something else? *Phys.Rev.*, D78:054003. 22, 88

Ko, P., Yu, C., and Lee, J. (2011). Inclusive double-quarkonium production at the Large Hadron Collider. *JHEP*, 1101:070. 86

Kom, C., Kulesza, A., and Stirling, W. (2011). Pair Production of J/psi as a Probe of Double Parton Scattering at LHCb. *Phys.Rev.Lett.*, 107:082002. 86, 87, 155

Maltoni, F. and Polosa, A. (2004). Observation potential for eta(b) at the Tevatron. *Phys.Rev.*, D70:054014. 22, 88

Novoselov, A. (2011). Double parton scattering as a source of quarkonia pairs in LHCb. 87, 155

Pivk, M. and Le Diberder, F. R. (2005). sPlot: A statistical tool to unfold data distributions. *Nuclear Instruments and Methods in Physics Research A*, 555:356–369. 117, 128, 148

Qiao, C.-F., Sun, L.-P., and Sun, P. (2010). Testing Charmonium Production Mechamism via Polarized J/psi Pair Production at the LHC. *J.Phys.G*, G37:075019. 87

Salam, A. (1968). Weak and Electromagnetic Interactions. *Conf.Proc.*, C680519:367–377. 11

Sjostrand, T., Mrenna, S., and Skands, P. Z. (2006). PYTHIA 6.4 Physics and Manual. *JHEP*, 0605:026. 88

Sjostrand, T., Mrenna, S., and Skands, P. Z. (2008). A Brief Introduction to PYTHIA 8.1. *Comput.Phys.Commun.*, 178:852–867. 89

Swartz, M., Fehling, D., Giurgiu, G., Maksimovic, P., and Chiochia, V. (2007). A new technique for the reconstruction, validation, and simulation of hits in the CMS Pixel Detector. *PoS*, Vertex 2007(CMS-NOTE-2007-033):035. 37 p. 78

The CMS Collaboration (2012). Performance of CMS muon reconstruction in pp collision events at $\sqrt{s} = 7TeV$. *Journal of Instrumentation*, 7:2P. xxvii, 142, 143

Verkerke, W. and Kirkby, D. (2003). The RooFit toolkit for data modeling. *ArXiv Physics e-prints*. 57, 117

Weinberg, S. (1967). A Model of Leptons. *Phys.Rev.Lett.*, 19:1264–1266. 11

Wöhri, H., Krätschmer, I., Wang, J., and Zhang, L. (2011). T&P single muon efficiencies for low p_t dimuon triggers in 2011. CMS Note 2011/417, CERN. 98, 102, 140, 141, 142

Wöhri, H., Krätschmer, I., Zhang, L., Knünz, V., Faccioli, P., Lourenço, C., and Abbiendi, G. (2012). Low p_t muon and dimuon efficiencies. CMS Note 2012/088, CERN. 140, 141, 142

Appendix

Appendix A

Values Found for PDFs of Primary Fit

Tables A.1, A.2, and A.3 display the PDF values determined by the primary fit based on the signal prompt double J/ψ sample.

Table A.1: PDF parameters for $M_{J/\psi}$ in signal prompt double J/ψ production.

Signal $M_{J/\psi}$	Value	Error
μ_1^1	3.09313	$1.23265 \cdot 10^{-3}$
σ_1^1	$5.79266 \cdot 10^{-2}$	$5.18787 \cdot 10^{-3}$
σ_2^1	$4.56886 \cdot 10^{-1}$	$2.88027 \cdot 10^{-2}$
f^1	$1.80473 \cdot 10^{-1}$	$5.52695 \cdot 10^{-2}$
μ_1^2	3.08933	$1.59605 \cdot 10^{-3}$
σ_1^2	$5.06183 \cdot 10^{-2}$	$5.49871 \cdot 10^{-3}$
σ_2^2	$5.82996 \cdot 10^{-1}$	$5.04930 \cdot 10^{-2}$
f^2	$4.47328 \cdot 10^{-1}$	$2.30313 \cdot 10^{-2}$

Tables A.4 and A.5 display the PDF values determined by the primary fit based on a cocktail of B-background MC. The $M_{J/\psi}$ parameters are taken from the signal sample.

Table A.2: PDF parameters for $ct_{xy}(J/\psi_1)$ in signal prompt double J/ψ production.

Signal $ct_{xy}(J/\psi)$	Value	Error
μ_1^1	$2.63860 \cdot 10^{-5}$	$8.04013 \cdot 10^{-5}$
μ_2^1	$1.19874 \cdot 10^{-3}$	$5.18535 \cdot 10^{-4}$
σ_1^1	$2.72201 \cdot 10^{-3}$	$1.09188 \cdot 10^{-4}$
σ_2^1	2.72258	$1.59567 \cdot 10^{-1}$
f^1	$8.47797 \cdot 10^{-1}$	$3.27593 \cdot 10^{-2}$

Table A.3: PDF parameters for $d^{J/\psi}$ in signal prompt double J/ψ production.

Signal $d^{J/\psi}$	Value	Error
μ^1	$4.08278 \cdot 10^{-1}$	$1.56988 \cdot 10^{-2}$
σ^1	$2.17748 \cdot 10^{-1}$	$1.64741 \cdot 10^{-2}$
λ^1	$6.76288 \cdot 10^{-1}$	$2.17191 \cdot 10^{-2}$

Table A.4: PDF parameters for $ct_{xy}(J/\psi_1)$ in a cocktail of B-background MC.

B-bkg. $ct_{xy}(J/\psi)$	Value	Error
μ^1	$6.51060 \cdot 10^{-4}$	$1.00314 \cdot 10^{-3}$
σ^1	$3.77146 \cdot 10^{-3}$	$7.63876 \cdot 10^{-4}$
λ^1	$1.59424 \cdot 10^{-2}$	$1.42585 \cdot 10^{-3}$

Table A.5: PDF parameters for $d^{J/\psi}$ in a cocktail of B-background MC.

B-bkg. $d^{J/\psi}$	Value	Error
μ^1	1.18073	$2.45563 \cdot 10^{-1}$
σ^1	$5.15922 \cdot 10^{-1}$	$2.26415 \cdot 10^{-1}$
λ^1	$1.0 \cdot 10^{2}$	$9.90301 \cdot 10^{1}$

Tables A.6, A.7, A.8, and A.9 display the PDF values determined by the primary fit based on one sideband extracted from data for the J/ψ-combinatorial, combinatorial-J/ψ, and combinatorial-combinatorial components.

Table A.6: PDF parameters for $M_{J/\psi}$ from the sidebands extracted from data for the combinatorial part of the J/ψ-combinatorial, combinatorial-J/ψ, and combinatorial-combinatorial components. The explanation of the method is given in Section 5.6.2.

Comb.-J/ψ $M_{J/\psi}$	Value	Error
a_0^1	$-2.93132 \cdot 10^{-1}$	$1.03292 \cdot 10^{-1}$
a_1^1	$-3.89092 \cdot 10^{-1}$	$1.32480 \cdot 10^{-1}$
a_2^1	$1.94808 \cdot 10^{-1}$	$1.09782 \cdot 10^{-1}$
a_0^2	$-2.10268 \cdot 10^{-1}$	$1.03007 \cdot 10^{-1}$
a_1^2	$-1.95504 \cdot 10^{-1}$	$1.35851 \cdot 10^{-1}$
a_2^2	$5.00755 \cdot 10^{-2}$	$9.96932 \cdot 10^{-2}$

Table A.7: PDF parameters for $ct_{xy}(J/\psi_1)$ and $d^{J/\psi}$ from the first sideband extracted from data for the J/ψ-combinatorial component. The explanation of the method is given in Section 5.6.2.

J/ψ-Comb. $ct_{xy}, d^{J/\psi}$	Value	Error
μ_1^1	$1.04093 \cdot 10^{-2}$	$1.40520 \cdot 10^{-3}$
μ_2^1	$-2.51869 \cdot 10^{-4}$	$8.65756 \cdot 10^{-4}$
σ_1^1	$1.24609 \cdot 10^{-2}$	$7.63379 \cdot 10^{-4}$
σ_2^1	$2.63519 \cdot 10^{-1}$	$7.86723 \cdot 10^{-2}$
f^1	$7.07283 \cdot 10^{-1}$	$8.34261 \cdot 10^{-2}$
a_0	$9.99840 \cdot 10^{-1}$	1.74272
a_1	$2.00471 \cdot 10^{-6}$	$2.83604 \cdot 10^{-1}$
f_{Landau}	$6.48517 \cdot 10^{-1}$	$5.61172 \cdot 10^{-2}$
μ_{Landau}	1.00181	$1.04945 \cdot 10^{-1}$
σ_{Landau}	$4.35740 \cdot 10^{-1}$	$7.23716 \cdot 10^{-2}$

Table A.8: PDF parameters for $ct_{xy}(J/\psi_1)$ and $d^{J/\psi}$ from the second sideband extracted from data for the combinatorial-J/ψ component. The explanation of the method is given in Section 5.6.2.

Comb.-J/ψ $ct_{xy}, d^{J/\psi}$	Value	Error
μ_1^1	$3.60489 \cdot 10^{-2}$	$6.43472 \cdot 10^{-2}$
μ_2^1	$4.32342 \cdot 10^{-3}$	$1.16219 \cdot 10^{-3}$
σ_1^1	$2.89854 \cdot 10^{-2}$	$1.9 \cdot 10^{-2}$
σ_2^1	$3.60637 \cdot 10^{-1}$	$3.7 \cdot 10^{-1}$
f^1	$6.27677 \cdot 10^{-2}$	$7.3 \cdot 10^{-2}$
a_0	$6.58858 \cdot 10^{-1}$	$7.74664 \cdot 10^{-1}$
a_1	$2.48596 \cdot 10^{-5}$	$3.98192 \cdot 10^{-1}$
f_{Landau}	$5.33780 \cdot 10^{-1}$	$1.70924 \cdot 10^{-1}$
μ_{Landau}	1.09999	$1.17982 \cdot 10^{-1}$
σ_{Landau}	$4.64046 \cdot 10^{-1}$	$7.03453 \cdot 10^{-3}$

Table A.9: PDF parameters for $ct_{xy}(J/\psi_1)$ and $d^{J/\psi}$ from the sample populating the mass sidebands of both J/ψ in data and used to characterize the combinatorial-combinatorial component. The explanation of the method is given in Section 5.6.2.

Comb.-Comb. $ct_{xy}, d^{J/\psi}$	Value	Error
μ_1^1	$4.78646 \cdot 10^{-3}$	$2.25302 \cdot 10^{-3}$
μ_2^1	$5.38739 \cdot 10^{-3}$	$4.58928 \cdot 10^{-4}$
σ_1^1	$1.20037 \cdot 10^{-2}$	$1.63207 \cdot 10^{-3}$
σ_2^1	$4.38348 \cdot 10^{-2}$	$2.77349 \cdot 10^{-2}$
f^1	$8.87066 \cdot 10^{-1}$	$7.59609 \cdot 10^{-2}$
a_0	$3.86180 \cdot 10^{-1}$	$5.83845 \cdot 10^{-1}$
a_1	$9.49975 \cdot 10^{-1}$	$9.19403 \cdot 10^{-1}$
f_{Landau}	$7.28332 \cdot 10^{-1}$	$1.63095 \cdot 10^{-1}$
μ_{Landau}	1.56581	$3.50069 \cdot 10^{-1}$
σ_{Landau}	$5.51089 \cdot 10^{-1}$	$1.94083 \cdot 10^{-1}$

Appendix B

Results of Alternate Fits

Several variations of the central fit technique have been tried, described in Section 5.6.

- Variant 1: uses a Crystal Ball function to parameterize $M^1_{\mu\mu}$ and $M^2_{\mu\mu}$ for signal case; other PDFs are identical to primary fit.
- Variant 2: $d^{J/\psi}$ is parameterized by the product of a Gaussian and a decay function in all cases (including the combinatorial cases); other PDFs are identical to primary fit.
- Variant 3: uses a Crystal Ball function to parameterize $M^1_{\mu\mu}$ and $M^2_{\mu\mu}$ for the signal case, $d^{J/\psi}$ is parameterized by the product of a Gaussian and a decay function in all cases (including the combinatorial cases); other PDFs are identical to primary fit.
- Variant 4: uses SPS simulation to parameterize the signal PDFs, but is otherwise identical to primary fit.

The resulting signal and background yields using these variations are shown in Table B.1. The signal yield never changes by more than 0.6%, which is taken as an estimate of uncertainty due to chosen method of parameterization.

Tables B.2 and B.3, as well as Fig. B.1 display the results of using a Crystal Ball function to characterize the shape of the $M_{\mu\mu}$. This parameterization was not

Table B.1: Summary of signal and background yields determined by fitting simultaneously M_{J/ψ^1}, M_{J/ψ^2}, $ct_{xy}(J/\psi^1)$, and $d^{J/\psi}$ for 1043 selected candidate events using variations on the central fitting method.

Parameter	Variant 1	Variant 2	Variant 3	Variant 4
N_{sig}	445 ± 23	448 ± 23	447 ± 23	446 ± 24
$N_{\mathrm{non-prompt}}$	182 ± 18	169 ± 18	169 ± 18	171 ± 18
$N_{\mathrm{J/psi-comb.+comb.-J/psi}}$	323 ± 28	323 ± 28	324 ± 28	326 ± 27
$N_{\mathrm{comb.-comb.}}$	94 ± 16	111 ± 16	111 ± 16	99 ± 16

selected for the central fit due to lack of statistics, particularly in the tail of the $M_{\mu\mu}$ distributions.

Table B.2: PDF parameters for M_{J/ψ_1} using a Crystal Ball function in signal prompt double J/ψ production.

Signal M_{J/ψ_1}	Value	Error
f^1	$2.88426 \cdot 10^{-1}$	$9.56806 \cdot 10^{-2}$
α^1	2.88399	$2.81005 \cdot 10^{-1}$
n^1	1.00040	$6.95318 \cdot 10^{-1}$
μ^1	3.09325	$1.21684 \cdot 10^{-3}$
σ_1^1	$4.85614 \cdot 10^{-2}$	$4.67134 \cdot 10^{-3}$
σ_2^1	$5.06440 \cdot 10^{-1}$	$2.92371 \cdot 10^{-2}$

Tables B.5, B.4, and B.6 display the values in an alternate fit using the product of a Gaussian and an exponential to characterize the shape of $d^{J/\psi}$ in the cases with a sideband extracted from data for the J/ψ-combinatorial, combinatorial-J/ψ, and combinatorial-combinatorial components. The shape is displayed in Fig. B.2.

Table B.3: PDF parameters for M_{J/ψ_2} using a Crystal Ball function in signal prompt double J/ψ production.

Signal M_{J/ψ_2}	Value	Error
f^2	$7.29412 \cdot 10^{-1}$	$1.13009 \cdot 10^{-1}$
α^2	2.09886	$9.03353 \cdot 10^{-1}$
n^2	2.02744	2.51040
μ^2	3.08964	$1.60017 \cdot 10^{-3}$
σ_1^2	$4.42237 \cdot 10^{-2}$	$1.71174 \cdot 10^{-3}$
σ_2^2	$4.90595 \cdot 10^{-1}$	$9.17511 \cdot 10^{-2}$

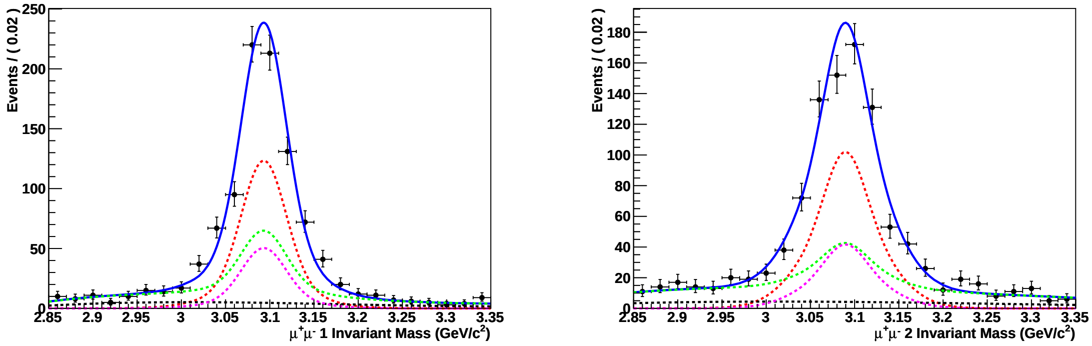

Figure B.1: Fits to determine PDF parameters for M_{J/ψ_1} (left) and M_{J/ψ_2} (right) using a Crystal Ball function.

Table B.4: PDF parameters for $d^{J/\psi}$ from sidebands extracted from data for the J/ψ-combinatorial component. The explanation of the method is given in Section 5.6.2.

J/ψ-Comb. $d^{J/\psi}$	Value	Error
μ_1	$2.28997 \cdot 10^{-1}$	$4.69367 \cdot 10^{-2}$
σ_1	$7.22911 \cdot 10^{-2}$	$4.09109 \cdot 10^{-2}$
λ_1	4.94307	$7.94631 \cdot 10^{-1}$

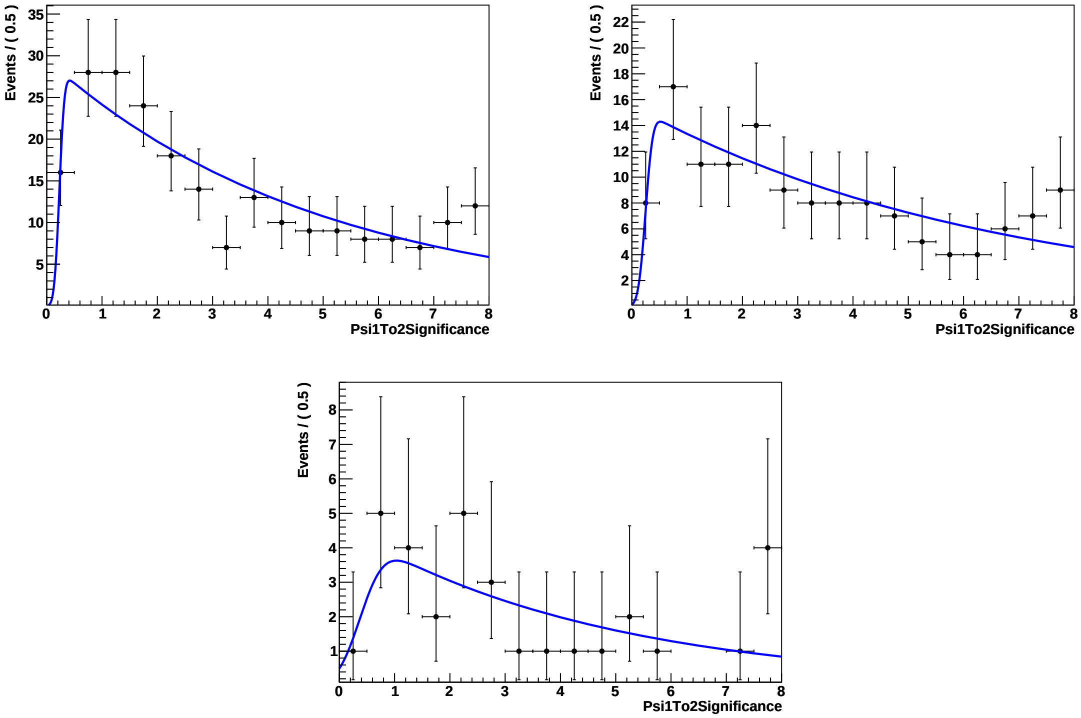

Figure B.2: Fits to determine PDF parameters for the significance of the distance between the two J/ψ from the sidebands extracted from data for the J/ψ-combinatorial (first), combinatorial-J/ψ (second), and combinatorial-combinatorial (third) components. The explanation of the method is given in Section 5.6.2.

Table B.5: PDF parameters for $d^{J/\psi}$ from sidebands extracted from data for the combinatorial-J/ψ component. The explanation of the method is given in Section 5.6.2.

Comb.-J/ψ $d^{J/\psi}$	Value	Error
μ_1	$2.49205 \cdot 10^{-1}$	$8.29338 \cdot 10^{-2}$
σ_1	$1.04013 \cdot 10^{-1}$	$7.63884 \cdot 10^{-2}$
λ_1	6.54912	1.68128

Table B.6: PDF parameters for $d^{J/\psi}$ from sidebands extracted from data for the combinatorial-combinatorial component. The explanation of the method is given in Section 5.6.2.

Comb.-Comb. $d^{J/\psi}$	Value	Error
μ_1	$3.89967 \cdot 10^{-1}$	$2.61645 \cdot 10^{-1}$
σ_1	$3.31232 \cdot 10^{-1}$	$2.46500 \cdot 10^{-1}$
λ_1	4.67109	1.98491

Vita

Andrew York was born on February 22^{nd} 1982. After completing high school at JEB Stuart High School in Falls Church, VA (USA) in 2000, he attended The College of William Mary from 2000-2004. He graduated with a B.S. degree in Physics and a Minor in Math. In 2006, while working as an Operations Research Analyst for the consulting company Systems, Planning, and Analysis, Inc. he was accepted to the PhD program of the University of Tennessee's Department of Physics. He taught for one year before starting a research assistant position. He received his Ph.D. in October 2013.